

The Pennsylvania State University

The Graduate School

Department of Chemistry

**CROSSING SCALES WITH COMPUTATIONAL TOOLS:
APPLICATIONS TO DIVALENT SILICATE DISSOLUTION**

A Dissertation in

Chemistry

by

Christin Palombo Morrow

© 2010 Christin Palombo Morrow

Submitted in Partial Fulfillment
of the Requirements
for the Degree of

Doctor of Philosophy

August 2010

The dissertation of Christin Palombo Morrow was reviewed and approved* by the following:

Karl T. Mueller
Professor of Chemistry
Dissertation Co-Advisor
Chair of Committee

James D. Kubicki
Dissertation Co-Advisor
Professor of Geochemistry

Sharon Hammes-Schiffer
Eberly Professor of Biotechnology and Professor of Chemistry

William G. Noid
Assistant Professor of Chemistry

Vincent H. Crespi
Professor of Physics and Professor of Materials Science and Engineering

Barbara J. Garrison
Shapiro Professor of Chemistry
Head of the Department of Chemistry

*Signatures are on file in the Graduate School

ABSTRACT

Computational tools are used to cross spatial scales during investigations of geochemical reactions and mineral surfaces. Density functional theory (DFT) calculations are employed to investigate M–O ($M = \text{Mg}^{2+}$, Ca^{2+} , and Ni^{2+}) bond breaking and H_2O exchange using a H_2O molecule and molecular sized clusters analogous to sites on silicate mineral surfaces. The barrier heights for hydrolysis of protonated, neutral, and deprotonated Mg–O–Si sites on the forsterite surface were determined. These barrier heights were used to calculate the rate constants, and in turn, a rate for the release of Mg^{2+} due to the breaking of the Mg–O bond. In a second set of calculations, hydrolysis of protonated M–O–Si ($M = \text{Mg}^{2+}$, Ca^{2+} , and Ni^{2+}) sites was investigated to determine whether H_2O exchange or bond breaking occurred for Ni^{2+} –, Mg^{2+} –, and Ca^{2+} –silicate molecular clusters. Here again, the barrier heights are used to calculate rate constants for release of these metals from protonated sites on silicate surfaces. A comparison with experimental data is given, and experimental trends are replicated.

Density functional theory molecular dynamics (DFT-MD) simulations enable the use of a unit cell sized system and allow for an investigation of several reaction sites on the mineral surface. The forsterite (100) and (010) surfaces were investigated to determine the most stable structures for these surfaces when initially covered with all H_2O molecules or OH groups. The surfaces yielded similar structures comprised of H_2O , OH, O^- , and O_{br} sites, and a true forsterite surface likely has a distribution of all of these sites. These surfaces were simulated in the presence of bulk water to investigate the surface structure at the aqueous-mineral interface over time, and H^+ and H_2O transfers between groups throughout the surface and between the solution and the surface were observed.

TABLE OF CONTENTS

LIST OF FIGURES	vi
LIST OF TABLES	x
ACKNOWLEDGEMENTS	xii
Chapter 1 Introduction	1
1.1 Increasing Levels and Storage of Atmospheric CO ₂	1
1.2 Silicate Mineral Structures	3
1.3 Kinetics	7
1.3.1 Transition State Theory (TST)	7
1.3.2 Rate Laws	9
1.4 Geochemical Reactions	13
1.4.1 Dissolution Reactions	14
1.4.2 Methods for Studying Dissolution	15
1.4.2.1 Experimental Methods	17
1.4.2.2 Computational Methods	19
1.5 Expected Implications	24
1.6 References	25
Chapter 2 A Description of Mg ²⁺ Release from Forsterite using Ab-Initio Methods	29
2.1 Introduction	29
2.2 Computational Methods	33
2.3 Results and Discussion	41
2.3.1 Hydrolysis of Mg–O–Si Sites	41
2.3.1.1 Reaction Coordinate	41
2.3.1.2 Energy Profiles	43
2.3.1.3 Reaction Mechanisms	48
2.3.1.4 Gibbs Free Energy Change	53
2.3.1.5 Overall Trends and Comparison to Experiment	55
2.3.2 Mg ²⁺ Release Rates from Mg–O–Si Sites versus pH	60
2.3.2.1 Parameters for Calculating the Rate	60
2.3.2.2 Rates versus pH	64
2.3.2.3 Comparisons with Previous Work	64
2.4 Conclusions	66
2.5 References	68
Chapter 3 Quantum Mechanical Modeling of Hydrolysis and H ₂ O-Exchange in Mg-, Ca-, and Ni-Silicate Clusters: Implications for Dissolution Mechanisms of Olivine Minerals	71

3.1 Introduction.....	71
3.2 Computational Methods.....	76
3.3 Results and Discussion	81
3.3.1 H ₂ O Exchange around the Hydrated Mg ²⁺ Ion.....	81
3.3.2 Reaction Mechanisms and Energy Profiles for H ₂ O Exchange and Hydrolysis	88
3.3.2.1 Protonated Ni–O–Si Sites.....	88
3.3.2.2 Protonated Mg–O–Si Sites	92
3.3.2.2.1 H ₂ O Exchange.....	92
3.3.2.2.2 Hydrolysis of a Protonated Mg–O–Si Site.....	94
3.3.2.3 Protonated Ca–O–Si Sites	97
3.3.2.3.1 Formation of Hepta-Coordinated Ca ²⁺	97
3.3.2.3.2 Hydrolysis of a Protonated Ca–O–Si Site.....	99
3.3.3 Molecular Orbital (MO) and Natural Bond Order (NBO) Analysis of H ₂ O Exchange and Hydrolysis Reactions.....	103
3.3.4 Rate Constants.....	106
3.3.5 Overall Trends and Comparison to Experiment.....	107
3.4 Conclusions.....	113
3.5 References.....	115
Chapter 4 Density Functional Theory Modeling of Water on Forsterite (100) and (010) Surfaces	118
4.1 Introduction.....	118
4.2 Computational Details	121
4.3 Results and Discussion	125
4.3.1 Bulk Forsterite Structure	125
4.3.2 Forsterite (100) and (010) Slabs.....	127
4.3.3 Associative and Dissociative Adsorption of H ₂ O to Forsterite Slabs ..	129
4.3.4 Density Functional Theory Molecular Dynamics (DFT-MD) Simulations.....	134
4.3.5 Comparison to Computational Results and Experimental Data	137
4.4 Conclusions and Future Directions.....	140
4.4.1 Conclusions	140
4.4.2 Future Directions.....	142
4.5 References.....	146
Chapter 5 Conclusions and Future Directions	148
5.1 Summary of Research.....	148
5.2 Expected Implications	152
5.3 Future Directions	155
5.4 References.....	158

LIST OF FIGURES

Figure 1-1: Formula units for silicate mineral structures. (a) Orthosilicate (b) Single chain (c) Double chain (d) Ring (e) Sheet (f) Framework. ¹⁵	4
Figure 1-2: Forsterite (100) mineral structure from the Materials Studio mineral structures database. ¹⁸ The Mg^{2+} ions are yellow, the Si tetrahedra are green, and the O atoms are red.	6
Figure 1-3: Anorthite mineral structure. ¹⁸ The O atoms are red, the Si tetrahedra are green, the Al^{3+} tetrahedra are blue, and the Ca^{2+} ions are cyan.	6
Figure 1-4: Plot of energy versus reaction coordinate where reactants, TS, dividing surface, and products are shown. ²⁰	8
Figure 1-5: Zero-order reaction. ²²	11
Figure 1-6: First-order reaction. ²²	12
Figure 1-7: Second-order reaction. ²²	12
Figure 1-8: Anorthite dissolution versus pH. The various shapes represent the input concentrations of Si, Ca^{2+} , and Al^{3+} . ⁴⁶	16
Figure 1-9: System size of computational methods versus simulation time. The number of atoms and timescales given in the boxes are the maxima possible for each computational method.	20
Figure 2-1: Forsterite (100) surface where a Mg–O–Si surface site has been extracted to depict the molecular cluster model. The magnesium atoms are yellow, the oxygen atoms are red, the silicon atoms are turquoise, and the hydrogen atoms are white.	30
Figure 2-2: Rates of Mg^{2+} release from the forsterite surface plotted as the log of the rate ($\text{mol m}^{-2} \text{s}^{-1}$) versus the pH. ⁵⁻¹¹ The data in this figure were taken from the ChemXSeer chemical kinetics database. ¹²	31
Figure 2-3: The model molecular cluster used to represent Mg–O–Si sites on the forsterite surface. The color scheme is the same as Figure 2-1 .	35
Figure 2-4: The PES scan of H_2O exchange around a neutral Mg–O–Si site. (a) The gas phase RC, TS, and PC species from the scan. The H_2O molecule circled in blue represents the H_2O molecule from the second hydration sphere that will bond with the Mg^{2+} in the products, and the H_2O molecule in the green circle will be released from the first hydration sphere of Mg^{2+} . (b) The energy (kJ/mol) of each point on the scan is plotted against the Mg– H_2O	

distance of the incoming H ₂ O molecule, and thus the progression of the scan is from right to left.....	42
Figure 2-5: The energy plot for the protonated Mg–O–Si site reaction. The gas-phase potential energy scan (G-P PES Scan) is green, and the aqueous-phase potential energy scan (A-P PES Scan) is orange. The energy profiles comparing the RC, TS, and PC in the gas-phase (G-P), single-point aqueous-phase (Single-Point A-P), and energy-minimized aqueous-phase (A-P) are black, red, and blue, respectively.....	45
Figure 2-6: The energy plot for the neutral Mg–O–Si site reaction where the labeling and color scheme are the same as Figure 2-5	46
Figure 2-7: The energy plot for the deprotonated Mg–O–Si site reaction where the labeling and color scheme are the same as Figure 2-5	47
Figure 2-8: The reaction mechanism for the hydrolysis of a protonated Mg–O–Si site. The reactant complex (RC), the transition state (TS), and the product complex (PC) are shown, and the color scheme is the same as Figure 2-1	49
Figure 2-9: The reaction mechanism for the hydrolysis of neutral Mg–O–Si sites. The color scheme is the same as Figure 2-1 , and the labeling is the same as Figure 2-8	50
Figure 2-10: The reaction mechanism for the hydrolysis of deprotonated Mg–O–Si sites. The color scheme is the same as Figure 2-1 , and the labeling is the same as Figure 2-8	51
Figure 3-1: PES scan of H ₂ O exchange around a solvated Mg ²⁺ ion. (a) The energy profile for this reaction in the gas-phase and the aqueous-phase. (b) The optimized RC, TS, and PC in the gas-phase. The magnesium ion is yellow, the oxygen atoms are red, and the hydrogen atoms are white. The H ₂ O molecule from the first hydration sphere that moves to the second is circled in green, while the H ₂ O molecule from the second hydration sphere that moves to the first is circled in blue.....	83
Figure 3-2: Optimized TS structures for the gas-phase, IEFPCM, and super-molecule calculations. The gas-phase TS is the same as that in Figure 3-1 but has been rotated to show the hepta-coordinated geometry around the Mg ²⁺ ion. The color scheme is the same as Figure 3-1	85
Figure 3-3: (a) The potential energy surface (PES) scan (blue line with blue squares) and optimized energy profile (red line with red squares) for hydrolysis of a protonated Ni–O–Si site where energy (kJ/mol) is plotted versus reaction coordinate. (b) The reaction mechanism for this reaction where the reactant complex (RC), transition state (TS), and product complex	

(PC) are presented. The nickel ion is blue, the silicon atom is turquoise, the oxygen atoms are red, and the hydrogen atoms are white.	89
Figure 3-4: (a) The PES scan (black line with open diamonds) and optimized energy profile (green line with closed diamonds) for H ₂ O exchange around Mg in a protonated Mg–O–Si site where energy (kJ/mol) is plotted versus reaction coordinate. (b) The reaction mechanism for this reaction where the RC, TS, and PC are presented. The magnesium ion is yellow, the silicon atom is turquoise, the oxygen atoms are red, and the hydrogen atoms are white.	93
Figure 3-5: (a) The PES scan (blue line with blue diamonds) and optimized energy profile (red line with red diamonds) for hydrolysis of a protonated Mg–O–Si site where energy (kJ/mol) is plotted versus reaction coordinate. (b) The reaction mechanism for this reaction where the RC, TS, and PC are presented. The color scheme is the same as for Figure 3-4	95
Figure 3-6: The (a) PES scan (black line with open triangles) and optimized energy profile (green line with closed triangles) for H ₂ O exchange around Ca ²⁺ in a protonated Ca–O–Si site where energy (kJ/mol) is plotted versus reaction coordinate. (b) The reaction mechanism for this reaction where the RC, TS, and PC are presented. The calcium ion is gold, the silicon atom is turquoise, the oxygen atoms are red, and the hydrogen atoms are white.	98
Figure 3-7: (a) The PES scan for the forward direction (blue line with closed triangles), the PES scan for the reverse direction (open blue triangles), and optimized energy profile (red line with closed triangles) for hydrolysis of a protonated Ca–O–Si site where energy (kJ/mol) is plotted versus reaction coordinate. (b) The reaction mechanism for this reaction where the RC, TS, and PC are presented. The color scheme is the same as for Figure 3-6	100
Figure 3-8: The molecular orbitals (MOs) for the hydrolysis of protonated Ni–O–Si, Mg–O–Si, and Ca–O–Si sites. The columns correspond to RCs or TSs, and the rows correspond to each silicate site.	104
Figure 3-9: The molecular orbitals (MOs) for the H ₂ O exchange reaction for protonated Mg–O–Si sites as well as for the formation of the hepta-coordinated Ca–O–Si complex. The columns correspond to RCs or TSs, and the rows correspond to each silicate site.	105
Figure 3-10: The log of the rate constant k (s ⁻¹) for hydrolysis and H ₂ O exchange at protonated Ni–O–Si, Mg–O–Si, and Ca–O–Si sites (from this work) versus the log of the rate constant k (s ⁻¹) of H ₂ O exchange for each of the corresponding metal ions. ^{17,57}	108
Figure 4-1: Scheme of computational methods used in this work.	123

Figure 4-2: (a) Initial structure of bulk forsterite from Cerius ² mineral database. ^{26,27} (b) Energy-minimized bulk forsterite structure. ²⁷	127
Figure 4-3: Forsterite (100) slab. (a) Initial structure. ^{26,27} (b) Energy-minimized structure. ²⁷	128
Figure 4-4: Forsterite (010) slab. (a) Initial structure. ^{26,27} (b) Energy-minimized structure. ²⁷	128
Figure 4-5: Hydrated forsterite (100) surface. a) Original (left) and energy-minimized (right) surface structures for associative adsorption of H ₂ O molecules. b) Original (left) and energy-minimized (right) surface structures for dissociative adsorption of H ₂ O molecules. The color scheme is such that magnesium ions are yellow, silicon atoms are green, oxygen atoms are red, and hydrogen atoms are white.	131
Figure 4-6: Hydrated forsterite (010) surface. a) Original (left) and energy-minimized (right) surface structures for associative adsorption of H ₂ O molecules. b) Original (left) and energy-minimized (right) surface structures for dissociative adsorption of H ₂ O molecules. The color scheme is the same as Figure 4-5	133
Figure 4-7: (a) Forsterite (100) surface solvated with low-density water. Atoms are characterized according to their x-coordinates. (b) O atom histogram and (c) H atom histogram. Each histogram is averaged over the last 5 ps of simulation. The color scheme is the same as Figure 4-5	136

LIST OF TABLES

Table 2-1: Barrier heights (kJ/mol) for hydrolysis of protonated, neutral, and deprotonated sites for calculations in the gas-phase, single-point aqueous-phase, and energy-minimized aqueous-phase calculations.	48
Table 2-2: Mg–O and Si–O distances (Å) and Mg–O–Si angles (°) for RCs and TSs for all reactions in the gas-phase.	54
Table 2-3: The change in Gibbs free energy (ΔG) values (kJ/mol) for Mg^{2+} release from protonated, neutral, and deprotonated sites in the gas- and aqueous-phase hydrolysis reactions.....	55
Table 2-4: Ab-initio barrier heights (kJ/mol) for Si–O–Si site hydrolysis in the gas phase. ^{2,24,25,54}	57
Table 2-5: Pre-exponential factors A (s^{-1}) and rate constants k (s^{-1}) for the hydrolysis of Mg–O–Si sites on the forsterite surface.....	61
Table 2-6: Reaction rates ($\text{mol m}^{-2}\text{s}^{-1}$) for the hydrolysis of protonated, neutral, and deprotonated sites in gas-, single-point aqueous-, and energy-minimized aqueous-phases.	62
Table 3-1: Relevant distances (Å), bond angles (°), barrier heights (kJ/mol), pre-exponential factors (s^{-1}), and rate constants (s^{-1}) for the H_2O exchange reaction around $\text{Mg}(\text{H}_2\text{O})_6^{2+}$	84
Table 3-2: Reaction enthalpies (ΔH^\ddagger , in kJ/mol) and barrier heights (ΔE^\ddagger , in kJ/mol) for H_2O exchange around $\text{Ni}(\text{H}_2\text{O})_6^{2+}$, $\text{Mg}(\text{H}_2\text{O})_6^{2+}$, and $\text{Ca}(\text{H}_2\text{O})_6^{2+}$ in the gas-phase from previous studies ^{42,43,45,54-56} and from this work for $\text{Mg}(\text{H}_2\text{O})_6^{2+}$ in the gas-phase and aqueous-phase.....	87
Table 3-3: Relevant distances (Å) and bond angles (°) in the reactions for protonated Ni–O–Si, Mg–O–Si, and Ca–O–Si sites.....	90
Table 3-4: Barrier heights (kJ/mol) for H_2O exchange and hydrolysis of protonated Ni–O–Si, Mg–O–Si, and Ca–O–Si sites.....	91
Table 3-5: Energies (kJ/mol) and change in energy (ΔE , kJ/mol) for relevant molecular orbitals (MOs) in the hydrolysis reactions of protonated Ni–O–Si, Mg–O–Si, and Ca–O–Si sites, the H_2O exchange reaction at the protonated Mg–O–Si site, and the formation of the hepta-coordinated Ca–O–Si site.	106
Table 3-6: The pre-exponential factors A (s^{-1}) and rate constants k (s^{-1}) for H_2O exchange and hydrolysis of protonated Ni–O–Si, Mg–O–Si, and Ca–O–Si sites.	107

Table 4-1: Energies (J) and lattice parameters (\AA^3) for forsterite samples studied throughout this work. *For the forsterite (010) aqueous-mineral interface, $t = 6.0$ ps.	126
Table 4-2: Type and number of functional groups on the bulk, slab, hydrated, and aqueous-mineral interface surfaces for forsterite (100) and (010). The raw number and the fraction of total sites are given.....	130
Table 4-3: Relative energies (J/m^2) for the forsterite (100) and (010) slabs, hydrated surfaces, and aqueous-mineral interfaces.	130

ACKNOWLEDGEMENTS

My sincerest gratitude goes to my advisors, Jim Kubicki and Karl Mueller, who graciously and excitedly accepted me as a graduate student into their groups both suddenly and late in my career. From the very first day that I worked with them until my last, they treated me as a colleague and granted me room to research and develop on my own. I aspire to achieve their enthusiasm, intelligence, and creativity in their profession, and I hope to emulate and to pass on their positive examples.

I am also indebted to my financial supporters. Throughout my doctoral career, I was sponsored by several National Science Foundation and Department of Energy grants. I received funding from the Center for Environmental Kinetics Analysis (CEKA), an NSF-DOE environmental molecular sciences institute, through grant number CHE-0431328 as well as through the ChemXSeer project, a environmental kinetics database, through grant number CHE-0535656. In addition, my research was funded by the Department of Energy Biological and Environmental Research (BER) through the student contract “Rates and Mechanisms of Mineral-Fluid Interactions at the Nanoscale” with Oak Ridge National Laboratory.

Two colleagues that I have enjoyed collaborating with and have learned a great deal from are Dave Cole, Oak Ridge National Laboratory, and Amanda Olsen, University of Maine. Dave Cole has taught me how experimental geochemists think and how I can tailor my theoretical research to most effectively communicate my science as well as design research projects to most usefully fill in the gaps that experimentalists have not been able to do themselves. I am also very appreciative of Dave’s commitment to CEKA and his financial support of my research. I had the fortune of working with Amanda

during her time here at Penn State as a post-doc, and I enjoyed writing the manuscript which serves as Chapter 3 in this work with her. I admire her as a scientist, and she has been a great role model to me.

I have also had the incredible fortune to work with three wonderful research groups. The Mueller Group past and present – Bill Brouwer, Tom Morgan, Mike Davis, Caleb Strepka, Dave Roach, Becky Sanders, Lymaris Ortiz-Rivera, Dan Suchy, Eric Fillerup, Carrie Ryan-Silverstein, Eric Poweleit, Kelly Murphy, and countless undergraduate students – have helped me immensely. I must particularly point out Mike, Becky, and Caleb for answering my seemingly unending questions regarding minerals, their structure, and experiments regarding their dissolution. Tom, Becky, and Kelly gave insightful suggestions to drafts of this dissertation. Eric and I regularly traded textbooks while I was writing this dissertation and he was preparing for his Oral Exam. Carrie was particularly helpful in her constructive criticisms of early drafts of interview and defense presentations, and from her, I learned so much about how to communicate my research effectively and innovatively. The members of this group are so very special, and I have enjoyed sharing offices, drinks, chicken wings, and various joyful get-togethers with them. I will miss you each very greatly.

The second research group in which I participated was the Center for Environmental Kinetics Analysis (CEKA), and it was through CEKA that I first realized I should become a geochemist. As a child growing up down the South Jersey Shore, I was never exposed to mountains or rocks and did not think much about them. Once I began interacting with the faculty, post-doctoral scholars, students, and affiliates associated with CEKA, I learned so much about the Earth as well as developed immensely as a scientist.

They are perhaps the most welcoming, respectful, and collaborative assembly of scientists that I have ever met. Each meeting, workshop, or casual gathering of CEKA members has been informative, inviting, and invigorating. I enjoyed working for and with this group of people. I am not entirely sure what lies ahead in my professional future, but whichever path I choose, I sincerely hope that I find another group very much like CEKA.

The Kubicki group was very helpful to me late in my stay as a group member. I have to thank Andrei Bandura and Masoud Aryanpour especially for their help with the visualizations and data analysis for the VASP calculations in Chapter 4 of this dissertation. I also must thank our collaborators Nitin Kumar, from Jorge Sofo's group, and Mike Russo and Sung-Yup Kim from Andri van Duin's group who helped with the data analysis for the VASP calculations. Qing Zhu assisted me with Materials Studio when Cerius² died two months before this work was due, and Qing inspired me to step out of my comfort zone and apply to a job slightly outside of my field. I have greatly enjoyed interacting with Heath Anderson, Brendan Puls, Naseer Mohamed, Lara Kabalan, and Zhen Zhao, and I will miss chatting and celebrating with them.

I must equally thank my husband, Tom Morrow, without whom I would never have begun my Ph. D. career (again). A wise person once told me that the best professional move a person can make is to marry or commit well. This has been my experience in that Tom has stood by me as a colleague, friend, and husband, and thus my professional success in the attainment of this degree is very much his as it is my own. I look forward to our continued success in both our careers and our marriage. I know that we will both garner significant accomplishments throughout our lifetimes.

My family has been a completely selfless group of people on whom I could count for helpful advice and sincere support throughout my entire graduate experience. My parents have gracefully developed a balance between authority figures, esteemed confidantes, and friends. My sisters, Kimberly and Regina, have helped me to see how easy it can be to add fun into one's hectic and professionally serious life. Two of my aunts – Dr. Kathleen Ward Brown and Sandra Palombo, M. S. – inspired me as scientists, successful women, and role models. These and many others are the Tree in Shel Silverstein's *The Giving Tree*; no matter which the circumstance, somehow they had the resources to be just the comfort I needed. I will forever be indebted to them, and I only hope that my thankfulness for having them in my life is apparent each day.

Chapter 1

Introduction

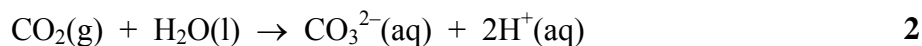
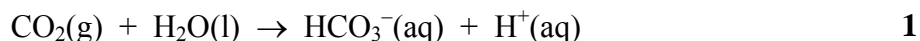
1.1 Increasing Levels and Storage of Atmospheric CO₂

The rising levels of CO₂ in the atmosphere^{1,2} have increased our need for a better understanding of the global carbon cycle. The global C cycle describes the transformation of C substances throughout the Earth between the atmosphere, bodies of water, Earth's surface, and biota.³ The interplay between anthropogenic CO₂ and C mitigation by minerals has recently received much attention⁴⁻¹⁰ due to the potential to store C long-term. These studies provide insight into how geological systems play a role in the C cycle.

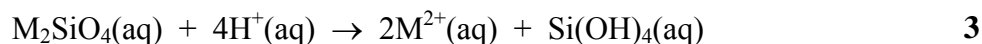
The ability of a particular mineral to mitigate C depends, in part, on the release of metal ions from its structure. In addition to dissolution of minerals for CO₂ storage, this process occurs on Earth's surface and affects groundwater chemistry, erosion, and the concentrations of soil nutrients.¹¹ Dissolution of minerals controls numerous life processes on Earth, and particular focus has been given to investigations of silicate minerals because they are the most abundant class of minerals on Earth's surface.¹²

Silicate minerals are desirable choices for geologic storage because of their relatively rapid dissolution rates.¹³ In particular, the dissolution of divalent cation silicate minerals – such as those that contain Mg²⁺ and Ca²⁺ – is especially important because the leached cations can be used to “trap” anthropogenic CO₂ during a process known as

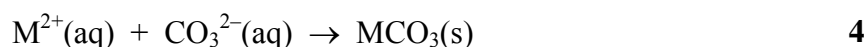
“mineral trapping.”^{4,7-10} For example, in underground mineral trapping, also known as *in situ* storage, CO₂ is injected into a saline aquifer¹⁴ and reacts with water through reactions **1** and **2**:



where the formerly gaseous CO₂ is now present as aqueous carbonate ions. The H⁺ formed during this transformation then reacts with the mineral surrounding the aquifer cavity. **Reaction 1-3** describes the case of a divalent cation silicate:



As the mineral dissolves, metal ions (M²⁺) are released to solution and are available for reaction with the carbonate ions (CO₃²⁻), produced by the dissolution of CO₂ as described in **Reactions 1-1–2**. This interaction is described by the **Reaction 1-4**, showing the general precipitation scheme of carbonate mineral forms:



Thus, the gaseous CO₂ is “trapped” as a stable solid carbonate. Similar reactions can occur in *ex situ* mineral trapping reactions where Mg-silicates are dissolved and the Mg²⁺ is used to precipitate Mg-carbonates.¹⁴ Despite the urgency for a means to store CO₂, a molecular scale understanding of how these minerals release metal ions to solution does not exist; therefore, investigations into the breaking of M–O bonds as well as the distribution of protonation states of surface sites are required to provide insight into how metal ions are released from mineral surfaces.

1.2 Silicate Mineral Structures

In order to understand how metal ions are released from the mineral surface, one must begin by describing silicate mineral structures. The structure of each silicate mineral is based upon the SiO_4^{4-} tetrahedron, where a Si atom is bonded to four O atoms (**Figure 1-1a**).^{12,15} Orthosilicate minerals are those where each SiO_4^{4-} does not share any O atoms with the closest SiO_4^{4-} within the mineral structure.¹² The remaining mineral classes, however, share at least one apex of the tetrahedron with a neighboring SiO_4^{4-} unit. Disilicate minerals share one mutual O atom between two SiO_4^{4-} units. Single chain silicates, whose structure is shown in **Figure 1-1b**, share two mutual O atoms in each SiO_4^{4-} tetrahedron. Double chain silicate minerals in **Figure 1-1c** share three O atoms per SiO_4^{4-} tetrahedron, and this is akin to the single chain silicate structure in **Figure 1-1b** being joined together with its mirror. Ring silicate minerals have six SiO_4^{4-} formula units linked together such that each tetrahedron shares two O atoms (**Figure 1-1d**). The structure for sheet silicate minerals is shown in **Figure 1-1e**, and here the ring silicate structure of **Figure 1-1d** is essentially extended laterally. Lastly, the framework silicate mineral structure is shown in **Figure 1-1f**, and in this case, every O atom within the SiO_4^{4-} formula unit is shared between tetrahedra.¹²

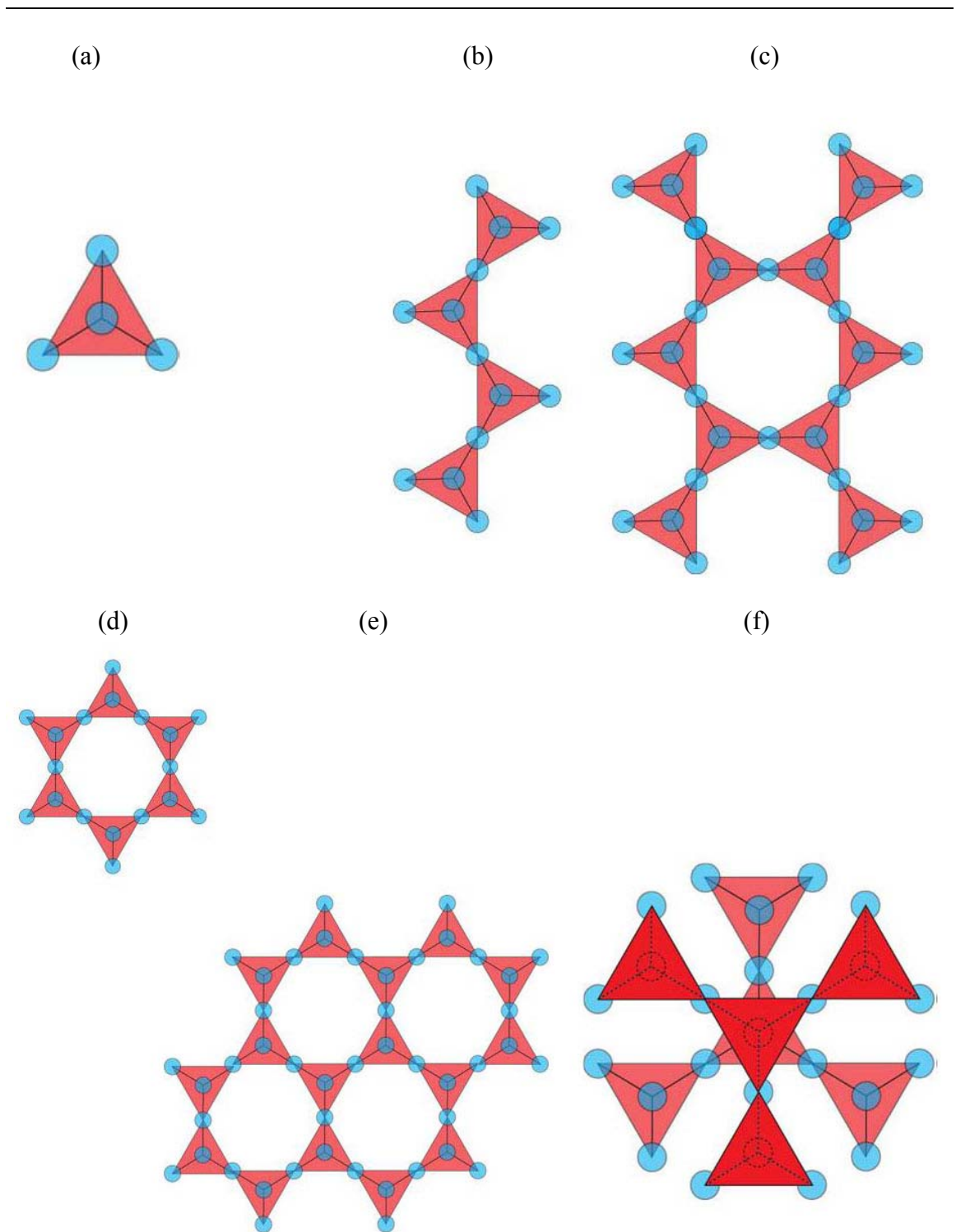


Figure 1-1: Formula units for silicate mineral structures. (a) Orthosilicate (b) Single chain (c) Double chain (d) Ring (e) Sheet (f) Framework.¹⁵

In this work, the two main classes of silicate minerals discussed are orthosilicates (**Figure 1-1a**) and framework silicates (**Figure 1-1f**). The orthosilicate mineral that receives the most attention is the forsterite end-member of the olivine series. Forsterite, Mg_2SiO_4 , has SiO_4^{4-} tetrahedra that are connected via Mg^{2+} ions. Each Mg^{2+} is present in octahedral coordination such that the six O atoms from neighboring SiO_4^{4-} tetrahedra satisfy this coordination. Two Mg^{2+} ions for every SiO_4^{4-} tetrahedron serve to balance the charge.¹⁶ These MgO_6 octahedra alternate the SiO_4^{4-} tetrahedra in the mineral structure (**Figure 1-2**).¹⁷

In addition to forsterite, anorthite ($\text{CaAl}_2\text{Si}_2\text{O}_8$) is discussed throughout this work. The anorthite end-member of the plagioclase group of framework silicates is a Ca-aluminosilicate. In this mineral, both Si and Al are tetra-coordinated to four O atoms, forming SiO_4 and AlO_4 tetrahedra (**Figure 1-3**).¹⁸ Four tetrahedra are bound where each shares two O atoms with its neighbor, forming a ring. Rings are bound together by sharing additional O atoms and are arranged in spirals. The “framework” arises from the lateral joining of these rings. The resulting structure is open and therefore can accommodate larger cations such as Ca^{2+} .¹² Structural analysis of the Ca^{2+} within the mineral shows that it is likely hepta-coordinated.¹⁹

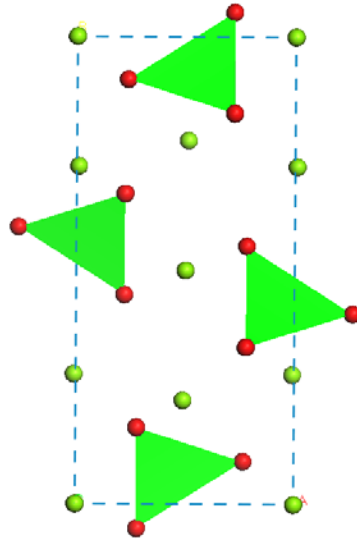


Figure 1-2: Forsterite mineral structure from the Materials Studio mineral structures database.¹⁸ The Mg²⁺ ions are yellow, the Si tetrahedra are green, and the O atoms are red.

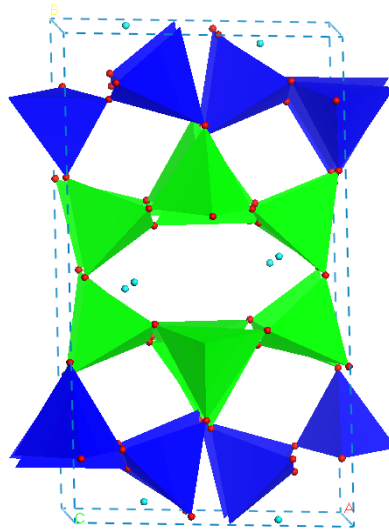


Figure 1-3: Anorthite mineral structure.¹⁸ The O atoms are red, the Si tetrahedra are green, the Al³⁺ tetrahedra are blue, and the Ca²⁺ ions are cyan.

1.3 Kinetics

1.3.1 Transition State Theory (TST)

The transition state theory (TST) approximation is used to describe the rate of dissolution for the divalent cation silicates discussed herein. TST describes reaction mechanisms and reaction rates and hinges upon the existence of a short-lived chemical species that has characteristics of both the reactants and the products of the reaction. TST is derived from the statistical nature of the reacting species but, in its most classical state, does not include quantum contributions. The change from reactants to products is traced along the reaction coordinate, and the transition state corresponds to the structure with the highest free energy along that path. The transition state (TS) is more specifically a saddle point where the maximum energy along the reaction coordinate serves as the minimum energy point along the path orthogonal to the reaction coordinate (**Figure 1-4**).²⁰

There are several assumptions made by the TST that become critical when calculating the rate of a reaction. First, the TST incorporates the Born-Oppenheimer approximation, where electronic motion is decoupled from the nuclear motion. Second, a Maxwell-Boltzmann distribution exists among reactant molecules. Third, those reactants that contain sufficient energy to cross the TS barrier toward the products are not able to recross this barrier and return to reactants (*i. e.* the reaction is irreversible). Fourth, movement along the reaction coordinate is independent from other molecular motions. Lastly, those TSs moving toward products exist in states according to Maxwell-Boltzmann distributions.²⁰

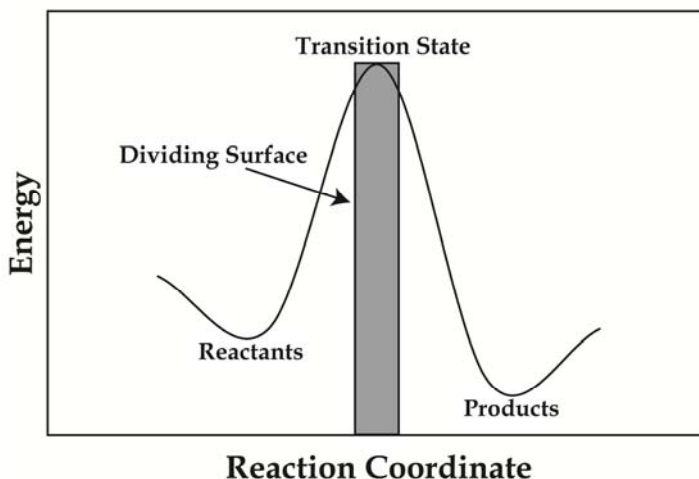


Figure 1-4: Plot of energy versus reaction coordinate where reactants, TS, dividing surface, and products are shown.²⁰

The equilibrium that is assumed to exist between the reactants and the TS is known as the quasi-equilibrium hypothesis. In this description, a model reaction is considered according to **Reaction 1-5**:



where A and B are the reactants, X^{\ddagger} is the transition state, and C is the product. The energy profile of this model reaction is shown in **Figure 1-4**. Species moving toward the products proceed from left to right in the plot in **Figure 1-4**, and those moving from products to reactants move from right to left. The TS exists at the center of the plot where the potential energy is the greatest. This region is known as the dividing surface and is used to delineate those species that have “crossed over” from reactants to products or vice versa. Thus TSs may either be those species forming as products become reactants or as reactants become products. The rate of the reaction describes the speed at which TSs are converted to products (forward) or reactants (reverse).²⁰

1.3.2 Rate Laws

From the classical TST, the rate for a reaction can be calculated using the energy difference between the reactants and TS. The difference in internal energy between the reactants and the TS $\Delta U_{\ddagger}^{\circ}$ can be related to the activation energy E_a according to **Equation 1-6**:

$$E_a = RT + \Delta U_{\ddagger}^{\circ} \quad 6$$

where R is the gas constant and T is the temperature in K.²¹ E_a is defined as the minimum energy required for a reaction to occur and can be used to calculate the rate constant k for a reaction through the Arrhenius equation (**Equation 1-7**):

$$k = Ae^{-E_a/RT} \quad 7$$

where A is the Arrhenius pre-exponential factor.²⁰ For the gas phase, A is defined by **Equation 1-8**:

$$A = e^{-(\Delta n_{\ddagger}-1)} \frac{k_B T}{h} e^{\Delta S_{\ddagger}^{\circ}/R} \quad 8$$

where Δn_{\ddagger} is the change in moles between the reactants and TS, k_B is Boltzmann's constant, h is Planck's constant, and $\Delta S_{\ddagger}^{\circ}$ is the standard entropy change between the reactants and TS.²⁰

Several factors affect the rate constant; however, E_a and T are of particular interest to this work. Due to the inverse exponential relationship between k and E_a , a greater E_a is associated with a smaller k . The temperature of a reaction, however, has the opposite effect on k such that both increase concurrently as described in **Equation 1-7**.

In addition, the temperature dependence of A contributes to the temperature dependence of k .²⁰

Reaction rates are not only affected by temperature but on the relative concentrations of reactants. For example, a zero-order reaction has no concentration dependence,²⁰ and the relationship between the rate of the reaction and the concentration of a reactant follows **Equations 1-9–10**:

$$r = k[A]_0 = k \quad 9$$

where r is the rate of the reaction, k is the rate constant, and $[A]_0$ is the initial concentration of the reactant.²² **Equation 1-9** can be integrated to yield the slope-intercept form of a line:

$$[A]_t = -kt + [A]_0 \quad 10$$

where $[A]_t$ is the concentration at time t . **Figure 1-5** shows a typical zero-order reaction, where the plot follows **Equation 1-10**, and the rate constant k is the slope of the line.

However, if the rate of the reaction increases linearly with the concentration of a reactant, then the reaction is of the first order and is described by **Equation 1-11**:

$$r = k[A] \quad 11$$

Equation 1-11 can be integrated and rearranged to give slope-intercept form, shown by **Equation 1-12**:

$$\ln[A]_t = -kt + \ln[A]_0 \quad 12$$

A plot of **Equation 1-12** is given in **Figure 1-6**.

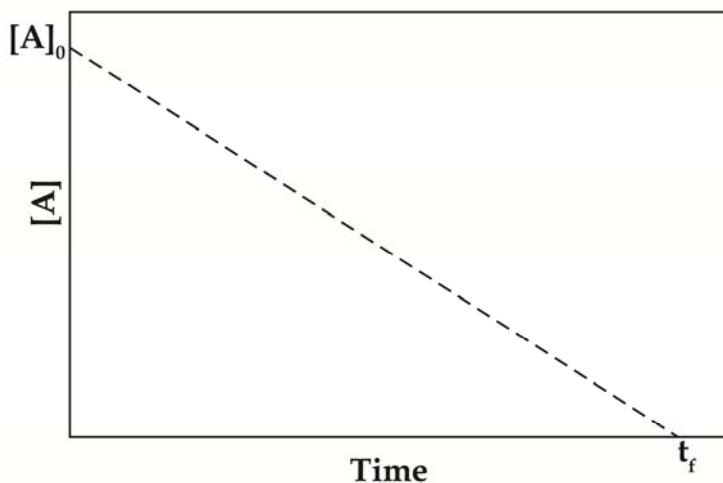


Figure 1-5: Zero-order reaction.²²

In some cases, the rate of a reaction increases with the square of the concentration of a reactant, and these reactions are known as second-order. The rate law for a second-order reaction is defined as **Equation 1-13**,

$$r = k[A]^2 \quad 13$$

and is integrated to form **Equation 1-14**:

$$\frac{1}{[A]_t} = kt + \frac{1}{[A]_0} \quad 14$$

Figure 1-7 displays a second-order reaction.²²

The orders of reactions can be classified according to the effect of each individual reactant on the overall rate of a reaction. If, for example, a rate doubles when $[A]$ doubles, then the reaction is first-order with respect to A . However, if the rate of the same reaction quadruples as $[B]$ doubles, then the reaction is second-order in B . The overall order of a

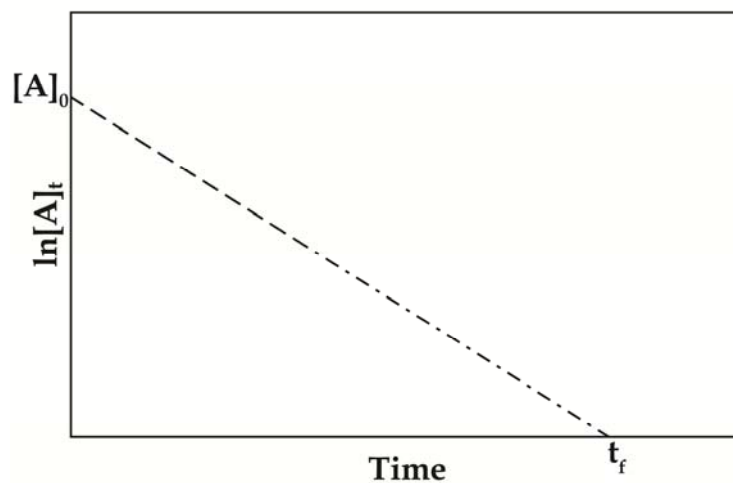


Figure 1-6: First-order reaction.²²

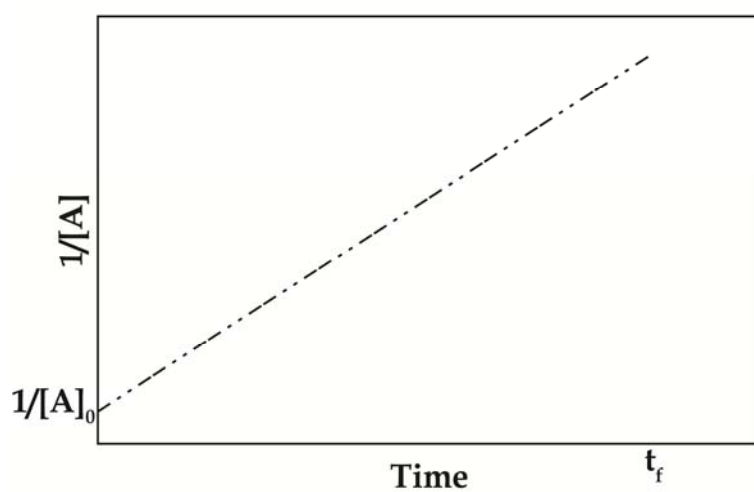


Figure 1-7: Second-order reaction.²²

reaction is the sum of the orders of the individual reactants, and in this example, the reaction is third-order overall.²⁰

For reactions involving more than one step²⁰ or where one reactant is present in great excess of another,²² the pseudo-first order approximation can be used. In

experimental situations where $[A] \gg [B]$,²⁰ the rate of the reaction appears to behave independently of $[A]$.²² For those reactions where bulk water serves as a reactant, the pseudo-first order approximation is invoked.²² Some geochemical reactions are examples of those that appear as pseudo-first order reactions and will be discussed in **Section 1.4**.

Computational determinations of experimental rate laws have recently been employed to describe geochemical systems.^{23,24} In these investigations, molecular clusters representing single surface sites were used, and the energy required to break the Si–O bond²³ and Mg–O bond²⁴ was calculated. This energy was used to calculate the rate constant as in **Equation 1-7**, and the rate laws for dissolution of quartz²³ and forsterite²⁴ were described according to the pseudo-first order approximation.

1.4 Geochemical Reactions

Geochemical reactions are studied for their contributions to natural¹¹ and energy-related processes,⁴⁻¹⁰ but understanding the kinetics of these reactions is challenging for a number of reasons. First, these reactions often occur in aqueous media, and therefore, water as well as dissolved species are reacting with the mineral under investigation, leading to complex competing or side reactions. Further, separating the contributions of water, H_3O^+ , OH^- , and additional ions such as Na^+ , Cl^- , or Ca^{2+} compounds this issue, as dissolved ions are known to catalyze some geochemical reactions.²⁵⁻²⁹ In addition, determining the concentrations of reactants may often be difficult.³⁰⁻³³ For example, quantifying the number of sites on a surface that participate in a given reaction remains poorly understood since many investigations have focused on the total number of surface

sites as opposed to only those sites that participate in the reaction.³²⁻³⁴ For dissolution, the release of species to solution is considered to be pseudo-first order because of the excess of water in the system, but the rate law for each mineral differs³⁴ and depends strongly upon pH.³⁵⁻³⁸ Each effect on dissolution must be investigated individually to determine its impact on the rate, and there are a number of experimental and theoretical approaches that can be used, which will be discussed below.

1.4.1 Dissolution Reactions

Dissolution of a mineral can be defined as the collection of physicochemical phenomena that cause the ultimate breakdown of the mineral structure and lead to the net release of elemental and ionic constituents to solution.³⁹ If one traces these phenomena chronologically, then a complete picture of dissolution can be described. First, species from solution are transported to the mineral surface, and these include H₂O molecules, H₃O⁺ ions, OH⁻ ions, and dissolved species such as organic acids, metal cations, and halide anions.³⁹ Next, these species adsorb to the mineral surface, a process thought to contribute to degradation of the mineral surface.⁴⁰ The adsorption of ions,^{39,41,42} such as H₃O⁺, to the surface O atoms weakens the M–O bond, allowing this bond to break more easily.³⁹⁻⁴¹ Additional chemical reactions lead to the alteration of the mineral surface structure, such as the development of surface defects. These features are sites where surface reactions can preferentially occur.^{43,44} As mineral constituents are released to solution, additional ions from solution replace them in the mineral structure to allow for charge-balancing.⁴⁵ The final step of dissolution is the transport of dissolved species

away from the aqueous-mineral interface into solution.³⁹ **Figure 1-8** shows the dissolution rate of anorthite as pH increases, and such an analysis is typical of experimental descriptions of dissolution. Both experimental and theoretical approaches to investigating dissolution focus on examining each of these processes in turn, and these techniques and models will be discussed in the following section.

1.4.2 Methods for Studying Dissolution

Dissolution of geochemical materials can either be studied experimentally or computationally. The rates of these reactions are determined by measuring the concentration of product species in solution over time, and thus, these experiments rely on the release of chemical species from the mineral surface to solution. Once the rate of a dissolution reaction has been determined, the rate constant for a reaction, and subsequently the activation energy, may be determined. Computational methods approach dissolution reactions oppositely such that the energy for a given reaction is calculated, and the rate constant is calculated using **Equation 1-7**. The goal of a computational approach investigating dissolution is the ability to either compare observed trends in experimental data or to calculate a quantity that is experimentally measured. In the two sections below, various types of experimental and computational approaches to studying dissolution reactions are described.

In the rate law for a geochemical reaction, the surface area of the mineral sample is experimentally measured and is assumed to be proportional to the reaction rate.³⁴⁻³⁸

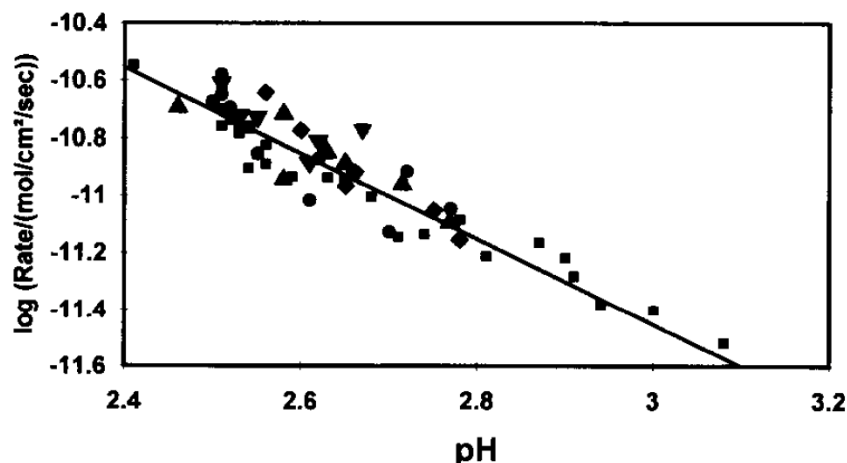


Figure 1-8: Anorthite dissolution versus pH. The various shapes represent the input concentrations of Si, Ca²⁺, and Al³⁺.⁴⁶

One of the most common methods for determining the surface area of a mineral sample is the Brunauer-Emmett-Teller (BET) surface area.⁴⁷ In this approach, an inert gas adsorbs to the mineral surface, and the surface area of the sample is determined according to the volume of gas that was lost to adsorption. The surface area that is calculated is then inserted into the rate law and used to explain the contribution of surface sites to the reaction rate. Unfortunately, the BET surface area does not always correlate to the dissolution rate of mineral samples,³² resulting in the necessity to quantify the reactive surface sites needed to describe the surface contribution to dissolution.^{32,48} That is to say, instead of considering the entire surface area as participating in dissolution, only individual sites that are known to be more reactive than others are considered to play a role in dissolution.^{32,48}

Computational descriptions of mineral surface samples can provide insight into the problem of total surface sites versus reactive surface sites. Modeling the surface topography shows where adsorption of gas particles to the surface is most likely and also

provides insight into the role of surface structure on the adsorption of gas particles.^{44,49} Because dissolution is comprised of a collection of processes,³⁹ computational approaches using molecular clusters focus on representing individual sites to explain the contribution of each to reactions of dissolution on the mineral surface,^{23,24,26,27,50-54} and these calculations further provide insight into which steps are rate-limiting.²⁴

1.4.2.1 Experimental Methods

Several experimental approaches have been used to study the dissolution of minerals. The two that have the most popularity are batch reactors^{5,10,33,35,45,55} and flow-through reactors.^{8,32,34,40,43,56} Batch reactors consist of a single container where all of the reactants are placed together and continuously stirred to promote homogeneous reaction conditions in solution. The reaction progress is measured by the accumulation of products in solution, and the concentration can be followed with time. The advantage of this method is that these reactors are easily constructed. Unfortunately, frequent sampling of the solution leads to a complicated description of the reaction rate, particularly if the rate changes with time.⁵⁷ Batch reactors have been used to study the dissolution of a variety of minerals, such as alumina,⁴¹ basalt,³⁶ beryllium oxide,⁴¹ forsterite,^{5,35,45,55} kaolinite,^{33,38} montmorillonite,³³ serpentine,¹⁰ and silica.²⁸

The other commonly used experimental method for dissolution is a flow-through reactor, also known as a mixed-flow reactor. In this setup, fluid moves through the reaction vessel at a continuous rate. The concentration of products in the outgoing solution is monitored and used to gauge the progress of the reaction. The advantage to

this method is that the reaction rate is determined directly as the concentration of products increases with time, but the disadvantage is that these apparatus require difficult construction.⁵⁷ Mixed-flow reactors have been used to study the dissolution of aluminosilicates,³² anorthite,³⁴ forsterite,^{8,40,56} and quartz.^{25,43}

Two other less commonly used experimental approaches for studying dissolution are surface titrations^{30,31} and the pH stat method.^{42,58,59} In a surface titration experiment, the mineral sample is suspended in solution, and either acid or base is added step-wise.³⁰ The pH is monitored throughout the experiment, and the loss of either H_3O^+ or OH^- ions from solution indicates adsorption to the mineral surface.^{30,31} The pH stat method is similar to a batch reactor where the reaction is contained in a single vessel, and the solution is sampled periodically.⁵⁹ A constant pH is maintained by the addition of acid to compensate for H^+ ions used in the dissolution reaction scheme.⁵⁹

The strength of experimental approaches, then, is the ability to follow dissolution processes simultaneously and measure the concentration of several products or the effect of several environmental factors within the same reaction scheme. Despite the existence of several experimental methods for studying the dissolution of minerals, developing an accurate molecular-scale picture of the processes occurring in solution at the mineral surface is still an elusive challenge in these studies. In order to understand geochemical processes from a molecular perspective, computational methods have become another tool used to probe the nature of these systems.

1.4.2.2 Computational Methods

The strength of computational methods is the ability to describe a molecular-scale picture of an individual process within a geochemical reaction scheme. Several temporal and spatial scales are possible using computational tools, and these regimes are depicted in **Figure 1-9**. The challenge, however, is to include enough chemical information so the calculations provide molecular information while simultaneously representing a system size or timescale that provides meaningful insight. Further, this challenge is compounded by the size of the system that can be studied. Smaller systems are required to include chemical information such as electronic structure, and these calculations are tractable up to ~50 atoms. Larger systems of $10^2 - 10^5$ atoms can also be modeled, but the tradeoff is that the electronic structure is not included, which permits these calculations to remain feasible.

The smallest-sized systems can be studied with electronic structure calculations, and one particular class of electronic structure calculations employs the density functional theory (DFT). In this approach, the electronic structure of atoms within the system is modeled with approximations to the Schrödinger equation, and these approximations are manifested via functionals that use the energy and electron density gradients to model electronic behavior.⁶⁰ These functionals include several quantities to describe the energy and electron density.⁶⁰ The exchange-correlation functional combines the energy of the inversion of two electrons within the wavefunction^{61,62} with the energy arising from the coupled motion of electrons throughout the system.^{62,63} The exchange-correlation functional can be further modified by addition of Hartree-Fock

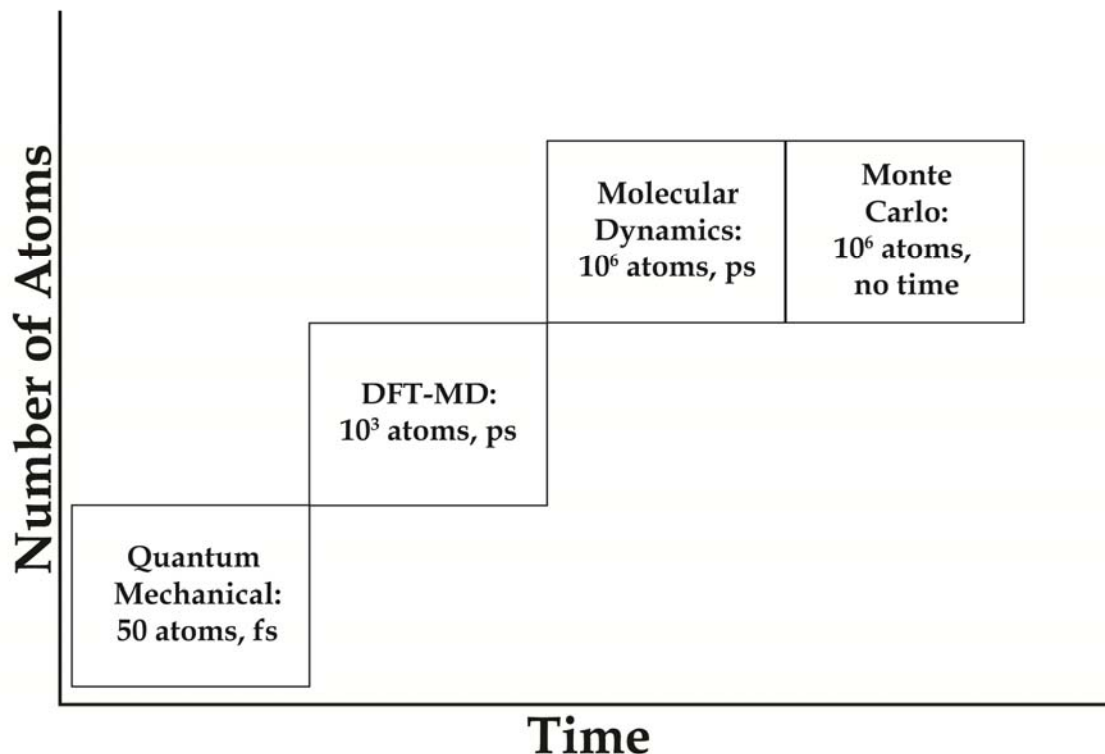


Figure 1-9: System size of computational methods versus simulation time. The number of atoms and timescales given in the boxes are the maxima possible for each computational method.

exchange, where electron exchange is described according to Hartree-Fock theory.⁶⁴ An advantage of DFT is that each electron has a maximum of four coordinates: x, y, z, and spin direction, while the electron density is described solely in terms of three coordinates, regardless of how many electrons are present within the system. The use of density functional theory (DFT) calculations has recently been reviewed,⁶⁵ and the functional used throughout this work blends exchange-correlation with Hartree-Fock exchange.⁶⁴⁻⁶⁸

DFT calculations have been employed to model geochemical reactions.^{23,24,26,27,50-}

⁵⁴ In order for these electronic structure calculations to be practical, model clusters are designed to effectively represent the system under study. Once a proper cluster has been chosen, these structures are energy-minimized to isolate a stable molecular geometry.

Clusters to represent the reactants, transition state, and products of a reaction are compared to describe the reaction mechanism, and the relative energies of the reactants and transition state give the barrier height for the reaction. The descriptions of the electronic structure within these calculations are derived from the gas-phase. However, the aqueous-phase can be modeled through the inclusion of a dielectric continuum⁶⁹ or a super-molecule, where explicit H₂O molecules around the reacting species are included.⁷⁰

Increasing the system size from molecular clusters to a unit-cell of a crystal can be attained via density functional theory molecular dynamics (DFT-MD) simulations. The electronic structure of atoms within the simulation cell is included, and motion of the atoms is also permitted. The electronic structure is represented by pseudo-potentials that divide the electrons into core and valence (*i. e.* non-reacting and reacting),⁷¹ and the band structure is evaluated via a projector-augmented wave (PAW) approximation.⁷²

The PAW approximation is an all-electron approach that includes full wavefunctions and blends augmented waves with pseudopotentials.⁷³ The augmented wave methods serve to fraction the electronic system into atom regions and envelope functions, which describe bonding between atoms. The electrons in the atom region are fractioned into valence and core, and the projector functions serve to describe the local nature of wavefunctions within the atomic region.⁷³ Despite these adjustments to evaluating electronic structure, chemical behaviors using all-electron methods are well replicated.⁷⁴

DFT-MD simulations provide an opportunity to investigate reactive processes and bulk characteristics within one simulation scheme, and one application for which this tool is particularly suited is the study of the aqueous-mineral interface. Reactions between

atoms are possible, and the inclusion of explicit H₂O molecules in solution permits representation of bulk water. Previous applications of these simulations for geochemical systems include modeling the adsorption of H₂O molecules to mineral surfaces,⁷⁵ the aqueous-mineral interface,^{76,77} the adsorption of ions from solution to the mineral surface,⁷⁸ and the vibrational spectrum of H₂O molecules adsorbed to the mineral surface.⁷⁹

Monte Carlo (MC) simulations are practical for system sizes of hundreds⁸⁰⁻⁸⁶ to thousands of particles.⁸⁷⁻⁹⁰ The fundamental design of this approach relies on the relative energies of the arrangement of particles in the system as they are moved in accordance with the simulation scheme under study. When the present arrangement is lower in energy than the initial, the system accepts the present arrangement. If instead the initial arrangement is lower, then two options are possible. The Boltzmann factor, $e^{-\Delta E/k_B T}$, is compared with a number between 0 and 1. If the Boltzmann factor is less than this fraction, the present arrangement is assumed. If on the other hand, the Boltzmann factor is greater than this fraction, then the initial arrangement of particles in the system remains.⁶⁰ This approach allows for the equivalent sampling of all possible configurations of the system, where the probability is weighted by the Boltzmann factor.⁹¹ Because MC simulations do not include a time parameter,⁹² those phenomena that proceed over a long timescale (*i. e.* ns or longer) can be studied. Geochemical processes such as the H-bonding networking on the mineral surface,⁸⁶ adsorption of water to the mineral surface^{80,84,85,90} or to the interlayer,⁸¹⁻⁸³ evolution of surface topography,⁸⁸

abiotic dissolution and precipitation,⁸⁹ biologically-mediated dissolution,⁸⁷ and pore-water fluid flow⁹³ have each been studied via MC simulations.

The last class of computational methods is molecular dynamics (MD) simulations, and this approach is feasible for systems similar in size to those for MC simulations. MD simulations use Newton's second law to describe the interaction of particles, and their behavior is studied with time. The electrostatic interactions of particles are modeled with potentials,⁹² which is in contrast with electronic structure and DFT-MD methods where the electronic structure of each particle is explicitly included.^{60,71,72} Specific characteristics of electronic behavior such as vibrational motion, Coulombic and Lennard-Jones interactions, and van der Waals interactions are also present in these simulations.⁶² Recent applications of MD simulations to geochemical systems include examining the silica-water interface as a function of surface hydroxylation,⁹⁴ the forsterite structure under high temperature and pressure conditions,⁹⁵ the adsorption of water to the forsterite surface,⁹⁶⁻⁹⁸ and pore water fluid flow.⁹³

The two computational methods that are employed in this work are density functional theory (DFT) calculations and DFT-MD simulations. DFT calculations are used to investigate the breaking of M–O ($M = \text{Mg}^{2+}$, Ni^{2+} , and Ca^{2+}) bonds within silicate molecular clusters to model the release of these metal ions from mineral surfaces. DFT-MD simulations are used to model the aqueous-mineral interface for forsterite (100) and (010) surfaces, and reactions between surface groups and between surface groups and species from solution permit a realistic model of the forsterite surface structure in an aqueous environment.

1.5 Expected Implications

The expected implications of this work are to provide a molecular scale understanding of the mechanisms through which dissolution reactions occur and to investigate contributing factors to experimental values. In particular, the barrier heights of metal release from mineral surfaces are calculated, and experimental data are combined with computational results to calculate rates and rate constants of dissolution. These two techniques relate to the need to understand how Mg^{2+} and Ca^{2+} are released from forsterite and anorthite during CO_2 storage via mineral trapping. The functional groups present on the forsterite surface at the water-mineral interface are also modeled, and this investigation provides insight into which sites on the surface are available to participate in dissolution reactions. These approaches are taken to explain experimental observations such as the dissolution rates of forsterite in Chapter 2, the dissolution rates and water-exchange rates of Ni-, Mg-, and Ca-silicate minerals in Chapter 3, and the difference between the stabilities and functional groups present on the forsterite (100) and (010) surfaces in Chapter 4. The use of computational techniques to study geochemical systems employs existing technology and relies upon models to adequately explain experimental phenomena. The work described is particularly unique for its inclusion of alkaline and transition metals as well as the methods chosen to model experimental observations.

1.6 References

- (1) Petit, J. R.; Jouzel, J.; Raynaud, D.; Barkov, N. I.; Barnola, J.-M.; Basile, I.; Bender, M.; Chappellaz, J.; Davis, M.; Delaygue, G.; Delmotte, M.; Kotlyakov, V. M.; Legrand, M.; Lipenkov, V. Y.; Lorius, C.; Pepin, L.; Ritz, C.; Saltzman, E.; Stievenard, M. *Nature* **1999**, 399, 429.
- (2) Tans, P.; NOAA/ESRL. Trends in Atmospheric Carbon Dioxide - Global, <http://www.esrl.noaa.gov/gmd/ccgg/trends/>.
- (3) NOAA/ESRL. Carbon Cycle Science, <http://www.esrl.noaa.gov/research/themes/carbon/>.
- (4) Giammar, D. E.; Bruant, R. G.; Peters, C. A. *Chem. Geol.* **2005**, 217, 257.
- (5) Jarvis, K.; Carpenter, R. W.; Windman, T.; Kim, Y.; Nunez, R.; Alawneh, F. *Environ. Sci. Technol.* **2009**, 43, 6314.
- (6) Roselle, G. T.; Baumgartner, L. P. *Geochim. Cosmochim. Ac.* **1995**, 59, 1539.
- (7) Matter, J. M.; Takahashi, T.; Goldberg, D. *Geochem. Geophys. Geosy.* **2007**, 8, Q02001.
- (8) Hanchen, M.; Prigiobbe, V.; Storti, G.; Seward, T. M.; Mazzotti, M. *Geochim. Cosmochim. Ac.* **2006**, 70, 4403.
- (9) Oelkers, E. H.; Gislason, S. R.; Matter, J. *Elements* **2008**, 4, 333.
- (10) Van Essendelft, D. T.; Schobert, H. H. *Ind. Eng. Chem. Res.* **2009**, 48, 2556.
- (11) Brantley, S. L. Reaction kinetics of primary rock-forming minerals under ambient conditions: fresh water geochemistry, weathering, and soils. In *Treatise on Geochemistry*; Turekian, K. K., Holland, H. D., Eds.; Pergamon Press: Oxford, 2003; Vol. 5; pp 73.
- (12) Neese, W. D. *Introduction to Mineralogy*; Oxford University Press: New York, NY, 2000.
- (13) Brantley, S. L. Kinetics of mineral dissolution. In *Kinetics of Water-Rock Interaction*; Brantley, S. L., Kubicki, J. D., White, A. F., Eds.; Springer: New York, NY, 2008; pp 151.
- (14) "Special Report on Carbon Capture and Storage," Intergovernmental Panel on Climate Change, 2005.
- (15) Koteas, C.; Kaiser, J. <http://www.geo.umass.edu/courses/geo311/systematic%20min.pdf>, 2008.
- (16) Birle, J. D.; Gibbs, G. V.; Moore, P. B.; Smith, J. V. *Am. Mineral.* **1968**, 53, 807.
- (17) Cerius²; Accelrys: San Diego, CA.
- (18) Materials Studio; Accelrys: San Diego, CA.
- (19) Phillips, M. W.; Ribbe, P. H.; Gibbs, G. V. *Am. Mineral.* **1973**, 58, 495.
- (20) Steinfeld, J. I. F., J. S.; Hase, W. L. *Chemical Kinetics and Dynamics*, 2nd ed.; Prentice Hall: Upper Saddle River, NJ, 1999.
- (21) Laidler, K. J. *Chemical Kinetics*, 3rd ed.; Pearson Education: Dehli, 1987.
- (22) Petrucci, R. H.; Harwood, W. S. *General Chemistry: Principles and Modern Applications*, 7th ed.; Prentice Hall: Upper Saddle River, 1997.
- (23) Nangia, S.; Garrison, B. J. *J. Phys. Chem. A* **2008**, 112, 2027.

- (24) Morrow, C. P.; Kubicki, J. D.; Mueller, K. T.; Cole, D. R. *J. Phys. Chem. C* **2010**, *114*, 5417.
- (25) Berger, G.; Cadore, E.; Schott, J.; Dove, P. M. *Geochim. Cosmochim. Ac.* **1994**, *58*, 541.
- (26) Xiao, Y.; Lasaga, A. C. *Geochim. Cosmochim. Ac.* **1994**, *58*, 5379.
- (27) Xiao, Y.; Lasaga, A. C. *Geochim. Cosmochim. Ac.* **1996**, *60*, 2283.
- (28) Icenhower, J. P.; Dove, P. M. *Geochim. Cosmochim. Ac.* **2000**, *64*, 4193.
- (29) Wallace, A. F.; Gibbs, G. V.; Dove, P. M. *J. Phys. Chem. A* **2010**, *114*, 2534.
- (30) Blum, A.; Lasaga, A. *Nature* **1988**, *331*, 431.
- (31) Pokrovsky, O. S.; Schott, J. *Geochim. Cosmochim. Ac.* **2000**, *64*, 3299.
- (32) Washton, N. M.; Brantley, S. L.; Mueller, K. T. *Geochim. Cosmochim. Ac.* **2008**, *72*, 5949.
- (33) Sanders, R. L.; Washton, N. M.; Mueller, K. T. *J. Phys. Chem. C* **2010**, *114*, 5491.
- (34) Luttge, A.; Bolton, E. W.; Lasaga, A. C. *Am. J. Sci.* **1999**, *299*, 652.
- (35) Olsen, A. A.; Rimstidt, J. D. *Geochim. Cosmochim. Ac.* **2008**, *72*, 1758.
- (36) Gislason, S. R.; Arnorsson, S. *Chem. Geol.* **1993**, *105*, 117.
- (37) Bickmore, B. R.; Wheeler, J. C.; Bates, B.; Nagy, K. L.; Eggett, D. L. *Geochim. Cosmochim. Ac.* **2008**, *72*, 4521.
- (38) Huertas, F. J.; Chou, L.; Wollast, R. *Geochim. Cosmochim. Ac.* **1999**, *63*, 3261.
- (39) Stumm, W.; Wollast, R. *Rev. Geophys.* **1990**, *28*, 53.
- (40) Rosso, J. J.; Rimstidt, J. D. *Geochim. Cosmochim. Ac.* **2000**, *64*, 797.
- (41) Furrer, G.; Stumm, W. *Geochim. Cosmochim. Ac.* **1986**, *50*, 1847.
- (42) Ludwig, C.; Casey, W. H.; Rock, P. A. *Nature* **1995**, *375*, 44.
- (43) Dove, P. M.; Han, N.; De Yoreo, J. J. *P. Natl. Acad. Sci. USA* **2005**, *102*, 15357.
- (44) Bandstra, J. Z.; Brantley, S. L. *Geochim. Cosmochim. Ac.* **2008**, *72*, 2587.
- (45) Awad, A.; van Groos, A. F. K.; Guggenheim, S. *Geochim. Cosmochim. Ac.* **2000**, *64*, 1765.
- (46) Oelkers, E. H.; Schott, J. *Geochim. Cosmochim. Ac.* **1995**, *59*, 5039.
- (47) Brunauer, S.; Emmett, P. H.; Teller, E. *J. Am. Chem. Soc.* **1938**, *60*, 309.
- (48) Sanders, R. L.; Washton, N. M.; Mueller, K. T. *J. Phys. Chem. C* **2010**, 5491.
- (49) Brantley, S. L.; Mellott, N. P. *Am. Mineral.* **2000**, *85*, 1767.
- (50) Pelmeshnikov, A.; Leszczynski, J.; Pettersson, L. G. M. *J. Phys. Chem. A* **2001**, *105*, 9528.
- (51) Criscenti, L. J.; Kubicki, J. D.; Brantley, S. L. *J. Phys. Chem. A* **2006**, *110*, 198.
- (52) Nangia, S.; Garrison, B. J. *Mol. Phys.* **2009**, *107*, 831.
- (53) Morrow, C. P.; Nangia, S.; Garrison, B. J. *J. Phys. Chem. A* **2009**, *113*, 1343.
- (54) Morrow, C. P.; Olsen, A. A.; Kubicki, J. D. *J. Phys. Chem. C* **2010**, submitted.
- (55) Davis, M. C.; Brouwer, W. J.; Wesolowski, D. J.; Anovitz, L. M.; Lipton, A. S.; Mueller, K. T. *Phys. Chem. Chem. Phys.* **2009**, *11*, 7013.
- (56) Pokrovsky, O. S.; Schott, J. *Geochim. Cosmochim. Ac.* **2000**, *64*, 3313.
- (57) Brantley, S. L.; Conrad, C. F. Analysis of Rates of Geochemical Reactions. In *Kinetics of Water-Rock Interaction*; Brantley, S. L., Kubicki, J. D., White, A. F., Eds.; Springer: New York, NY, 2008; pp 1.
- (58) Casey, W. H.; Westrich, H. R. *Nature* **1992**, *355*, 157.

- (59) Westrich, H. R.; Cygan, R. T.; Casey, W. H.; Zemitis, C.; Arnold, G. W. *Am. J. Sci.* **1993**, 293, 869.
- (60) Jensen, F. *Introduction to Computational Chemistry*; John Wiley and Sons, Inc.: New York, 1998.
- (61) Levine, I. N. *Quantum Chemistry*, 5th ed.; Prentice Hall: Upper Saddle River, 2000.
- (62) Atkins, P.; de Paula, J. *Physical Chemistry*, 7th ed.; W. H. Freeman and Company: New York, 2002.
- (63) Foresman, J. B.; Frisch, A. *Exploring Chemistry with Electronic Structure Methods*, 2nd ed.; Gaussian, Inc.: Pittsburgh, 1996.
- (64) Becke, A. D. *J. Chem. Phys.* **1993**, 98, 1372.
- (65) Sousa, S. F.; Fernandes, P. A.; Ramos, M. J. *J. Phys. Chem. A* **2007**, 111, 10439.
- (66) Vosko, S. H.; Wilk, L.; Nusair, M. *Can. J. Phys.* **1980**, 58, 1200.
- (67) Lee, C.; Yang, W.; Parr, R. G. *Phys. Rev. B* **1988**, 37, 785.
- (68) Becke, A. D. *J. Chem. Phys.* **1993**, 98, 5648.
- (69) Cancès, E.; Mennucci, B.; Tomasi, J. *J. Chem. Phys.* **1997**, 107, 3032.
- (70) Keith, T. A.; Frisch, M. J. Inclusion of explicit solvent molecules in a self-consistent-reaction field model of solvation. In *ACS Symposium Series*; Smith, D. A., Ed.; American Chemical Society: Washington, D.C., 1994; Vol. 569; pp 22.
- (71) Hafner, J. *Comput. Phys. Commun.* **2007**, 177, 6.
- (72) Blochl, P. E. *Phys. Rev. B* **1994**, 50, 17953.
- (73) Blochl, P. E.; Forst, C. J.; Schimpl, J. B. *Mater. Sci.* **2003**, 26, 33.
- (74) Hafner, J.; Wolverton, C.; Ceder, G. *MRS Bull.* **2006**, 31, 659.
- (75) Bandura, A. V.; Sykes, D. G.; Shapovalov, V.; Troung, T. N.; Kubicki, J. D.; Evarestov, R. A. *J. Phys. Chem. B* **2004**, 108, 7844.
- (76) Tunega, D.; Gerzabek, M. H.; Lischka, H. *J. Phys. Chem. B* **2004**, 108, 5930.
- (77) Kubicki, J. D.; Paul, K. W.; Sparks, D. L. *Geochem. T.* **2008**, 9, 4.
- (78) Zhang, Z.; Fenter, P.; Cheng, L.; Sturchio, N. C.; Bedzyk, M. J.; Predota, M.; Bandura, A.; Kubicki, J. D.; Lvov, S. N.; Cummings, P. T.; Chialvo, A. A.; Ridley, M. K.; Benezeth, P.; Anovitz, L.; Palmer, D. A.; Machesky, M. L.; Wesolowski, D. J. *Langmuir* **2004**, 20, 4954.
- (79) Kumar, N.; Neogi, S.; Kent, P. R. C.; Bandura, A. V.; Kubicki, J. D.; Wesolowski, D. J.; Cole, D. R.; Sofo, J. O. *J. Phys. Chem. C* **2009**, 113, 13732.
- (80) Delville, A. *J. Phys. Chem.* **1995**, 99, 2033.
- (81) Skipper, N. T.; Chang, F. R. C.; Sposito, G. *Clay Clay Miner.* **1995**, 43, 285.
- (82) Skipper, N. T.; Sposito, G.; Chang, F. R. C. *Clay Clay Miner.* **1995**, 43, 294.
- (83) Sposito, G.; Skipper, N. T.; Sutton, R.; Park, S. H.; Soper, A. K.; Greathouse, J. A. *P. Natl. Acad. Sci. USA* **1999**, 96, 3358.
- (84) Croteau, T.; Bertram, A. K.; Palley, G. N. *J. Phys. Chem. A* **2008**, 112, 10708.
- (85) Croteau, T.; Bertram, A. K.; Patey, G. N. *J. Phys. Chem. A* **2009**, 113, 7826.
- (86) Nangia, S.; Garrison, B. J. *J. Phys. Chem. C* **2010**, 114, 2267.
- (87) Luttge, A.; Zhang, L.; Nealson, K. H. *Am. J. Sci.* **2005**, 305, 766.
- (88) Stubner, K.; Jonckheere, R.; Ratschbacher, L. *Geochim. Cosmochim. Ac.* **2008**, 72, 3184.
- (89) Nangia, S.; Garrison, B. J. *J. Am. Chem. Soc.* **2009**, 131, 9538.

- (90) Croteau, T.; Bertram, A. K.; Palley, G. N. *J. Phys. Chem. A* **2010**, *114*, 2171.
- (91) Alder, B. J.; Ceperley, D. M.; Pollock, E. L. *Accounts Chem. Res.* **1985**, *18*, 268.
- (92) Leach, A. R. *Molecular Modeling: Principles and Applications*; Pearson Prentice Hall: New York, 2001.
- (93) Meakin, P.; Tartakovsky, A. M. *Rev. Geophys.* **2009**, *47*.
- (94) Argyris, D.; Cole, D. R.; Striolo, A. *J. Phys. Chem. C* **2009**, *113*, 19591.
- (95) Martin, G. B.; Spera, F. J.; Ghiorso, M. S.; Nevins, D. *Am. Mineral.* **2009**, *94*, 693.
- (96) Watson, G. W.; Oliver, P. M.; Parker, S. C. *Phys. Chem. Miner.* **1997**, *25*, 70.
- (97) de Leeuw, N. H.; Parker, S. C.; Catlow, C. R. A.; Price, G. D. *Phys. Chem. Miner.* **2000**, *27*, 332.
- (98) Stimpfl, M.; Walker, A. M.; Drake, M. J.; de Leeuw, N. H.; Deymier, P. *J. Cryst. Growth* **2006**, *294*, 83.

Chapter 2

A Description of Mg^{2+} Release from Forsterite using Ab-Initio Methods

Reproduced with permission from:

Morrow, C. P.; Kubicki, J. D.; Mueller, K. T.; Cole, D. R. *Barbara J. Garrison Festschrift: Journal of Physical Chemistry C*, 2010, 114, 5147-5428. Copyright 2010 American Chemical Society.

2.1 Introduction

The work described in Chapter 2 employs quantum mechanical calculations to model the release of Mg^{2+} from sites on the forsterite mineral surface. Molecular cluster analogs of these surface sites allow for tractable computation times, and the varying protonation states of sites are included. The reaction mechanism and the barrier height for Mg^{2+} release from each type of site are reported. The barrier heights are used to calculate rate constants for Mg^{2+} release from each type of site, and these are combined with experimental data to calculate a rate for Mg^{2+} release from the forsterite surface versus pH.

In order to understand the dissolution of forsterite, one begins with a description of the forsterite mineral structure (**Figure 2-1**). The bulk structure of forsterite has octahedrally coordinated Mg bound to six oxygen atoms, each of which is bound to a Si atom. The network continues, alternating between tetrahedrally-coordinated Si and octahedrally-coordinated Mg atoms connected via bridging oxygen atoms (O).^{19,20} The release of Mg species to solution is triggered by the breaking of a terminal Mg–O bond linking the Mg to the surface, and in this state, Mg is octahedrally-coordinated with the O

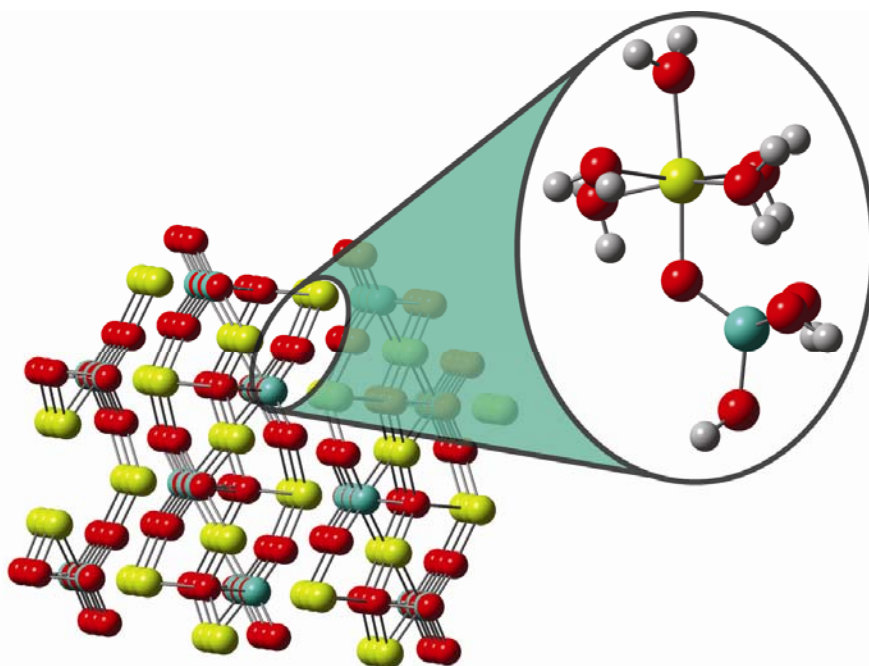


Figure 2-1: Forsterite (100) surface where a Mg–O–Si surface site has been extracted to depict the molecular cluster model. The magnesium atoms are yellow, the oxygen atoms are red, the silicon atoms are turquoise, and the hydrogen atoms are white.

and five H₂O molecules as is shown by the molecular cluster in the inset to **Figure 2-1**. Once released from the surface, Mg returns to six-fold coordination when an incoming H₂O molecule replaces the O for the sixth position around the Mg center. Descriptions of this process based on empirical studies are both numerous and extensive and are outlined below.

In a recent review,²¹ the dissolution rates of a number of silicate minerals, including forsterite, were compared as a function of pH. For silica, the dissolution rate is at a minimum at neutral pH and increases in acidic and basic pH ranges, but for forsterite, most recent work^{5,7-11,21} supports a linear decrease in the Mg²⁺ release rate with an increase in pH as shown in **Figure 2-2**.¹² The experiments performed by Wogelius and Walther⁶ and Blum and Lasaga²² showed an increase of the dissolution rate in the basic

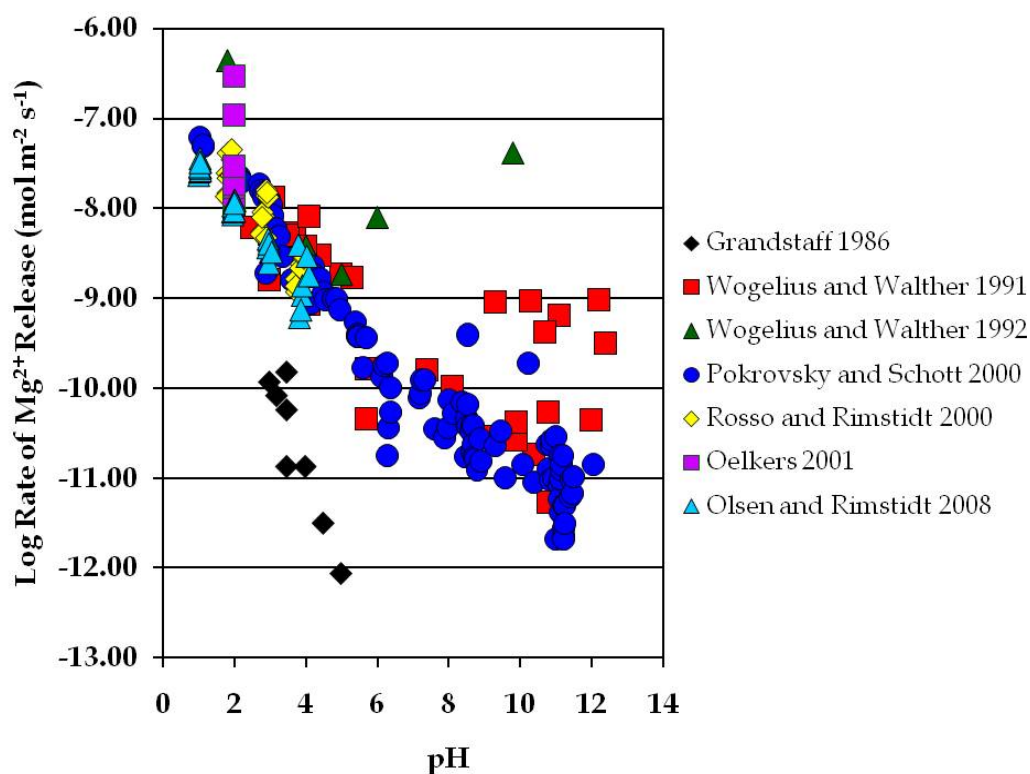


Figure 2-2: Rates of Mg^{2+} release from the forsterite surface plotted as the log of the rate ($\text{mol m}^{-2} \text{s}^{-1}$) versus the pH.⁵⁻¹¹ The data in this figure were taken from the ChemXSeer chemical kinetics database.¹²

region. Blum and Lasaga explained that their U-shaped dissolution rate curve analogous to that observed for silica may indicate that the deprotonation of Si sites, defined here as Si–O–Mg sites, on the forsterite surface is the most prevalent hydrolysis surface reaction at basic pH. However, the validity of the studies by Wogelius and Walther⁶ and Blum and Lasaga²² have been questioned because neither set of experiments was performed in the steady-state region of dissolution nor was a statistically adequate number of data collected for the dissolution rate in the basic pH region.⁸ Further, the ionic strength of the solutions that Wogelius and Walther used during their dissolution studies of forsterite could have produced an increase in surface charge²³ which may lead to an increase in dissolution rate.^{24,25}

A recent study by Rosso and Rimstidt⁹ investigated the effect of H_3O^+ adsorption onto the forsterite surface in the pH range of 1 to 3, and the link between H_3O^+ catalysis and forsterite dissolution was explained. They determined that two H atoms from H_3O^+ adsorb to O atoms in two adjacent Mg octahedra which weakens the Mg–O bonds. This description explains the observation that two H^+ replace Mg^{2+} in the surface structure during dissolution.²⁰ Further, this allows H_2O molecules from solution to more easily exchange for the O atoms in the mineral structure, and the substitution causes the surface network to open. After five H_2O molecules have replaced the O atoms in the octahedra, the Mg is hexa-coordinated to five H_2O molecules and one O, and this last step before release to solution²⁶ is amenable to a molecular-scale interrogation of the forsterite dissolution process.

In order to explain experimental observations with a molecular-level understanding, ab-initio calculations have recently been employed to describe mechanisms for hydrolysis reactions occurring at the mineral surface.^{2,4,24,25} In these studies, molecular cluster-sized analogs of mineral units are used to represent reaction sites on the surface, and this approach has replicated experimental trends for both silica² and aluminosilicate minerals.⁴ The use of molecular clusters enables the description of the central phenomenon in a chemical process without the computational burden of atoms that do not contribute directly to the reaction in question.²⁴ This facilitates a molecular description of dissolution where the molecular cluster serves as a site on the surface, and H_3O^+ , H_2O , or OH^- is the second reactant. At every pH, a distribution of each type of site is present.

One of the challenges in choosing an ab-initio approach to study geochemical reactions is that the calculations are often performed in the gas-phase and thus with no solvent explicitly present, while the reactions occur at the water-surface interface in aqueous media. Including a solvation continuum model is arguably necessary because it would yield insight into how effectively the gas-phase calculations represent the chemical process under study, and the inclusion of solvation effects has recently been employed in the investigation of species with geochemical relevance.^{27,28} In addition, comparisons of ab-initio results with experimental data are more meaningful when solvation effects are included because they allow for the identification of any results which are artifacts of performing the original calculations in the gas-phase. The use of a continuum model is one tool for the inclusion of a solvation approach without the use of explicit H₂O molecules.^{27,29}

The aim of this study is to examine dissolution from Mg²⁺ sites, defined as Mg–O–Si sites, on the forsterite surface using a molecular cluster approach via ab-initio calculations. The reaction mechanisms are described along with energy profiles that present the barrier heights for these reactions in gas-, single-point aqueous-, and energy-minimized aqueous-phases. Rate constants for these reactions as well as the rate for the release of Mg²⁺ from Mg–O–Si sites are also presented. These computational results are compared with experimental data.

2.2 Computational Methods

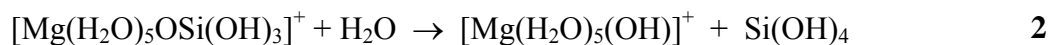
Molecular clusters were extracted from Mg–O–Si sites on the forsterite (100) surface using the Cerius² database,³⁰ and an example of a cluster is shown in the inset of

Figure 2-1. Here a Mg^{2+} is bonded to a O which is in turn bonded to a Si atom. The Si atom is bonded to three OH groups which are meant to represent the bonds to the bulk crystal, and this is in accord with the finding that bonds breaking at the surface experience minimal contribution from other atoms deeper in the surface.²⁴ The hexacoordination of the Mg^{2+} is satisfied by five H_2O molecules in its first hydration sphere, and the cluster is reacted with a H_2O molecule to simulate dissolution. **Figure 2-3** depicts a model molecular cluster with a H_2O molecule which represents a general setup for each of the calculations presented here. In each of these clusters, the protonation or deprotonation of a surface site is also considered to represent acidic and basic conditions, respectively. The presence of an H^+ on the O represents a protonated site, and for the neutral and deprotonated sites, no H^+ is included. In the deprotonated site reaction, the absence of an H^+ on the surface site is represented by reacting the molecular cluster with an OH^- rather than a H_2O molecule.

The hydrolysis of Mg–O–Si sites in each protonation state is represented by the following reactions, corresponding to protonated, neutral, and deprotonated Mg–O–Si sites, respectively. The protonated Mg–O–Si site reaction is **(2-1)**:



where presence of an H^+ on the O denotes a protonated site. The neutral Mg–O–Si site reaction is described by two possible reactions **(2-2)**:



and **(2-3)**:

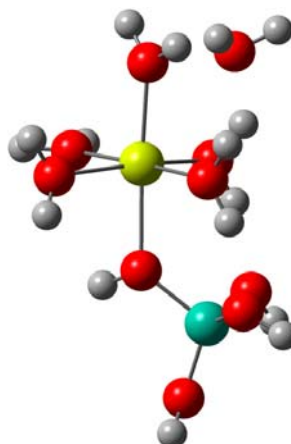
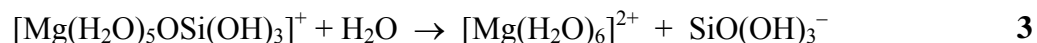
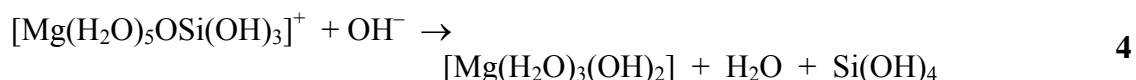


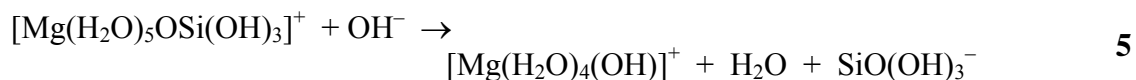
Figure 2-3: The model molecular cluster used to represent Mg–O–Si sites on the forsterite surface. The color scheme is the same as **Figure 2-1**.



where the O is not protonated, and the products may include either a hydroxylated surface site, denoted by $\text{Si}(\text{OH})_4$, or a deprotonated surface site, denoted by $\text{SiO}(\text{OH})_3^-$. The deprotonated Mg–O–Si site reaction is also described by two possible reactions (**2-4**):



and (**2-5**):



where the O is not protonated as with the neutral site reaction, and the products may include either a hydroxylated surface site, denoted by $\text{Si}(\text{OH})_4$, or a deprotonated surface site, denoted by $\text{SiO}(\text{OH})_3^-$. In each calculation, the overall charge of the system is included, and the contribution of each species to the overall charge is shown in **Reactions 2-1, 2-2, 2-3, 2-4, and 2-5**.

A density functional theory (DFT) approach was chosen for this study because of enhanced computational feasibility as well as successful use of these methods in the literature to calculate the hydrolysis reaction mechanisms for mineral dissolution.^{2,4,24,25} The B3LYP functional is a hybrid density functional which includes exchange-correlation,³¹⁻³⁴ gradient correction,^{33,34} and a fraction of Hartree-Fock exchange.³⁵ The employment of the 6-31+G(d,p) basis set is reasonable in this application because it is appropriate for Mg^{2+} complexes,³⁶ and *p* orbitals were added in the event that a H^+ transfer occurred in the course of any of the reactions studied.

The structures of the reactants for each reaction were optimized without constraints in the gas-phase, and then potential energy surface (PES) scans of the Mg–O distance were performed to determine estimates for both the transition states and products which were in turn optimized. Reactant and product species had no negative frequencies, and possible transition states were identified by the presence of one negative frequency that corresponded to the breaking of the Mg–O bond. A second set of PES scans was performed where the distance between the incoming H_2O molecules and the Mg^{2+} was decreased in order to calculate the barrier height for the absorption of H_2O by Mg^{2+} . The energy profiles were constructed by using the reactant energy as the reference state and comparing the energies of the transition states and products to the energy of the reactants. All calculations were performed with Gaussian 03,³⁷ and all molecular cluster figures were visualized with GaussView 4.³⁸

After the initial reaction mechanism was determined using gas-phase calculations, aqueous-phase calculations were performed using the self-consistent reaction field (SCRF) method through the integral equation formalism polarized continuum model

(IEFPCM)³⁹ with water as the solvent. Single-point aqueous-phase calculations were performed where the gas-phase structures were used as input, and the corresponding energies were calculated. No frequency calculations were performed because the gas-phase structures do not correspond to a potential energy minimum once the continuum solvation model is applied.

Finally, the reactants from the gas-phase calculations were optimized without constraints using the IEFPCM, and PES scans of the Mg–O distance as well as the approach of the H₂O to the Mg²⁺ were performed in a manner analogous to the gas-phase calculations. The reactants and products for each reaction yielded no negative frequencies, whereas optimized transition states in the aqueous-phase calculations had a single negative frequency corresponding to the breaking of the Mg–O bond.

In an effort to determine whether each hydrolysis reaction is spontaneous, the Gibbs free energy change for each reaction was calculated. In the gas-phase, the Gibbs free energy of each structure includes a zero-point energy (ZPE) correction as well as a correction to the thermal energy. Partition functions that describe the translational, electronic, rotational, and vibrational motion are incorporated into the entropy term, while the enthalpy is the atomic energy of the structure with the addition of a thermal correction factor.⁴⁰

In the continuum calculations, the Gibbs free energy is calculated with respect to contributions from the presence of the solvent continuum and the solute structure in the gas phase. The Gibbs free energy includes this electrostatic description of the solute/solvent interaction and a “cavitation free energy” contribution, which calculates the amount of energy required to form the cavity and includes the surface tension, the

surface area of the solute cavity, and the ratio of the molar volume of the solute to molar volume of the solvent.⁴¹ The temperature is treated as 298.15 K,⁴² and the free energy from the reaction was determined as **(2-6)**:

$$\Delta G_{reaction} = \Delta G_{products} - \Delta G_{reactants} \quad \mathbf{6}$$

where $\Delta G_{reaction}$ is the Gibbs free energy for the reaction, $\Delta G_{products}$ is the Gibbs free energy for the products, and $\Delta G_{reactants}$ is the Gibbs free energy for the reactants.

The Gibbs free energy quantities from the aqueous-phase calculations on the gas-phase structures relied upon additional corrections, as some of the correction quantities are calculated for the gas-phase only. Thus, the Gibbs free energy for the single-point aqueous-phase calculations was calculated according to **(2-7)**:

$$\Delta G_{reaction} = (\Delta G_{products} + CP_{gas-phase}) - (\Delta G_{reactants} + CR_{gas-phase}) \quad \mathbf{7}$$

where $CP_{gas-phase}$ is the Gibbs free energy correction from the gas-phase for the products and $CR_{gas-phase}$ is the Gibbs free energy correction for the reactants, and this approach was used because the gas-phase structures were used in these calculations.

The Gibbs free energy for the reactions using optimized aqueous-phase structures was determined as **(2-8)**:

$$\Delta G_{reaction} = (\Delta G_{products} + CP_{aqueous-phase}) - (\Delta G_{reactants} + CR_{aqueous-phase}) \quad \mathbf{8}$$

where $CP_{aqueous-phase}$ is the correction to the products in the aqueous-phase and $CR_{aqueous-phase}$ is the correction to the free energy of the reactants in the aqueous-phase. The Gibbs free energy values for the reactions in gas-phase, single-point aqueous-phase, and optimized aqueous-phase were used to determine if each reaction is spontaneous.

Once the reactant and transition state had been optimized in the gas- and aqueous-phases for each reaction, the frequency output files were used to calculate the rate constant using TheRate⁴³ via **Equation 2-9**:

$$k_T = AT^n e^{-(E_a/RT)} \quad 9$$

where A is the pre-exponential factor, T is the temperature in K, n is the exponential order of the temperature-dependence of A , E_a is the activation energy, and R is the gas constant.^{43,44} Transition state theory (TST) was employed, and the rate constant was calculated at 298K. The value of n was set to 0.0010 to eliminate the temperature dependence of A . For the single-point aqueous-phase calculations, the barrier heights were inserted into **Equation 2-9** using the A and n quantities from the calculations for the gas-phase reaction because the structures were the same.

The calculated rate constants for Mg–O–Si sites in each protonation state were used to calculate the release rate of Mg^{2+} from the forsterite surface according to the model that the surface contains a fraction of sites in each protonation state at every pH and that the number of OH groups available on the surface also contributes to the rate.² This model is given by **(2-10)**:

$$\text{Rate} = \rho(\theta_{\text{prot}}k_{\text{prot}} + \theta_{\text{neut}}k_{\text{neut}} + \theta_{\text{deprot}}k_{\text{deprot}}) \quad 10$$

where ρ (in units of mol m^{-2}) is the reactive site density and thus the number of OH groups on the surface, θ_i is the fraction of each site on the surface at a given pH, and k_i (in s^{-1}) is the rate constant for each i type of site.² Thus, the rate of Mg^{2+} release is proportional to the number of OH sites on the surface as well as the sum of the contribution from sites of each protonation state on the surface.² The density of reactive

sites, ρ , was extracted from the forsterite (100) surface provided in the Cerius² database³⁰ where the number of OH groups on each Si and each Mg²⁺ on the surface were totaled. The fraction of protonated, neutral, and deprotonated sites, θ_i , was determined from the data of Pokrovsky and Schott where the apparent surface charge was plotted versus pH, and the concentration of H⁺ adsorbed to the surface can be obtained from (2-11):

$$\sigma_{app} = F[H^+_{ads}]s^{-1} \quad 11$$

where σ_{app} is the apparent surface charge, F is Faraday's constant, and s is the surface area of the mineral sample.²³

Once the amount of H⁺ or OH⁻ adsorbed to the surface was determined, the number of remaining neutral and deprotonated or protonated sites was estimated. The amount of adsorbed H⁺ was treated as the number of protonated Mg–O–Si sites, and the number of deprotonated sites was set at zero according to the pH of zero surface charge of Pokrovsky and Schott.²³ The number of neutral Mg–O–Si sites was determined simply from (2-12):

$$\theta_{neut} = 1 - \theta_{prot} - \theta_{deprot} \quad 12$$

where θ_{neut} is the number of neutral Mg–O–Si sites, θ_{prot} is the number of protonated Mg–O–Si sites, and θ_{deprot} is the number of deprotonated Mg–O–Si sites on the surface at any given pH. These values were then used to calculate the rate of Mg²⁺ release from the surface according to **Equation 2-10**.

2.3 Results and Discussion

2.3.1 Hydrolysis of Mg–O–Si Sites

2.3.1.1 Reaction Coordinate

Two possibilities exist for the reaction coordinate of Mg–O–Si hydrolysis reactions: lengthening of the Mg–O bond and decreasing the Mg–O distance between the incoming H₂O molecule and the Mg²⁺. PES scans along the latter reaction coordinate led to H₂O exchange around the Mg²⁺ rather than hydrolysis of the Mg–O bond, suggesting that Mg²⁺ extraction from the surface can be de-coupled from H₂O exchange.

A representative scan for the exchange of H₂O molecules around the Mg²⁺ in the neutral site is shown in **Figure 2-4**. The reactant complex (RC), transition state (TS), and product complex (PC) structures shown in **Figure 2-4a** were taken directly from the PES scan, and the energy for each point along the scan is shown in **Figure 2-4b**. The H₂O molecule from the second hydration sphere is circled in blue, while the H₂O molecule that is originally bonded to the Mg²⁺ and will be replaced is circled in green (**Figure 2-4a**). In the RC, the H₂O molecule in the second hydration sphere is 3.74 Å from the Mg²⁺, and the H₂O molecule in the first hydration sphere is 2.22 Å from the Mg²⁺. As the H₂O molecule from the second hydration sphere approaches the Mg²⁺, the bond between the Mg²⁺ and the H₂O in the first hydration sphere begins to lengthen. In the TS, this bond length is 2.36 Å, while the H₂O from the second hydration sphere is 2.44 Å from the Mg²⁺. Once these two H₂O molecules have exchanged, the Mg–H₂O bond is 2.14 Å, and the H₂O that is now in the second hydration sphere is 3.49 Å from the Mg²⁺. The energy profile shows that the barrier height for this process is 41 kJ/mol. Although this

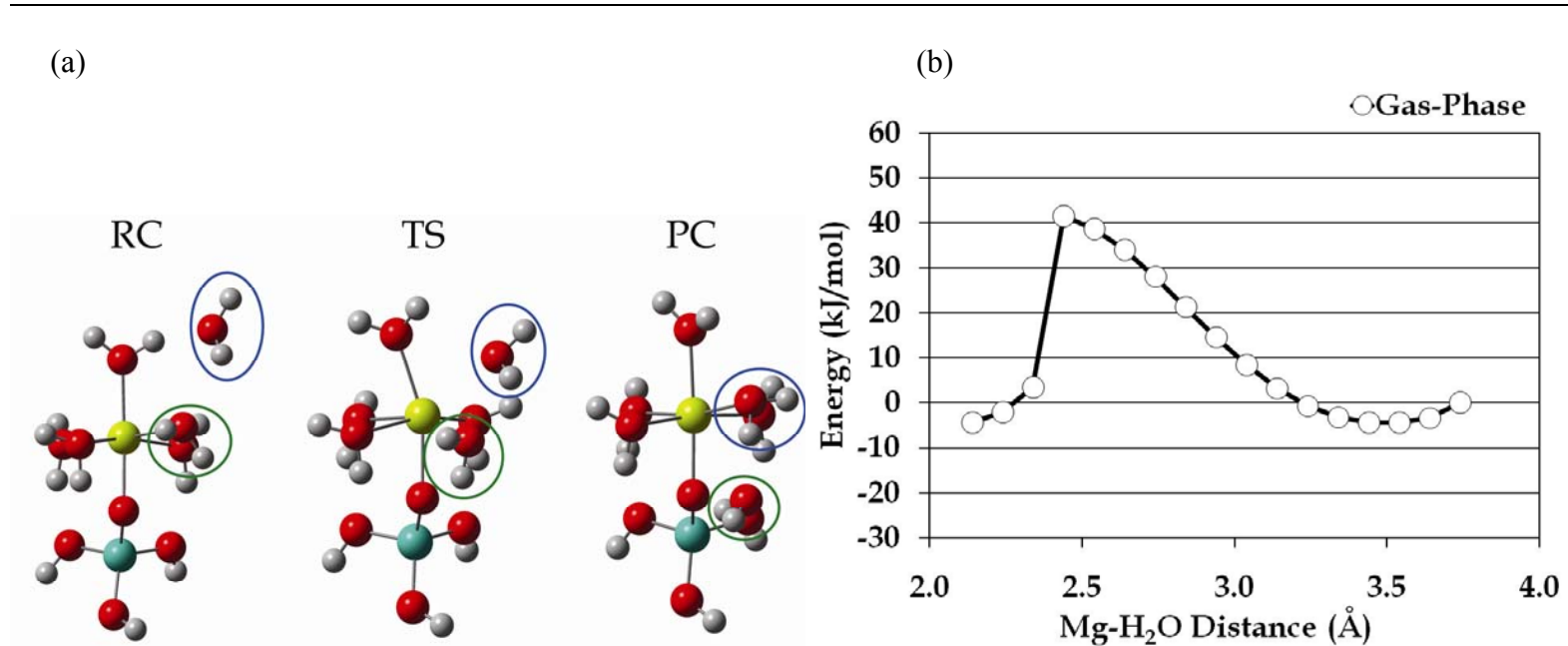


Figure 2-4: The PES scan of H₂O exchange around a neutral Mg–O–Si site. (a) The gas phase RC, TS, and PC species from the scan. The H₂O molecule circled in blue represents the H₂O molecule from the second hydration sphere that will bond with the Mg²⁺ in the products, and the H₂O molecule in the green circle will be released from the first hydration sphere of Mg²⁺. (b) The energy (kJ/mol) of each point on the scan is plotted against the Mg–H₂O distance of the incoming H₂O molecule, and thus the progression of the scan is from right to left.

process occurs regularly in solution,⁴⁵ the key to understanding dissolution behavior is to determine how the Mg–O bond is broken, resulting in the leaching of Mg²⁺ species to solution. These scans show that decreasing the H₂O–Mg distance does not contribute to the release of Mg²⁺ species from the forsterite surface.

On the other hand, PES scans of the Mg–O distance showed that a change in this parameter does lead to the release of Mg²⁺ species from the surface. The products for each of these scans of Mg–O bond break contained a penta-coordinated Mg²⁺ species where the incoming H₂O molecule had not yet been absorbed. For this reason, a second set of scans was performed to determine how this absorption process occurs. After both sets of scans were completed, further optimization of possible RC, TS, and PC structures from those PES scans led to the isolation of the stationary points on the reaction profile, and both sets of scans are included here.

2.3.1.2 Energy Profiles

The potential energy surface scans and energy profiles for each reaction are presented here for the gas-phase, single-point aqueous-phase, and energy-minimized aqueous-phase. The PES scans represent the energy for the complex at each point along the scan compared to the RC, for which the energy is set as zero. The energy profiles represent the energy of the optimized RC, TS, and PC species, where the RC energy is again set as zero. The PES scans in **Figures 2-5, 2-6, and 2-7** were used to gain a more complete understanding of how each reaction occurs, and they represent the two steps in the release of Mg²⁺ from the surface: the breaking of the Mg–O bond and the absorption of the incoming H₂O to form a hexa-coordinated product. The barrier heights for these

reactions are taken from the energy profiles and are also shown in **Figures 2-5, 2-6, and 2-7**, and the reaction with the highest barrier height varies between phases. For the gas-phase calculations, the barrier heights increase in the order of protonated, deprotonated, and neutral site reactions, whereas for the energy-minimized aqueous-phase calculations, the deprotonated site reaction has the lowest barrier height. The barrier heights for the protonated, neutral, and deprotonated sites in each of the three phases are summarized in **Table 2-1**, and the bond lengths given in the text are those for the gas-phase and are meant to be a guide for the reader.

The PES scan of the Mg–O distance and then the H₂O–Mg²⁺ distance for the protonated reaction in the gas-phase is included in **Figure 2-5**. The estimates for the RC and the TS from this scan are <1 kJ/mol different in energy which shows the structures derived from the scan are good estimates of the optimized structures. However, the PC from the PES scan of the Mg–O distance has a penta-coordinated Mg²⁺ with the incoming H₂O H-bonded to the axial H₂O molecule and an equatorial H₂O molecule. The scan of the H₂O–Mg²⁺ distance shows that the H-bonding network opens up to allow the H₂O from the second hydration sphere to further approach the Mg²⁺. The PC from the second scan is a hexaaqua Mg²⁺ ion and is lower in energy than the penta-coordinated conformation by 8 kJ/mol. The aqueous-phase PES scans follow the same behavior as the gas-phase.

The gas-phase, single-point aqueous-phase, and energy-minimized aqueous-phase energy profiles for the protonated reaction are also shown in **Figure 2-5**. The intact Mg–O bond length is 2.17 Å, and as the bond begins to lengthen, the negative frequency in the TS corresponds to the Mg–O bond breakage at 3.07 Å. The bond is fully broken in

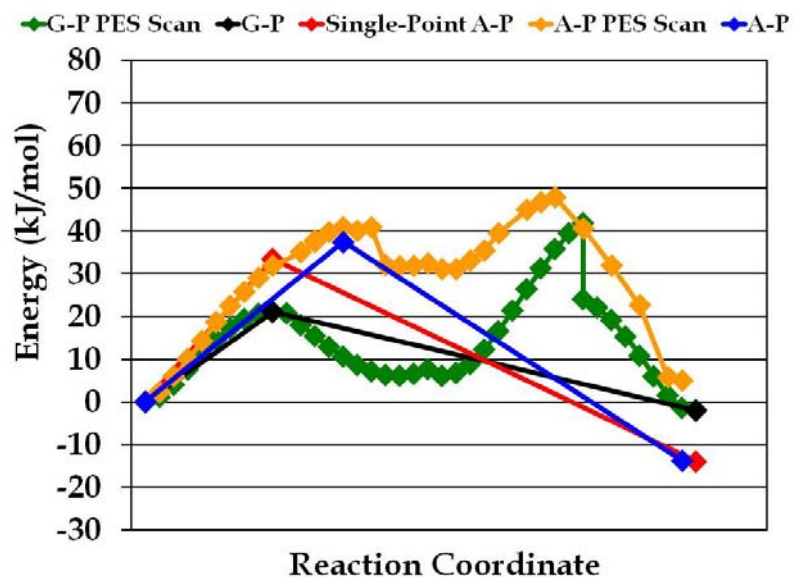


Figure 2-5: The energy plot for the protonated Mg–O–Si site reaction. The gas-phase potential energy scan (G-P PES Scan) is green, and the aqueous-phase potential energy scan (A-P PES Scan) is orange. The energy profiles comparing the RC, TS, and PC in the gas-phase (G-P), single-point aqueous-phase (Single-Point A-P), and energy-minimized aqueous-phase (A-P) are black, red, and blue, respectively.

the product complex where the Mg–O distance is 4.14 Å, and the barrier heights for this reaction are 21 kJ/mol in the gas-phase, 33 kJ/mol in the single-point aqueous-phase, and 37 kJ/mol in the energy-minimized aqueous-phase calculations.

The PES scans for the neutral reaction are shown in **Figure 2-6**. As with the protonated site reaction, the products for the neutral reaction in the scan include a H₂O molecule and a penta-coordinated Mg²⁺. In the PES scan of the H₂O–Mg²⁺ distance, the incoming H₂O breaks the H-bond network with the two H₂O molecules with which it is interacting, and as with the protonated site, the H₂O molecules bonded to Mg²⁺ rearrange to allow the incoming H₂O molecule to bond with the Mg²⁺. As before, the hexa-coordinated Mg²⁺ species is lower in energy than the penta-coordinated Mg²⁺ by more than 20 kJ/mol. This same phenomenon is observed in the gas-phase as well but the difference in energy is 6 kJ/mol.

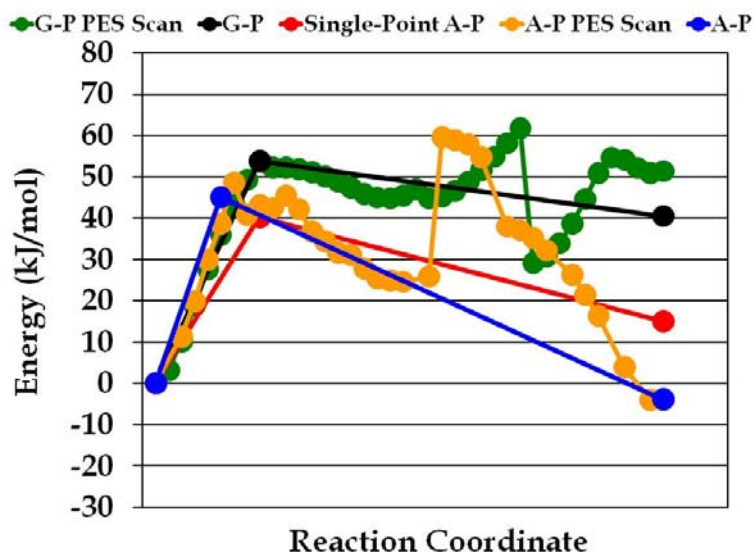


Figure 2-6: The energy plot for the neutral Mg–O–Si site reaction where the labeling and color scheme are the same as **Figure 2-5**

The energy profile for the neutral site reaction is given in **Figure 2-6**, and the gas-phase, single-point aqueous-phase, and energy-minimized aqueous-phase results are included. The initial Mg–O bond distance in the RC is 1.98 Å, shorter than in the protonated state because here the O is not protonated. As the bond lengthens, the breaking of the Mg–O bond in the TS occurs at a Mg–O distance of 2.78 Å. The Mg–O distance continues to lengthen until the PC where it is 3.79 Å, and the barrier heights for this reaction are 54 kJ/mol in the gas-phase, 40 kJ/mol in the single-point aqueous-phase, and 44 kJ/mol in the energy-minimized aqueous-phase calculations, respectively.

The PES scans for the deprotonated site reaction are shown in **Figure 2-7**. The gas-phase scan mimics the energy values for the RC and TS for this reaction in that they are less than 1 kJ/mol apart for each structure. The aqueous-phase is different in that the

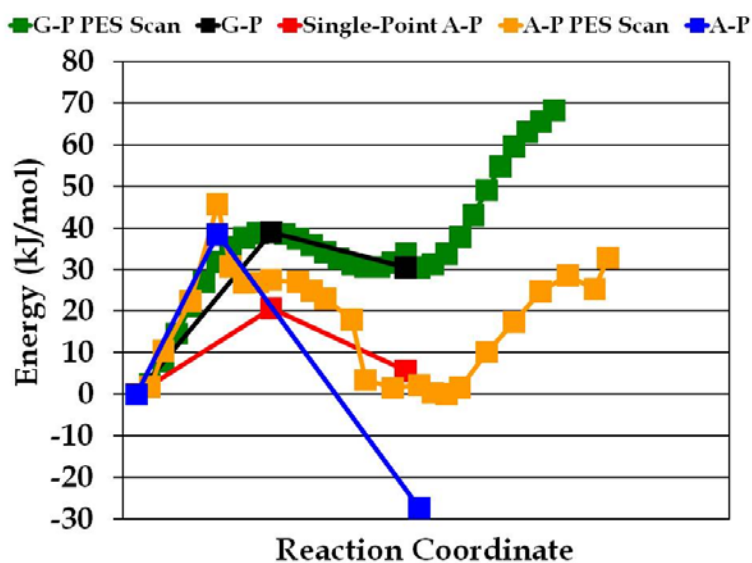


Figure 2-7: The energy plot for the deprotonated Mg–O–Si site reaction where the labeling and color scheme are the same as **Figure 2-5**.

TS from the PES scan is 7 kJ/mol higher in energy than the energy-minimized gas-phase. In the PES scan of the $\text{H}_2\text{O}-\text{Mg}^{2+}$ distance, the incoming H_2O molecule approaches the Mg^{2+} , and this causes the axial OH group to rearrange in order to allow the H_2O to approach. This scan in the aqueous-phase showed decreasing the $\text{Mg}^{2+}-\text{H}_2\text{O}$ distance to less than 3.40 Å caused an increase in energy of over 70 kJ/mol, indicating that the penta-coordinated Mg^{2+} with the H_2O molecule in the second hydration sphere is more stable, and a more detailed discussion of the presence of this penta-coordinated Mg^{2+} in the PC will be given in the next section.

The energy profiles for the hydrolysis of deprotonated sites are shown in **Figure 2-7** for the gas-phase, single-point aqueous-phase, and energy-minimized aqueous-phase calculations. The initial Mg–O distance is 2.01 Å, and the bond lengthens along the reaction coordinate until breakage in the TS where the Mg–O distance is 2.98 Å. In the

Table 2-1: Barrier heights (kJ/mol) for hydrolysis of protonated, neutral, and deprotonated sites for calculations in the gas-phase, single-point aqueous-phase, and energy-minimized aqueous-phase calculations.

Phase	Protonated	Neutral	Deprotonated
Gas	21	54	39
Single-Point Aqueous	33	40	21
Energy-Minimized Aqueous	37	44	40

PC, the Mg–O distance is 3.76 Å, and the barrier heights for this reaction are 39 kJ/mol in the gas-phase, 21 kJ/mol in the single-point aqueous-phase, and 40 kJ/mol in the energy-minimized aqueous-phase.

2.3.1.3 Reaction Mechanisms

In this section, the reaction mechanisms for the hydrolysis of Mg–O–Si sites in protonated, neutral, and deprotonated states are discussed. The reaction mechanisms show that each site releases Mg^{2+} to solution through the breaking of the Mg–O bond, and the Mg^{2+} is hexa-coordinated in the PCs for the protonated and neutral sites but penta-coordinated for the deprotonated site. Depictions of the reaction mechanisms for the hydrolysis of protonated, neutral, and deprotonated sites in the gas-phase appear in **Figures 2-8, 2-9, and 2-10**, respectively, and the Mg–O and Si–O distances as well as the Mg–O–Si angles for the RCs and TSs for each reaction in the gas-phase are given in **Table 2-2**.

The reaction mechanism for the hydrolysis of protonated Mg–O–Si sites appears in **Figure 2-8**. In the RC shown in **Figure 2-8**, the Mg^{2+} is bonded to five H_2O molecules and the O, which in this case is protonated. The protonation of O in conjunction with the

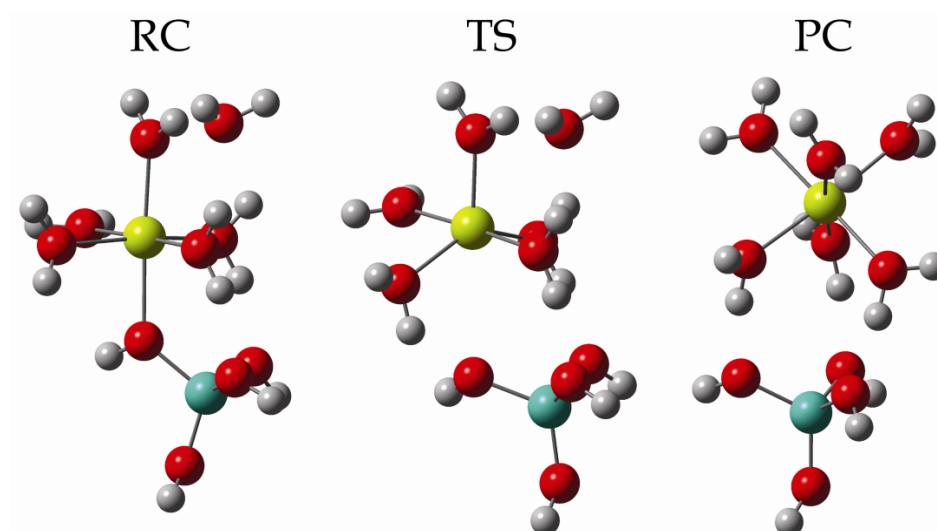


Figure 2-8: The reaction mechanism for the hydrolysis of a protonated Mg–O–Si site. The reactant complex (RC), the transition state (TS), and the product complex (PC) are shown, and the color scheme is the same as **Figure 2-1**.

use of H₂O as the Mg–O bond leads to breakage in the TS and leaves Mg²⁺ penta-coordinated. The TS shows attraction of an equatorial H₂O molecule to the O as well as rearrangement of two equatorial H₂O molecules on the Mg²⁺ to accommodate the incoming H₂O molecule. The PC is comprised of a hexaaqua Mg²⁺ ion, showing the incoming H₂O molecule has been absorbed by the Mg²⁺, and silicic acid, and three H₂O molecules on the Mg²⁺ participate in H-bonding with three OH groups on the silicic acid in the PC. This reaction mechanism agrees with previous calculations that showed that Mg²⁺ is released from the surface in the form of Mg(H₂O)₆²⁺ and that the O remains protonated and bonded to the Si atom.⁴⁶

The hydrolysis of neutral Mg–O–Si sites is represented by the reaction of a H₂O molecule with a cluster similar to that pictured in **Figure 2-8** but without the protonation of the O, and the mechanism for this reaction appears in **Figure 2-9**. In the RC, the incoming H₂O molecule is attracted to the axial H₂O molecule and an equatorial H₂O

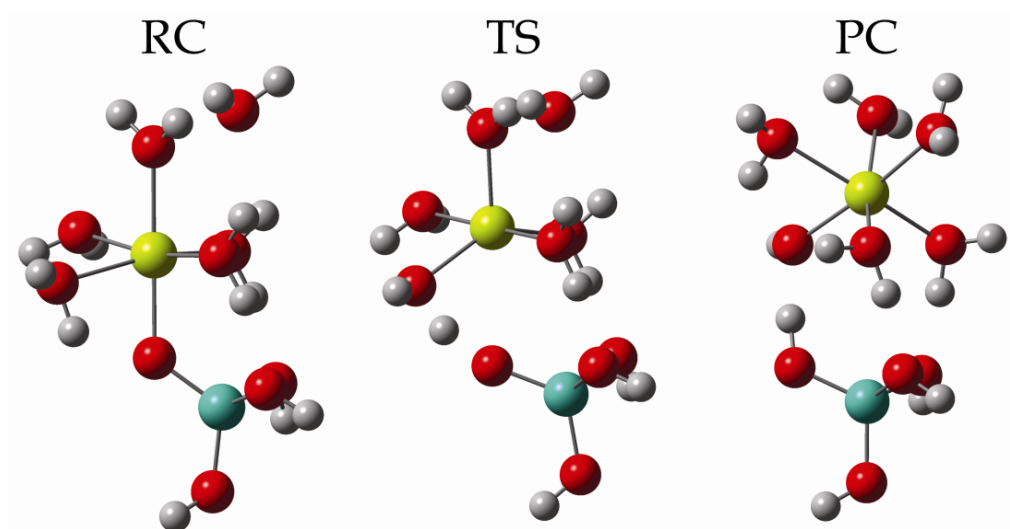


Figure 2-9: The reaction mechanism for the hydrolysis of neutral Mg–O–Si sites. The color scheme is the same as **Figure 2-1**, and the labeling is the same as **Figure 2-8**.

molecule bonded to the Mg^{2+} . The negative frequency in the TS corresponds to a concerted motion where the Mg–O bond is broken at the same time that an H^+ from an equatorial H_2O molecule is transferred to the O which now remains on the Si species. Also in the TS, breaking of the Mg–O bond in the TS leads to a decrease in Mg^{2+} coordination as with the protonated state. In the PC, the incoming H_2O molecule has been absorbed by the Mg^{2+} and also occurred in the protonated site reaction. Hence, the PC is comprised of a hexa-coordinated Mg^{2+} , in the form of $[\text{Mg}(\text{H}_2\text{O})_5\text{OH}]^+$, and silicic acid. The two H_2O molecules and the OH group on the Mg^{2+} are engaged in H-bonding with three OH groups on the Si atom.

Lastly, the deprotonated site hydrolysis reaction is depicted in **Figure 2-10**. The same Mg–O–Si molecular cluster from the neutral site reaction is reacted with OH^- in this case, and this is meant to simulate the existence of a deprotonated site on the surface. At the start of the reaction, an H^+ is transferred from the axial H_2O group on the Mg^{2+} to the incoming OH^- . Thus, in effect, a H_2O molecule reacts with the Mg–O–Si cluster

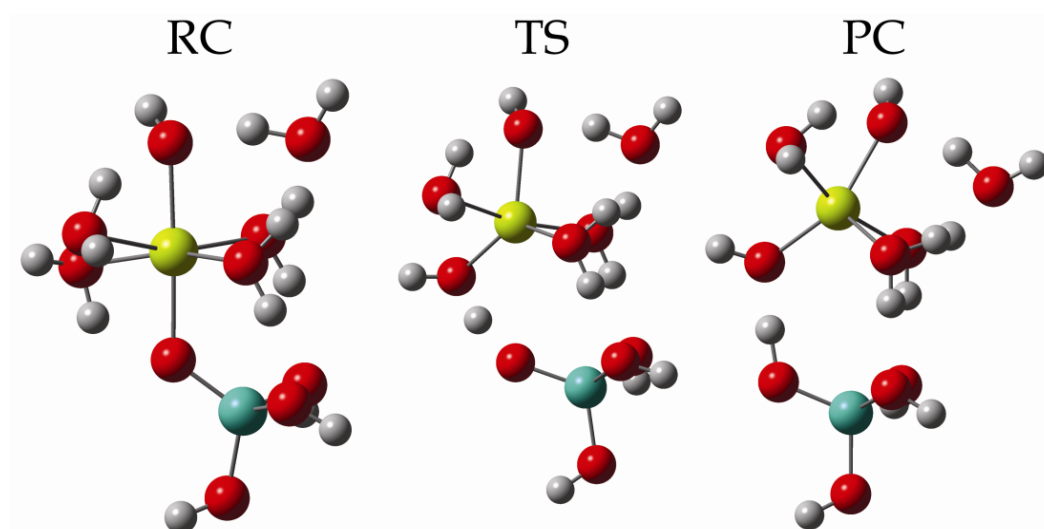


Figure 2-10: The reaction mechanism for the hydrolysis of deprotonated Mg-O-Si sites. The color scheme is the same as **Figure 2-1**, and the labeling is the same as **Figure 2-8**.

which now has an axial OH group, and these species are pictured as the RC in **Figure 2-10**. This reaction of a H₂O molecule with the deprotonated site due to a H⁺ abstraction has been postulated for quartz as well.³ In the TS, the Mg–O bond break leaves the Mg²⁺ penta-coordinated. Also in the TS, an equatorial H₂O molecule is attracted to the O whose valence is no longer complete, and this causes an H⁺ to be transferred to the O. The incoming H₂O molecule is not, however, bonded to the Mg²⁺ as seen in the previous two reactions, and the distance between the Mg²⁺ and the incoming H₂O molecule is approximately 1.0 Å greater than those in the first hydration sphere. Thus, the PC is comprised of silicic acid, a H₂O molecule, and [Mg(H₂O)₃(OH)₂].

The PC for this reaction warrants additional comment. In the gas-phase, a penta-coordinated PC is expected because the number of negatively charged groups attached to Mg²⁺ causes a decrease in its coordination number,^{47,48} and this PC is logical because the two OH groups can donate excess electrons to the Mg²⁺ within a small volume.⁴⁹ For completeness, a hexa-coordinated version of the PC was optimized in both the gas- and

aqueous-phases, and this hexa-coordinated structure was higher in energy than the penta-coordinated form with the incoming H₂O molecule in the second hydration sphere by more than 20 kJ/mol in each phase. Furthermore, aqueous Mg²⁺ species can also exist in lower coordinated states⁴⁸⁻⁵⁰ which depend upon the nature of the bonding groups.⁴⁷⁻⁴⁹ The possibility of producing either Si(OH)₄ or SiO(OH)₃⁻, representing the hydroxylated and deprotonated surface, respectively, as products will be discussed below.

The transfer of the H⁺ to the O in the gas-phase deprotonated site reaction is anomalous because the pK_a values of aqueous Mg²⁺ species are higher than those for Si^{51,52} which would indicate that H⁺ transfer is unlikely for these systems, and therefore, SiO(OH)₃⁻ rather than Si(OH)₄ would be the expected Si species in the products at high pH. In the gas-phase PES scan for the deprotonated site, the proton transfer occurs alongside of the Mg–O bond break; that is, as the Mg–O distance increases, the H–O distance decreases. The final bond length of the H⁺ transferred to the O residing on the Si species is 1.05 Å.

This anomaly prompted the use of aqueous-phase PES scans with small steps in the Mg–O distance to isolate the point in the scan at which the proton transfer occurred. In fact, for the PES scans in the aqueous-phase, the opposite is true. In both the neutral and deprotonated site reactions, the H⁺ remains on the original O atom, albeit with elongated bonds of 1.04 and 1.03 Å in the neutral and deprotonated site reactions, respectively. Thus, the results described here in the aqueous-phase show that the Si species in the PC is SiO(OH)₃⁻ and is the immediate product from the hydrolysis reaction.

The Mg–O and Si–O distances as well as the Mg–O–Si bond angles for RCs and TSs in the gas-phase for all reactions are given in **Table 2-2**. The Mg–O and Si–O distances for the RC in the protonated site reaction reflect that the O is protonated as exhibited by the longer bond for this protonation state. The Mg–O distance in the transition states is longest for the protonated state, followed by the deprotonated and neutral states. The Mg–O distance in the deprotonated state TS is longer than in the neutral site as a result of donated electron density from the axial OH group on the Mg^{2+} . This additional electron density throughout the cluster stabilizes the Mg–O distance in the TS and allows the distance to be larger than in the neutral state TS. Also in the TS, the Si–O distances for the neutral and deprotonated state reactions are shorter than that for the protonated state because the proton has not yet fully attached to the O, and thus excess electron density surrounds the O in the Si–O bond.

Lastly, the Mg–O–Si angles are similar for each protonation state in the RCs in that they differ by only 4%. This shows that the protonation of O does not have an effect on this angle, but the fact that this angle is over 120° represents compensation for steric crowding within this cluster. In addition, the beginning of a tetrahedral geometry around the O becomes evident in each of the transition states as the angles are $110^\circ - 112^\circ$.

2.3.1.4 Gibbs Free Energy Change

In addition to the reaction mechanisms and barrier heights, the change in Gibbs free energy (ΔG) for each reaction in all three phases is presented in **Table 2-3**. The overall trend is that these reactions are spontaneous at room temperature, and this is evident particularly in the calculations for the single-point and energy-minimized

Table 2-2: Mg–O and Si–O distances (Å) and Mg–O–Si angles (°) for RCs and TSs for all reactions in the gas-phase.

Protonation State	Stationary Point	Mg–O (Å)	Si–O (Å)	Mg–O–Si Angle (°)
Protonated	RC	2.17	1.70	129
	TS	3.07	1.68	111
Neutral	RC	1.98	1.59	127
	TS	2.78	1.58	110
Deprotonated	RC	2.01	1.59	126
	TS	2.98	1.58	110

Table 2-3: The change in Gibbs free energy (ΔG) values (kJ/mol) for Mg^{2+} release from protonated, neutral, and deprotonated sites in the gas- and aqueous-phase hydrolysis reactions.

Site	Gas-Phase	Single-Point Aqueous-Phase	Energy-Minimized Aqueous-Phase
Protonated	-2	-14	-12
Neutral	38	13	-8
Deprotonated	23	-2	-29

aqueous-phase reactions. The neutral and deprotonated site reactions are not thermodynamically favorable in the gas-phase but spontaneous in the energy-minimized aqueous-phase calculations. This suggests that the ΔG from gas-phase calculations is misleading. Therefore, determination of ΔG values for geochemical reactions investigated via ab-initio methods should be performed using energy-minimized aqueous-phase calculations as opposed to those in the gas-phase.

2.3.1.5 Overall Trends and Comparison to Experiment

Each of the hydrolysis reactions for Mg–O–Si sites proceeds through a dissociative interchange (I_d) mechanism.⁵³ The I_d mechanism is manifested by the decrease in coordination of the Mg^{2+} between the RC and the TS caused by the breaking of the Mg–O bond, and the Mg^{2+} returns to hexa-coordination in the PC for both the protonated and neutral states after the incoming H_2O molecule bonds with the Mg^{2+} . Further, the decrease in coordination is expected in the TS because Mg^{2+} cannot accommodate seven bonds in its first hydration sphere.⁵⁰ Although the Mg^{2+} is penta-

coordinated in the PC for the deprotonated site reaction, another H₂O molecule is likely to be bonded with the Mg²⁺ when this reaction occurs in the presence of bulk water.⁵³

The calculated Mg–O–Si barrier heights given in **Table 2-1** can be compared with previous calculations of barrier heights for Si–O–Si site hydrolysis,^{2,24,25,54} and these values appear in **Table 2-4**. The barrier heights in the gas-phase for Mg–O–Si site hydrolysis for each protonation state are lower than those for Si–O–Si hydrolysis in the same protonation state. Therefore, the Mg–O–Si barrier heights for Mg²⁺ release presented here in conjunction with the Si–O–Si barrier heights in **Table 2-4** indicate that the Mg²⁺ species would be released from the forsterite surface first. Further, this comparison can be extended to include the barrier heights for other silicate minerals as well. The barrier heights in **Table 2-1** for Mg–O–Si site hydrolysis are also lower than those for the hydrolysis of Si–O–Al sites in the same protonation state as well as for Al–O–Si sites in the pH range at which each site would exist.⁴ When these Al-bearing sites are in turn compared with the values in **Table 2-4** for Si–O–Si site hydrolysis, the Si–O–Si sites have the highest barrier heights. When one considers this particular group – Mg²⁺, Al³⁺, and Si⁴⁺ – the strength of the M–O bond increases as one moves to higher atomic number across the row in the periodic table when the octets of Mg²⁺ and Al³⁺ are expanded. This trend correlates with the observation that dissolution rates in the same pH range decrease for Mg²⁺ to Al³⁺ to Si⁴⁺ silicate minerals.²¹

Several previous experimental descriptions of forsterite dissolution have included measurements of the activation energy (E_a). However, these are actually “apparent activation energies (E_{app}).”⁵⁵⁻⁵⁸ The dissolution of forsterite includes the leaching of both Mg²⁺ and Si from the surface and from sites in all protonation states as well as the

Table 2-4: Ab-initio barrier heights (kJ/mol) for Si–O–Si site hydrolysis in the gas phase.^{2,24,25,54}

Source	Method	Protonation State		
		Protonated	Neutral	Deprotonated
Xiao and Lasaga 1994	HF/6-31G(d), MP2/6-31G(d)	100, 92	121, 134	
Xiao and Lasaga 1996	MP2/6-31G(d)			79
Pelmenschikov <i>et al.</i>	B3LYP/6-31G(d), B3LYP/6-311G(d,p)		105	
Nangia and Garrison	B3LYP/6-31+G(d,p), B3LYP/MG3S	69, 75	159, 174	110, 122

transport of H_3O^+ , H_2O , and OH^- species to the surface,⁵⁵ their adsorption,⁵⁶ and overall network opening. Furthermore, this E_{app} term also includes contributions from temperature-dependent processes that affect dissolution^{55,57} such as surface speciation.⁵⁷ Moreover, if the experiment has not reached steady state, this can have a profound effect on E_{app} .⁵⁸ Furthermore, the scatter in previous data depends mainly on the temperature at which the experiment was performed. The temperature is important because experimentally measured E_{app} values are extracted from the slope of the line formed when the log of the dissolution rate constant (k) is plotted versus the reciprocal of the temperature (in K). At temperatures below 327K, those processes in dissolution that have low E_a barriers dominate, and at temperatures higher than 327K, high E_a processes dominate.⁵⁹ Thus, the E_{app} that is measured in a dissolution experiment hinges upon the temperature at which the experiment was performed, and these aspects of dissolution must be considered when an E_{app} is communicated.

Previous researchers have calculated experimental E_{app} values for the dissolution of forsterite. Van Herk *et al.* performed dissolution experiments from pH = 1 to 3 over a temperature range of 313 to 343K, and they determined E_{app} values of 25 ± 2 kJ/mol using hydrochloric acid and 30 ± 2 kJ/mol using sulfuric acid.⁶⁰ Awad *et al.* also investigated the acidic dissolution of forsterite, specifically at pH = 1 to 2 and over the temperature range 296 to 363K. They determined the E_{app} for the dissolution of the bulk crystal to be 72 ± 12 kJ/mol.²⁰ The difference between these two values has been attributed to the inherent physical nature of the forsterite samples used.²⁰ In addition, the discrepancies between the results presented in this work shown in **Table 2-1** and these experimental values reflect the fact that these values represent different processes.

Moreover, the protonated Mg–O–Si site barrier heights are lower than nearly all of the values calculated by Van Herk *et al.* and Awad *et al.*, and this represents the fact that breaking the Mg–O bond is not the rate-limiting step.

However, there are experimental data that support the hypothesis that forsterite dissolution is controlled by Si–O–Si hydrolysis rather than Mg–O–Si hydrolysis. Pokrovsky and Schott performed dissolution experiments at $\text{pH} \leq 12$ and observed the formation of a Si-rich, Mg^{2+} -depleted layer on their forsterite samples at $\text{pH} < 9$,²³ and they postulated that the layer was comprised of polymerized silica tetrahedra.⁸ Forsterite dissolution in acidic solution was investigated via ^{29}Si MAS NMR by Davis and coworkers using a gem quality sample with no known impurities,⁶¹ and their primary finding was that Mg^{2+} was released from the surface first, leaving behind a Si-rich layer. The forsterite was dissolved at an initial pH of 3, and as Mg^{2+} ions were replaced by two H^+ ions at each site, the pH increased accordingly. This led to the development of a silica-type layer on the surface that was depleted of Mg^{2+} . The ^{29}Si MAS NMR spectra from these experiments showed the development of polymerized Si species in the form of Q^3 Si–O–Si units, or Si atoms connected through O atoms to three other Si atoms, which increased in concentration over time. The original forsterite sample was comprised of Q^0 Si units – that is, those without Si–O–Si units – which after dissolution give way to a Si-rich layer whose structure was composed of Si–O–Si bonds. Therefore, this recent experimental description of forsterite dissolution shows that Mg^{2+} release from the surface leads to the development of a Si-rich layer which is comprised of Q^3 sites and is in contrast to the original forsterite mineral structure that is characterized by Q^0 silicon sites.

2.3.2 Mg²⁺ Release Rates from Mg–O–Si Sites versus pH

2.3.2.1 Parameters for Calculating the Rate

The pre-exponential factors and rate constants for the hydrolysis reactions at protonated, neutral, and deprotonated sites in the gas-, single-point aqueous-, and energy-minimized aqueous-phases are given in **Table 2-5**, and the rate constants follow the same trend as the barrier heights outlined above. The rates for the release of Mg²⁺ from forsterite were calculated using the model from **Equation 2-10** and appear in **Table 2-6**. The data in **Table 2-6** are calculated for pH = 3.0 to 11.2, and rates for gas-, single-point aqueous-, and energy-minimized aqueous-phases are grouped in that order. The calculated rates for Mg²⁺ release given in **Table 2-6** decrease with increasing pH in the gas-phase and energy-minimized aqueous-phase calculations, and the trend in the single-point aqueous-phase calculations is anomalous due to the barrier heights from these calculations. Although the rate constants inserted into **Equation 2-14** were calculated in this work, the ρ and θ_i values were extracted from experimental data. Twenty-three OH groups appear on 1 nm² of the forsterite (100) surface which corresponds to a reactive site density of 3.82×10^{-5} mol m⁻². The θ_{prot} and θ_{deprot} values were taken from Pokrovsky and Schott,²³ and the θ_{neut} values were calculated according to **Equation 2-12**. The elementary rate constants, k_i , provided in **Table 2-5**, for the gas-, single-point aqueous-, and energy-minimized aqueous-phase reactions, were combined with the same

Table 2-5: Pre-exponential factors A (s^{-1}) and rate constants k (s^{-1}) for the hydrolysis of Mg–O–Si sites on the forsterite surface.

Site	Gas-Phase		Single-Point Aqueous-Phase		Energy-Minimized Aqueous-Phase	
	A	k	A	k	A	k
Protonated	2.4×10^{12}	5.7×10^8	2.4×10^{12}	4.3×10^6	6.3×10^{12}	1.7×10^6
Neutral	7.7×10^{11}	2.7×10^4	7.7×10^{11}	6.1×10^5	2.4×10^{12}	3.0×10^4
Deprotonated	7.1×10^{11}	2.2×10^6	7.1×10^{11}	6.0×10^8	9.7×10^{12}	9.9×10^5

Table 2-6: Reaction rates ($\text{mol m}^{-2}\text{s}^{-1}$) for the hydrolysis of protonated, neutral, and deprotonated sites in gas-, single-point aqueous-, and energy-minimized aqueous-phases.

Gas-Phase								
pH	ρ (mol m^{-2})	θ_{prot}	Protonated (s^{-1})	θ_{neut}	Neutral (s^{-1})	θ_{deprot}	Deprotonated (s^{-1})	Total Rate ($\text{mol m}^{-2} \text{s}^{-1}$)
3.0	3.82×10^{-5}	1.8×10^{-5}	5.7×10^8	2.0×10^{-5}	2.7×10^4	0.0×10^0	2.2×10^6	3.90×10^{-1}
3.5	3.82×10^{-5}	1.6×10^{-5}	5.7×10^8	2.3×10^{-5}	2.7×10^4	0.0×10^0	2.2×10^6	3.38×10^{-1}
4.7	3.82×10^{-5}	1.3×10^{-5}	5.7×10^8	2.6×10^{-5}	2.7×10^4	0.0×10^0	2.2×10^6	2.73×10^{-1}
5.6	3.82×10^{-5}	8.6×10^{-6}	5.7×10^8	3.0×10^{-5}	2.7×10^4	0.0×10^0	2.2×10^6	1.87×10^{-1}
6.2	3.82×10^{-5}	8.1×10^{-6}	5.7×10^8	3.0×10^{-5}	2.7×10^4	0.0×10^0	2.2×10^6	1.77×10^{-1}
6.6	3.82×10^{-5}	4.3×10^{-6}	5.7×10^8	3.4×10^{-5}	2.7×10^4	0.0×10^0	2.2×10^6	9.36×10^{-2}
7.3	3.82×10^{-5}	2.9×10^{-6}	5.7×10^8	3.5×10^{-5}	2.7×10^4	0.0×10^0	2.2×10^6	6.24×10^{-2}
8.0	3.82×10^{-5}	1.7×10^{-6}	5.7×10^8	3.7×10^{-5}	2.7×10^4	0.0×10^0	2.2×10^6	3.64×10^{-2}
8.5	3.82×10^{-5}	1.4×10^{-6}	5.7×10^8	3.7×10^{-5}	2.7×10^4	0.0×10^0	2.2×10^6	3.12×10^{-2}
9.6	3.82×10^{-5}	0.0×10^0	5.7×10^8	3.7×10^{-5}	2.7×10^4	9.6×10^{-7}	2.2×10^6	1.19×10^{-4}
10.2	3.82×10^{-5}	0.0×10^0	5.7×10^8	3.6×10^{-5}	2.7×10^4	2.6×10^{-6}	2.2×10^6	2.58×10^{-4}
10.6	3.82×10^{-5}	0.0×10^0	5.7×10^8	3.5×10^{-5}	2.7×10^4	3.1×10^{-6}	2.2×10^6	2.97×10^{-4}
11.2	3.82×10^{-5}	0.0×10^0	5.7×10^8	3.5×10^{-5}	2.7×10^4	3.6×10^{-6}	2.2×10^6	3.37×10^{-4}
Single-Point Aqueous-Phase								
pH	ρ (mol m^{-2})	θ_{prot}	Protonated (s^{-1})	θ_{neut}	Neutral (s^{-1})	θ_{deprot}	Deprotonated (s^{-1})	Total Rate ($\text{mol m}^{-2} \text{s}^{-1}$)
3.0	3.82×10^{-5}	1.8×10^{-5}	4.3×10^6	2.0×10^{-5}	6.1×10^5	0.0×10^0	6.0×10^8	3.42×10^{-3}
3.5	3.82×10^{-5}	1.6×10^{-5}	4.3×10^6	2.3×10^{-5}	6.1×10^5	0.0×10^0	6.0×10^8	3.08×10^{-3}
4.7	3.82×10^{-5}	1.3×10^{-5}	4.3×10^6	2.6×10^{-5}	6.1×10^5	0.0×10^0	6.0×10^8	2.66×10^{-3}
5.6	3.82×10^{-5}	8.6×10^{-6}	4.3×10^6	3.0×10^{-5}	6.1×10^5	0.0×10^0	6.0×10^8	2.11×10^{-3}
6.2	3.82×10^{-5}	8.1×10^{-6}	4.3×10^6	3.0×10^{-5}	6.1×10^5	0.0×10^0	6.0×10^8	2.04×10^{-3}
6.6	3.82×10^{-5}	4.3×10^{-6}	4.3×10^6	3.4×10^{-5}	6.1×10^5	0.0×10^0	6.0×10^8	1.50×10^{-3}
7.3	3.82×10^{-5}	2.9×10^{-6}	4.3×10^6	3.5×10^{-5}	6.1×10^5	0.0×10^0	6.0×10^8	1.30×10^{-3}
8.0	3.82×10^{-5}	1.7×10^{-6}	4.3×10^6	3.7×10^{-5}	6.1×10^5	0.0×10^0	6.0×10^8	1.13×10^{-3}
8.5	3.82×10^{-5}	1.4×10^{-6}	4.3×10^6	3.7×10^{-5}	6.1×10^5	0.0×10^0	6.0×10^8	1.10×10^{-3}

9.6	3.82×10^{-5}	0.0×10^0	4.3×10^6	3.7×10^{-5}	6.1×10^5	9.6×10^{-7}	6.0×10^8	2.28×10^{-2}
10.2	3.82×10^{-5}	0.0×10^0	4.3×10^6	3.6×10^{-5}	6.1×10^5	2.6×10^{-6}	6.0×10^8	6.10×10^{-2}
10.6	3.82×10^{-5}	0.0×10^0	4.3×10^6	3.5×10^{-5}	6.1×10^5	3.1×10^{-6}	6.0×10^8	7.20×10^{-2}
11.2	3.82×10^{-5}	0.0×10^0	4.3×10^6	3.5×10^{-5}	6.1×10^5	3.6×10^{-6}	6.0×10^8	8.29×10^{-2}
Energy-Minimized Aqueous-Phase								
pH	ρ (mol m ⁻²)	θ_{prot}	Protonated (s ⁻¹)	θ_{neut}	Neutral (s ⁻¹)	θ_{deprot}	Deprotonated (s ⁻¹)	Total Rate (mol m ⁻² s ⁻¹)
3.0	3.82×10^{-5}	1.8×10^{-5}	1.7×10^6	2.0×10^{-5}	3.0×10^4	0.0×10^0	9.9×10^5	1.18×10^{-3}
3.5	3.82×10^{-5}	1.6×10^{-5}	1.7×10^6	2.3×10^{-5}	3.0×10^4	0.0×10^0	9.9×10^5	1.03×10^{-3}
4.7	3.82×10^{-5}	1.3×10^{-5}	1.7×10^6	2.6×10^{-5}	3.0×10^4	0.0×10^0	9.9×10^5	8.43×10^{-4}
5.6	3.82×10^{-5}	8.6×10^{-6}	1.7×10^6	3.0×10^{-5}	3.0×10^4	0.0×10^0	9.9×10^5	5.92×10^{-4}
6.2	3.82×10^{-5}	8.1×10^{-6}	1.7×10^6	3.0×10^{-5}	3.0×10^4	0.0×10^0	9.9×10^5	5.61×10^{-4}
6.6	3.82×10^{-5}	4.3×10^{-6}	1.7×10^6	3.4×10^{-5}	3.0×10^4	0.0×10^0	9.9×10^5	3.18×10^{-4}
7.3	3.82×10^{-5}	2.9×10^{-6}	1.7×10^6	3.5×10^{-5}	3.0×10^4	0.0×10^0	9.9×10^5	2.27×10^{-4}
8.0	3.82×10^{-5}	1.7×10^{-6}	1.7×10^6	3.7×10^{-5}	3.0×10^4	0.0×10^0	9.9×10^5	1.51×10^{-4}
8.5	3.82×10^{-5}	1.4×10^{-6}	1.7×10^6	3.7×10^{-5}	3.0×10^4	0.0×10^0	9.9×10^5	1.35×10^{-4}
9.6	3.82×10^{-5}	0.0×10^0	1.7×10^6	3.7×10^{-5}	3.0×10^4	9.6×10^{-7}	9.9×10^5	7.90×10^{-5}
10.2	3.82×10^{-5}	0.0×10^0	1.7×10^6	3.6×10^{-5}	3.0×10^4	2.6×10^{-6}	9.9×10^5	1.40×10^{-4}
10.6	3.82×10^{-5}	0.0×10^0	1.7×10^6	3.5×10^{-5}	3.0×10^4	3.1×10^{-6}	9.9×10^5	1.58×10^{-4}
11.2	3.82×10^{-5}	0.0×10^0	1.7×10^6	3.5×10^{-5}	3.0×10^4	3.6×10^{-6}	9.9×10^5	1.75×10^{-4}

ρ and θ_i values in **Equation 2-10** to yield the Mg^{2+} release rate in units of $\text{mol m}^{-2} \text{s}^{-1}$ as given in the last column of **Table 2-6**.

2.3.2.2 Rates versus pH

In both the gas-phase and energy-minimized aqueous-phase calculations, the rate decreases as pH increases over the range of pH from 3.0 – 11.2. The Mg^{2+} release rate from the single-point aqueous-phase calculations shows a somewhat U-shaped behavior, which is a result of the anomaly in barrier heights described in Section 2.3.1.2. The need for energy-minimized aqueous-phase calculations for these systems is reinforced here with the anomalous behavior of the single-point aqueous-phase calculations.

2.3.2.3 Comparisons with Previous Work

The approach used here for the rate equation describing the release of species as a function of the types of sites on a surface has been used for quartz, and the calculated rates derived from ab-initio barrier heights replicated the findings of previous quartz dissolution experiments.² However, several different parameters are included here that were not present in the previous work. The number of OH groups available for reaction on a forsterite surface has not been measured experimentally, so an estimate was made based on the database included in the Cerius² software.³⁰ Additionally, the experimental data of Pokrovsky and Schott²³ were used to describe the fraction of protonated, neutral, and deprotonated sites on the surface as opposed to detailed descriptions of protonation

state fractions on the quartz surface.² The subsequent extrapolation of the number of neutral and deprotonated sites in acidic pH and the number of protonated and neutral sites in basic pH is thus a blend of experimental data and data fitting in this model.

In addition to differences in the methodology of the quartz dissolution rate analysis² versus this work, the dissolution chemistry is different between these two minerals. For quartz, overall dissolution occurs as a result of the network opening, site protonation, Si release from Si–O–Si sites, and the net release of material that results from excess dissolution versus precipitation. For forsterite, comparable processes occur for both Mg–O–Si and Si–O–Si sites, which form after the leaching of Mg²⁺ from the surface. Therefore, the discrepancies that exist for the dissolution rates stem from the fact that the Mg²⁺ leaching process is not rate-limiting in the pH ranges studied here, but the replication of experimental trends shows that the model is appropriate for describing Mg²⁺ release.

Stoichiometric dissolution is seen for forsterite dissolution in acidic^{10,11,23} and basic pH⁸ despite the slower release rate of Si to solution and occurs when the surface species are released to solution such that a ratio of their rates is equal to their ratio in the parent mineral.²¹ The presence of stoichiometric dissolution in forsterite experiments is intriguing in that Mg²⁺ release results from a lower energy process – that is, the breaking of the Mg–O bond – versus the same process for the release of Si to solution. However, stoichiometric dissolution for this mineral is explained by the sequential release of Mg²⁺ then Si from the forsterite surface. Once the Mg²⁺ is depleted in the surface layer, Si atoms are released from the polymerized layer that develops.⁶¹ Dissolution experiments performed on acid-reacted forsterite samples showed that Si was released preferentially,²³

indicative of the need to dissolve away this Si-rich layer before additional Mg^{2+} can be released.

2.4 Conclusions

The mechanisms and rate of Mg^{2+} release from forsterite have been successfully modeled by integrating experimental data and ab-initio results. The reaction mechanisms and barrier heights of the hydrolysis of Mg–O–Si sites were investigated, and the hydrolysis of the protonated, neutral, and deprotonated states proceeds through a two-step mechanism where the breaking of the Mg–O bond corresponds to the step which releases Mg^{2+} to solution. The barrier heights for the energy-minimized gas-phase and aqueous-phase calculations show that the protonated sites are the lowest, followed by the deprotonated and neutral sites in turn. Furthermore, any aqueous-phase calculations performed to represent geochemical processes must be optimized as the single-point aqueous-phase calculations do not always yield reliable results.

The barrier heights for the release of Mg^{2+} from Mg–O–Si sites were used to calculate rate constants and in turn a rate for this process. The rate constants and rates are higher than experimental rates for overall dissolution,⁵⁻¹¹ as indicated by the lower calculated barrier heights compared to E_{app} values for the dissolution for forsterite;^{20,60} thus, the release of Mg^{2+} is not the rate-limiting step. However, these ab-initio results corroborate previous experimental and ab-initio results; ^{29}Si MAS NMR experiments of forsterite dissolution show the Mg^{2+} is released before Si and that a Si-rich layer develops on the surface.⁶¹ In conjunction with previous ab-initio calculations for the hydrolysis of

Si–O–Si sites,^{2,24,25,54} the ab-initio results here also show that Mg^{2+} leaches first from the forsterite surface.

Initially, two possibilities existed for the reaction coordinate of these reactions, but the decrease in the distance between the H_2O molecule in the second hydration sphere and the Mg^{2+} in the Mg–O–Si cluster did not lead to a breaking of the Mg–O bond. Instead, PES scans indicate that the distance between the H_2O molecule and the Mg^{2+} led only to an exchange of H_2O molecules around the Mg^{2+} when it was hexa-coordinated, whereas the Mg–O bond remained intact. Therefore, the release of Mg^{2+} from the surface as a result of breaking the Mg–O bond is a direct result of the lengthening of the Mg–O bond and not the exchange of H_2O molecules around the Mg^{2+} .

2.5 References

- (1) Brantley, S. L. Reaction kinetics of primary rock-forming minerals under ambient conditions: fresh water geochemistry, weathering, and soils. In *Treatise on Geochemistry*; Turekian, K. K., Holland, H. D., Eds.; Pergamon Press: Oxford, 2003; Vol. 5; pp 73.
- (2) Nangia, S.; Garrison, B. J. *J. Phys. Chem. A* **2008**, *112*, 2027.
- (3) Bickmore, B. R.; Wheeler, J. C.; Bates, B.; Nagy, K. L.; Eggett, D. L. *Geochim. Cosmochim. Ac.* **2008**, *72*, 4521.
- (4) Morrow, C. P.; Nangia, S.; Garrison, B. J. *J. Phys. Chem. A* **2009**, *113*, 1343.
- (5) Grandstaff, D. E. The dissolution rate of forsteritic olivine from Hawaiian beach sand. In *Rates of Chemical Weathering of Rocks and Minerals*; Colman, S. M., Dethier, D. P., Eds.; Academic Press, Inc.: New York, 1986; pp 49.
- (6) Wogelius, R. A.; Walther, J. V. *Geochim. Cosmochim. Ac.* **1991**, *55*, 943.
- (7) Wogelius, R. A.; Walther, J. V. *Chem. Geol.* **1992**, *97*, 101.
- (8) Pokrovsky, O. S.; Schott, J. *Geochim. Cosmochim. Ac.* **2000**, *64*, 3313.
- (9) Rosso, J. J.; Rimstidt, J. D. *Geochim. Cosmochim. Ac.* **2000**, *64*, 797.
- (10) Oelkers, E. H. *Chem. Geol.* **2001**, *175*, 485.
- (11) Olsen, A. A.; Rimstidt, J. D. *Geochim. Cosmochim. Ac.* **2008**, *72*, 1758.
- (12) <http://chemxseer.ist.psu.edu>; compiled by Amanda A. Olsen.
- (13) Giammar, D. E.; Bruant, R. G.; Peters, C. A. *Chem. Geol.* **2005**, *217*, 257.
- (14) Hanchen, M.; Prigiobbe, V.; Storti, G.; Seward, T. M.; Mazzotti, M. *Geochim. Cosmochim. Ac.* **2006**, *70*, 4403.
- (15) Matter, J. M.; Takahashi, T.; Goldberg, D. *Geochem. Geophys. Geosy.* **2007**, *8*, Q02001.
- (16) Oelkers, E. H.; Gislason, S. R.; Matter, J. *Elements* **2008**, *4*, 333.
- (17) Van Essendelft, D. T.; Schobert, H. H. *Ind. Eng. Chem. Res.* **2009**, *48*, 2556.
- (18) IPCC *Special Report on Carbon Capture and Storage*; Cambridge University Press: Cambridge, 2005.
- (19) Birle, J. D.; Gibbs, G. V.; Moore, P. B.; Smith, J. V. *Am. Mineral.* **1968**, *53*, 807.
- (20) Awad, A.; van Groos, A. F. K.; Guggenheim, S. *Geochim. Cosmochim. Ac.* **2000**, *64*, 1765.
- (21) Brantley, S. L. Kinetics of mineral dissolution. In *Kinetics of Water-Rock Interaction*; Brantley, S. L., Kubicki, J. D., White, A. F., Eds.; Springer: New York, NY, 2008; pp 151.
- (22) Blum, A.; Lasaga, A. *Nature* **1988**, *331*, 431.
- (23) Pokrovsky, O. S.; Schott, J. *Geochim. Cosmochim. Ac.* **2000**, *64*, 3299.
- (24) Xiao, Y.; Lasaga, A. C. *Geochim. Cosmochim. Ac.* **1994**, *58*, 5379.
- (25) Xiao, Y.; Lasaga, A. C. *Geochim. Cosmochim. Ac.* **1996**, *60*, 2283.
- (26) Criscenti, L. J.; Brantley, S. L.; Mueller, K. T.; Tsomaia, N.; Kubicki, J. D. *Geochim. Cosmochim. Ac.* **2005**, *69*, 2205.
- (27) Ottonello, G.; Zuccolini, M. V. *Geochim. Cosmochim. Ac.* **2005**, *69*, 851.
- (28) Wander, M. C. F.; Kubicki, J. D.; Clark, A. E.; Schoonen, M. A. A. *J. Phys. Chem. A* **2009**, *113*, 1020.
- (29) Kubicki, J. D. *J. Phys. Chem. A* **2001**, *105*, 8756.

- (30) Cerius²; Accelrys: San Diego, CA.
- (31) Vosko, S. H.; Wilk, L.; Nusair, M. *Can. J. Phys.* **1980**, *58*, 1200.
- (32) Lee, C.; Yang, W.; Parr, R. G. *Phys. Rev. B* **1988**, *37*, 785.
- (33) Becke, A. D. *J. Chem. Phys.* **1993**, *98*, 1372.
- (34) Becke, A. D. *J. Chem. Phys.* **1993**, *98*, 5648.
- (35) Sousa, S. F.; Fernandes, P. A.; Ramos, M. J. *J. Phys. Chem. A* **2007**, *111*, 10439.
- (36) Dudev, T.; Lim, C. *J. Phys. Chem. A* **1999**, *103*, 8093.
- (37) Frisch, M. J.; Trucks, G. W.; Schlegel, H. B.; Scuseria, G. E.; Robb, M. A.; Cheeseman, J. R.; Montgomery, J. A., Jr.; Vreven, T.; Kudin, K. N.; Burant, J. C.; Millam, J. M.; Iyengar, S. S.; Tomasi, J.; Barone, V.; Mennucci, B.; Cossi, M.; Scalmani, G.; Rega, N.; Petersson, G. A.; Nakatsuji, H.; Hada, M.; Ehara, M.; Toyota, K.; Fukuda, R.; Hasegawa, J.; Ishida, M.; Nakajima, T.; Honda, Y.; Kitao, O.; Nakai, H.; Klene, M.; Li, X.; Knox, J. E.; Hratchian, H. P.; Cross, J. B.; Bakken, V.; Adamo, C.; Jaramillo, J.; Gomperts, R.; Stratmann, R. E.; Yazyev, O.; Austin, A. J.; Cammi, R.; Pomelli, C.; Ochterski, J. W.; Ayala, P. Y.; Morokuma, K.; Voth, G. A.; Salvador, P.; Dannenberg, J. J.; Zakrzewski, V. G.; Dapprich, S.; Daniels, A. D.; Strain, M. C.; Farkas, O.; Malick, D. K.; Rabuck, A. D.; Raghavachari, K.; Foresman, J. B.; Ortiz, J. V.; Cui, Q.; Baboul, A. G.; Clifford, S.; Cioslowski, J.; Stefanov, B. B.; Liu, G.; Liashenko, A.; Piskorz, P.; Komaromi, I.; Martin, R. L.; Fox, D. J.; Keith, T.; Al-Laham, M. A.; Peng, C. Y.; Nanayakkara, A.; Challacombe, M.; Gill, P. M. W.; Johnson, B.; Chen, W.; Wong, M. W.; Gonzalez, C.; Pople, J. A. Gaussian03, Revision E.01; Gaussian, Inc.: Wallingford, CT, 2004.
- (38) Dennington, R., II; Keith, T.; Millam, J. GaussView, Version 4.1; Semichem, Inc.: Shawnee Mission, KS, 2007.
- (39) Cancès, E.; Mennucci, B.; Tomasi, J. *J. Chem. Phys.* **1997**, *107*, 3032.
- (40) Ochterski, J. W. *Thermochemistry in Gaussian*; Gaussian, Inc., 2000.
- (41) Keith, T. A.; Frisch, M. J. Inclusion of explicit solvent molecules in a self-consistent-reaction field model of solvation. In *Modeling the H Bond*; Smith, D. A., Ed.; ACS Symposium Series: Washington, D. C., 1994; Vol. 569.
- (42) Foresman, J. B.; Frisch, A. *Exploring Chemistry with Electronic Structure Methods*, 2nd ed.; Gaussian, Inc.: Pittsburgh, 1996.
- (43) TheRate. The CSE-Online Project: University of Utah, 2006.
- (44) Duncan, W. T.; Bell, R. L.; Truong, T. N. *J. Comp. Chem.* **1998**, *19*, 1039.
- (45) Casey, W. H. *J. Colloid Interf. Sci.* **1991**, *146*, 586.
- (46) Liu, Y.; Olsen, A. A.; Rimstidt, J. D. *Am. Mineral.* **2006**, *91*, 455.
- (47) Brown, I. D. *Acta Crystallogr. B* **1988**, *44*, 545.
- (48) Kluge, S.; Weston, J. *Biochemistry-US* **2005**, *44*, 4877.
- (49) Markies, P. R.; Akkerman, O. S.; Bickelhaupt, F.; Smeets, W. J. J.; Spek, A. L. *Adv. Organomet. Chem.* **1991**, *32*, 147.
- (50) Bock, C. W.; Kaufman, A.; Glusker, J. P. *Inorg. Chem.* **1994**, *33*, 419.
- (51) Burgess, J. *Ions in solution: Basic principles of chemical interactions*; Ellis Horwood Limited: Chichester, 1988.
- (52) Dissociation Constants of Inorganic Acids and Bases. In *CRC Handbook of Chemistry and Physics*; 88th ed.; Lide, D. R., Ed.; CRC Press/Taylor and Francis: Boca Raton, FL, 2008.

- (53) Casey, W. H.; Swaddle, T. W. *Rev. Geophys.* **2003**, *41*, 1008.
- (54) Pelmeshnikov, A.; Leszczynski, J.; Pettersson, L. G. M. *J. Phys. Chem. A* **2001**, *105*, 9528.
- (55) Wieland, E.; Wehrli, B.; Stumm, W. *Geochim. Cosmochim. Ac.* **1988**, *52*, 1969.
- (56) Lasaga, A. C. Fundamental approaches in describing mineral dissolution and precipitation rates. In *Chemical Weathering Rates of Silicate Minerals*; Brantley, S. L., White, A. F., Eds.; Mineralogical Society of America: Washington, D. C., 1995; Vol. 31; pp 27.
- (57) Brady, P. V.; House, W. A. Surface-controlled dissolution and growth of minerals. In *Physics and Chemistry of Minerals Surfaces*; Brady, P. W., Ed.; CRC Press: New York, 1996.
- (58) Cama, J.; Ayora, C.; Lasaga, A. C. *Geochim. Cosmochim. Ac.* **1999**, *63*, 2481.
- (59) Lasaga, A. C. *Kinetic Theory of the Earth Sciences* Princeton University Press: Princeton, 1998.
- (60) Van Herk, J.; Pietersen, H. S.; Schuiling, R. D. *Chem. Geol.* **1989**, *76*, 341.
- (61) Davis, M. C.; Brouwer, W. J.; Wesolowski, D. J.; Anovitz, L. M.; Lipton, A. S.; Mueller, K. T. *Phys. Chem. Chem. Phys.* **2009**, *11*, 7013.

Chapter 3

Quantum Mechanical Modeling of Hydrolysis and H₂O-Exchange in Mg-, Ca-, and Ni-Silicate Clusters: Implications for Dissolution Mechanisms of Olivine Minerals

Reproduced with permission from:

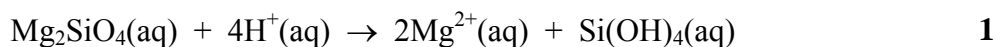
Morrow, C. P.; Olsen, A. A.; Kubicki, J. D. *Journal of Physical Chemistry C*, submitted for publication. Unpublished work copyright 2010 American Chemical Society.

3.1 Introduction

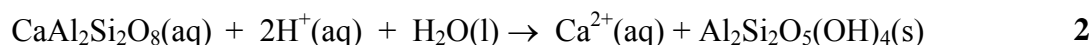
The work described in Chapter 3 employs quantum mechanical calculations to investigate the proposed correlation between H₂O exchange rates around aqueous metal ions and the dissolution rates of silicate minerals containing those ions. The H₂O exchange reaction for a hydrated Mg²⁺ ion is modeled in order to determine whether gas-phase or aqueous-phase approximations are more appropriate to model these systems. The conditions that cause each M–O bond to break, namely H₂O approach of M–O bond lengthening, are identified. The barrier heights for H₂O exchange and hydrolysis reactions for each protonated M–O–Si (M = Ni²⁺, Mg²⁺, Ca²⁺) site are calculated and used to calculate the rate constant for each of these reactions. For all of the reactions studied, a comparison with experimental observations is made.

Dissolution occurs via reaction of species from solution with sites on the mineral surface, leading ultimately to the breakdown of the original mineral structure and resulting in the release of elemental constituents to solution, as in **Reactions 3-1** and **3-2**.

Depending upon whether the mineral is forsterite or anorthite, dissolution of the mineral in acidic media would proceed as **(3-1)**:^{2,5}



for forsterite or **(3-2)**:



for anorthite. This process is comprised of many reactions, including the opening of the surface structure network, the replacement of the O atoms in the metal surface polyhedra with H₂O molecules,¹⁰ and surface site hydrolysis. This last class of reactions occurs when a H₃O⁺ ion, H₂O molecule, or OH⁻ ion from solution reacts with a metal site on the surface to release a metal ion to solution, which results from the breaking of the M–O bond.

The H₂O molecules, H₃O⁺ ions, and OH⁻ ions from solution affect the dissolution rate through two possible mechanisms. The effect of the H₃O⁺ ion on the dissolution rate has been described as proton-promoted dissolution,^{11,12} where the dissolution rate of a mineral is observed to increase as a function of decreasing pH. This is likely because H⁺ ions adsorb to surface O atoms and weaken the M–O and Si–O bonds. The second proposed mechanism is known as ligand-promoted dissolution.¹¹⁻¹³ The H₂O molecule and OH⁻ ion serve as ligands bonding to the mineral surface, and their effect on the dissolution rate likely results from the weakening of the M–O surface bonds via an increase in charge to the metal that is delivered by the adsorbing ligand.¹¹ At a given pH, there is a distribution of H⁺, H₂O, and OH⁻ species from solution reacting with surface

sites, and thus the proton- and ligand-promoted pathways can both be active during dissolution.¹²

While ligand-promoted dissolution occurs as a result of the exchange of ligands from solution for H₂O molecules or OH[−] groups on the surface,¹³ a ligand exchange reaction occurs when a group on an aqueous metal species is replaced by another from solution, and this reaction proceeds as (3-3):



where *M* is an aqueous metal ion, *X* is a ligand coordinated with *M*, and *Y* is a ligand from solution, according to the notation of Langford and Gray.¹⁴ One type of ligand exchange reaction is H₂O exchange around metal ions in solution.¹⁵ Such reactions can also occur on a mineral surface, and in the case of silicate minerals, this process involves the breaking and forming of M–O bonds at surface sites. Rates of H₂O exchange reactions around a metal cation in solution correlate with the amount of energy required to break the M–O bond^{15,16} as well as with the dissolution rates of orthosilicate minerals.^{15,17-19} This trend arises because both H₂O exchange reactions and the release of cations from silicate minerals involve the breaking of M–O bonds – in the form of M–O, M–OH, or M–OH₂, and this correlation extends across nearly seven orders of magnitude in orthosilicate dissolution rates.¹⁷ Because both processes involve breaking of M–O bonds, the reaction mechanisms for these two processes have been hypothesized to be fundamentally similar,^{13,17} and previous researchers have suggested that this similarity enables a direct comparison between rates for ligand-promoted dissolution and H₂O exchange reactions in solution.¹³ However, the amount of energy required to break a M–

O bond decreases across the following series: $M-O > M-OH > M-OH_2$. Therefore, the rates of such reactions are not equal, and the correlation of dissolution rates of orthosilicate minerals with H_2O exchange rates may not mean that the mechanisms are the same.

Both H_2O exchange reactions and ligand-promoted dissolution reactions in the form of hydrolysis of $M-O$ bonds occur at surface sites during dissolution of silicate minerals. What remains to be seen is if these two phenomena are related and if the H_2O exchange rate of an aqueous metal ion is an indicator of how dissolution proceeds for a mineral containing that cation. There is no known chemical explanation¹⁵ for the correlation of H_2O exchange reaction rates and the dissolution rates of orthosilicate minerals.^{15,17-19} H_2O molecules are thought to replace O atoms in mineral polyhedra during dissolution in acidic pH.¹⁰ Although extensive experimental data exist,^{10,15,17,20,21} molecular mechanisms of these surface reactions have yet to be described for divalent silicate minerals using quantum mechanical techniques. The link between H_2O exchange reactions in solution and the dissolution of divalent silicate minerals has not been investigated from a molecular perspective. Our hypothesis is that the release of metals to solution occurs as a result of hydrolysis of $M-O$ linkages in the mineral network. One aim of this work is to test the hypothesis that H_2O exchange reactions on the surface lead to $M-O$ bond hydrolysis.

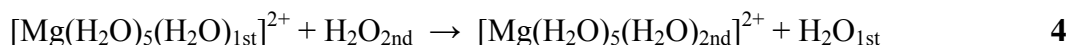
One approach for investigating the link between H_2O exchange reactions and the dissolution rates of minerals is to use quantum mechanical calculations, which enable a molecular scale investigation into reaction mechanisms. Previous work has studied the hydrolysis of sites on the surface for quartz,²² aluminosilicates,²³⁻²⁵ and forsterite.²⁶

These studies analyzed experimental phenomena by using molecular clusters to simulate sites on the mineral surface, and experimental observations were replicated.^{22,25,26} What is most important about this approach is that the most fundamental aspect of a chemical phenomenon is investigated without the interference of atoms that do not participate in the reaction.²³ Therefore, a molecular cluster investigation would allow for the analysis of H₂O exchange and hydrolysis reactions on the surface, enable a description of the reaction mechanisms, and provide insight into the link between H₂O exchange reaction rates for metals in solution and the dissolution rates for minerals containing these metals.

Questions that have yet to be answered include whether H₂O exchange reactions are coupled with dissolution, how H₂O exchange reactions affect dissolution, and if the metal cations studied are released from the mineral surface with similar mechanisms. The results from the quantum mechanical calculations employed in this work seek to answer these questions. Molecular clusters representing protonated M–O–Si (M = Ni²⁺, Mg²⁺, and Ca²⁺) sites on a mineral surface were reacted with H₃O⁺ ions to examine H₂O exchange and hydrolysis reactions and to determine whether these processes are coupled for the end-member silicate minerals chosen. These particular ions were chosen for this study because they represent orthosilicate minerals with nearly the slowest through the fastest dissolution rates in recent experimental investigations.¹⁵⁻¹⁷ This work includes the calculation of activation energy barrier heights and rate constants for these reactions, a description of each reaction mechanism, and a comparison with experimental results.

3.2 Computational Methods

Molecular clusters are employed to model two classes of reactions in this work. The first is a H₂O exchange reaction around the hexaaqua Mg²⁺ ion, Mg(H₂O)₆²⁺, and the second models reactions with H₂O and molecular clusters representing M–O–Si sites on olivine surfaces. In the H₂O exchange reaction around the Mg(H₂O)₆²⁺ ion, Mg(H₂O)₆²⁺ reacts with a H₂O molecule to model the replacement of a H₂O molecule from the first hydration sphere by one from the second. This reaction proceeds as (3-4):



with the H₂O molecule originally in the first hydration sphere now in the second.

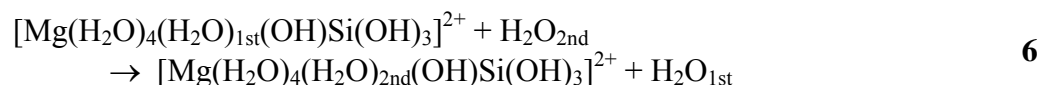
In the second class of reactions, molecular clusters are employed to represent protonated M–O–Si sites on olivine surfaces. A metal ion – where the metal is Ni, Mg, or Ca – is hexa-coordinated via five H₂O molecules and the M–O–Si linkage. The Si is bonded to three OH groups to represent the bonds to the bulk crystal. This termination via OH groups is supported by the fact that atoms farther than the next nearest neighbor position participate minimally in bond breaking at the surface.²³ These molecular clusters are each reacted with a H₂O molecule to investigate H₂O exchange and hydrolysis reactions occurring at protonated M–O–Si surface sites, where protonation is represented by a H⁺ bonded to the O in the M–O–Si linkage. The presence of both the H⁺ and the reacting H₂O molecule represent the reaction of a H₃O⁺ ion from solution with a M–O–Si site on the mineral surface.

The reactions of these protonated clusters with a H₂O molecule are given in **Reactions 3-5** through **3-9**. The protonated Ni–O–Si site is reacted with a H₂O molecule according to **(3-5)**:



forming a hexaaqua Ni²⁺ ion and silicic acid as products.

For protonated Mg–O–Si sites, two reactions are investigated. The first is a H₂O exchange reaction **(3-6)**,



where H₂O_{1st} is the H₂O molecule from the first hydration sphere that moves to the second, and H₂O_{2nd} is the H₂O molecule from the second hydration sphere that moves to the first. The second Mg–O–Si reaction studied is the hydrolysis of a protonated Mg–O–Si site **(3-7)**,

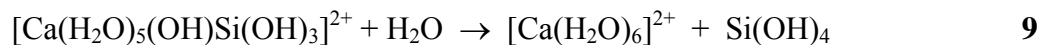


and the hexaaqua Mg²⁺ ion and silicic acid form as the products.

For protonated Ca–O–Si sites, two reactions are investigated, and the first is H₂O exchange **(3-8)**,



where instead of an exchange of H₂O molecules from the first and second hydration spheres, the absorption of the second hydration sphere H₂O molecule into the primary hydration sphere forms a hepta-coordinated Ca²⁺. The hydrolysis of a protonated Ca–O–Si site proceeds as **(3-9)**:



and the hexaaqua Ca^{2+} ion and silicic acid form in the products.

The silicic acid product, $\text{Si}(\text{OH})_4$, in **Reactions 3-5**, **3-7**, and **3-9** represents a hydroxylated Si site that remains on the surface after release of the metal to solution. The existence of charge is included in the calculations by assigning the overall system a charge of +2. Thus this charge is dispersed throughout all the atoms in the system and is not solely located on the metal ion. However, for clarity in this work as well as for ease in comparison with experimental data, the metals will each be referred to in their ionic state.

Density functional theory (DFT) calculations have been shown to describe surface site hydrolysis reactions successfully.²²⁻²⁶ In particular, the B3LYP functional is used because of its hybrid density functional nature that combines exchange-correlation,²⁷⁻³⁰ gradient correction,^{29,30} and a percentage of Hartree-Fock exchange.³¹ The 6-31G(d,p) basis set has been used to model the hydration of Mg^{2+} ³² and here is used to investigate the reactions in **Reactions 3-4** through **3-9**. The absence of diffuse functions is advantageous for decreasing the basis set superposition error (BSSE) on transition metal complexes;³³ BSSE is expected to be minimal as we report relative energy changes for molecular clusters, where the intermolecular distances do not vary dramatically.

Molecular clusters representing $\text{Mg}(\text{H}_2\text{O})_6^{2+}$ or protonated M–O–Si (M = Ni, Mg, and Ca) sites were optimized with a H_2O molecule in the second hydration sphere, and this optimized structure served as the starting reactants for potential energy surface (PES) scans of the H_2O exchange and hydrolysis reactions. For the H_2O exchange reactions, the

distance between the H₂O in the second hydration sphere and the metal was constrained and decreased by 0.1 Å for 20 steps to represent the approach of a H₂O molecule from solution. This reaction coordinate was chosen as opposed to varying the distance between the metal and the first hydration sphere H₂O molecule because the latter underestimates bound water lifetimes³⁴ and because the second hydration sphere H₂O molecule distance from the metal is considered fundamental to the H₂O exchange reaction.³⁵ If the M–O bond did not break during the H₂O exchange reaction, then a scan of the M–O distance was performed until it broke, and a second scan of the approach of the second hydration sphere H₂O molecule was performed. Each of these scans was comprised of 20 steps, where each step was 0.1 Å. These two scans represent the release of the metal ion to solution and the completion of the second hydration shell, respectively.

The structures with the lowest energy in the beginning and end of the scans were optimized as reactant complex (RC) and product complex (PC), respectively, whereas the structure with the highest energy was optimized as the transition state (TS). After optimization, the dynamic stability of each calculated RC and PC was demonstrated by an absence of negative frequencies; that is, each complex was at least in a local minimum. Possible TSs were identified by the presence of one and only one negative (imaginary) frequency. For each reaction, this negative frequency corresponded either to the forming of the M–OH₂ bond or to the breaking of the M–O bond and thus the reaction coordinate between reactants and products. The energy of each RC was set as zero, and the relative energies of the TS and PC were used to make the energy profiles. The PES

scans, geometry optimizations, and frequency calculations were performed with Gaussian 03,³⁶ and all images of the reaction mechanisms were made with GaussView 4.³⁷

The H₂O exchange reaction around the Mg(H₂O)₆²⁺ ion was also modeled using the self-consistent reaction field (SCRF) method via the integral equation formalism polarized continuum model (IEFPCM)³⁸ with water as the solvent as well as with a super-molecule approach,³⁹ where 12 H₂O molecules were included to model the second hydration sphere. The gas-phase RC, TS, and PC structures were optimized using the IEFPCM. The RC and PC were characterized by the absence of negative frequencies and the TS by a negative frequency corresponding to the formation of the Mg–OH₂ bond. In the super-molecule approach, the starting structure with 6 H₂O molecules in the first hydration sphere and 12 in the second was optimized. This structure was then used as the input for a PES scan where the distance between the Mg²⁺ and a H₂O molecule in the second hydration sphere was constrained, and this distance was decreased by 0.1 Å for 20 steps, in a similar fashion to the scans described above. The corresponding lowest energy structures at the beginning and end of the scan were optimized as the RC and PC, respectively, and the highest energy structure was optimized as the TS. As with each of the descriptions given above, the RC and PC structures were characterized by the absence of negative frequencies, while the TS was identified by the presence of one and only one negative frequency corresponding to the formation of the Mg–OH₂ bond.

Once the RC and TS had been isolated for each reaction, the frequency output files were used to calculate the rate constant according to the classical transition state theory (TST) approximation and using TheRate^{40,41} according to the Arrhenius equation (10):

$$k_T = AT^n e^{-(E_a/RT)}$$

10

where A is the pre-exponential factor, T is the temperature in K, n is the exponential of the temperature-dependence of A , E_a is the activation energy, and R is the gas constant.^{40,41} However, the n exponent was set to zero to eliminate the temperature dependence of A , and T was set to 298 K.

3.3 Results and Discussion

3.3.1 H₂O Exchange around the Hydrated Mg²⁺ Ion

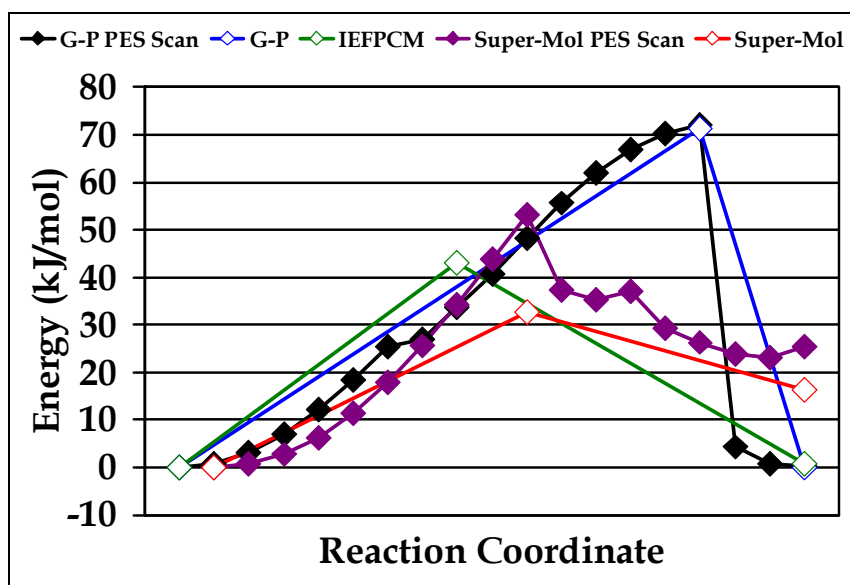
One of the goals of this work is to examine the H₂O exchange reaction around metal ions, and the H₂O exchange reaction around the Mg(H₂O)₆²⁺ ion was studied as a test of our computational approach. Similar investigations have been performed for Ni(H₂O)₆²⁺⁴²⁻⁴⁴ and Ca(H₂O)₆²⁺.⁴⁵ To date, computational investigations of hydrated Mg²⁺ ions have been restricted to the stability of structures,^{32,46-48} hydration energies,⁴⁷ binding energies,^{32,46-49} and vibrational spectra³² of H₂O molecules within the first and second hydration spheres, but no study has focused specifically on determining the barrier height or rate constant of this reaction. Here, H₂O exchange around the hexaaqua Mg²⁺ ion is described, and the reaction mechanisms, barrier heights, and rate constants are presented for this reaction in the gas-phase and the aqueous-phase, using the IEFPCM and super-molecule approximations.

The exchange of H₂O molecules around the hexaaqua Mg²⁺ ion is shown in **Figure 3-1**. The energy for each point along the PES scans and the energy profiles for

the gas-phase, IEFPCM, and super-molecule approaches are shown in **Figure 3-1a**. The reactant complex (RC), transition state (TS), and product complex (PC) structures shown in **Figure 3-1b** were optimized in the gas-phase. The H₂O molecule from the second hydration sphere is circled in blue, while the H₂O molecule in the first hydration sphere that will be replaced is circled in green (**Figure 3-1b**). In the RC, the H₂O molecule from the second hydration sphere is H-bonded to two H₂O molecules, as has been observed in previous calculations.^{32,46,48} The TS is marked by a single negative frequency corresponding to the formation of the bond between the Mg²⁺ and the H₂O molecule in the second hydration sphere. In the PC, the H₂O molecule from the second hydration sphere is bonded to the Mg²⁺ ion, and the H₂O molecule originally in the first hydration sphere has moved to the second.

The distances between the Mg²⁺ and the approaching second hydration sphere H₂O molecule as well as between the Mg²⁺ and the leaving first hydration sphere H₂O molecule are listed in **Table 3-1** for the optimized RC, TS, and PC structures in the gas-phase. In the RC, the H₂O molecule in the second hydration sphere is 3.88 Å from the Mg²⁺, and the H₂O molecule in the first hydration sphere is 2.12 Å from the Mg²⁺. As the H₂O molecule from the second hydration sphere approaches the Mg²⁺, the bond between the Mg²⁺ and the H₂O in the first hydration sphere begins to lengthen. In the TS, this bond length is 2.56 Å, while the H₂O from the second hydration sphere is 2.36 Å from the Mg²⁺. Once these two H₂O molecules have exchanged, the newly formed Mg–OH₂ bond is 2.11 Å, and the H₂O that is now in the second hydration sphere is 3.88 Å from the Mg²⁺.

(a)



(b)

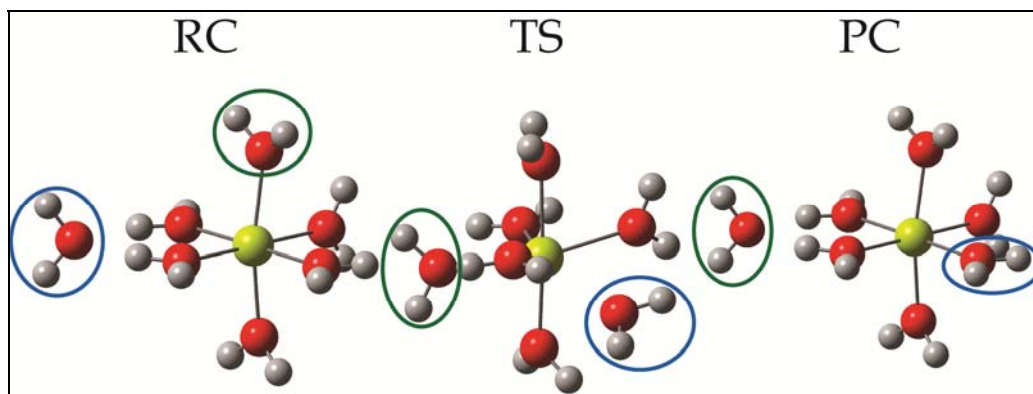


Figure 3-1: PES scan of H₂O exchange around a solvated Mg²⁺ ion. (a) The energy profile for this reaction in the gas-phase and the aqueous-phase. (b) The optimized RC, TS, and PC in the gas-phase. The magnesium ion is yellow, the oxygen atoms are red, and the hydrogen atoms are white. The H₂O molecule from the first hydration sphere that moves to the second is circled in green, while the H₂O molecule from the second hydration sphere that moves to the first is circled in blue.

Table 3-1: Relevant distances (Å), bond angles (°), barrier heights (kJ/mol), pre-exponential factors (s^{-1}), and rate constants (s^{-1}) for the H_2O exchange reaction around $Mg(H_2O)_6^{2+}$.

Optimized Gas-Phase Structure	Mg–H ₂ O _{2nd} (Å)	Mg–H ₂ O _{1st} (Å)	
RC	3.88	2.12	
TS	2.36	2.56	
PC	2.11	3.88	
H ₂ O _{2nd} –Mg–H ₂ O _{1st} Bond Angles in TS (deg)			
Gas-Phase	72, 141, 132, 73		
IEFPCM	91, 110, 92, 107		
Super-Molecule	112, 91, 87, 96		
Reaction Phase	Barrier Height (kJ/mol)	A (s^{-1})	k (s^{-1})
Gas-Phase	71	3.4×10^{13}	1.1×10^1
IEFPCM	43	5.7×10^{12}	1.6×10^5
Super-Molecule	33	8.7×10^{11}	1.7×10^6

The TSs in the gas-phase and aqueous-phase present two different molecular geometries, and they are each pictured in **Figure 3-2**. The bond angles around Mg^{2+} in the gas-phase, IEFPCM, and super-molecule approximation are given in **Table 3-1**. For the gas-phase structure, the angles start with the H_2O molecule from the second hydration sphere and proceed clockwise around the Mg^{2+} in **Figure 3-2**. For the IEFPCM and super-molecule structures, the angles are those made by the axial H_2O molecule, the Mg^{2+} ion, and each equatorial H_2O molecule. In the gas-phase, the molecular geometry is such that the entering and leaving H_2O molecules are oriented 132° from one another, and this contributes to a distorted pentagonal bipyramidal molecular geometry. Despite that this geometry is contrary to expectations,^{32,46,48,50-52} the heptaaqua Mg^{2+} ion has been optimized before.⁴⁸ For both the IEFPCM and super-molecule calculations, the reaction proceeded slightly differently than the gas-phase. Here, the TSs shown in **Figure 3-2** have square-pyramidal geometries. In the IEFPCM calculation, the H_2O molecule from the first hydration sphere H-bonded to the H_2O molecule at the apex of the pyramid,

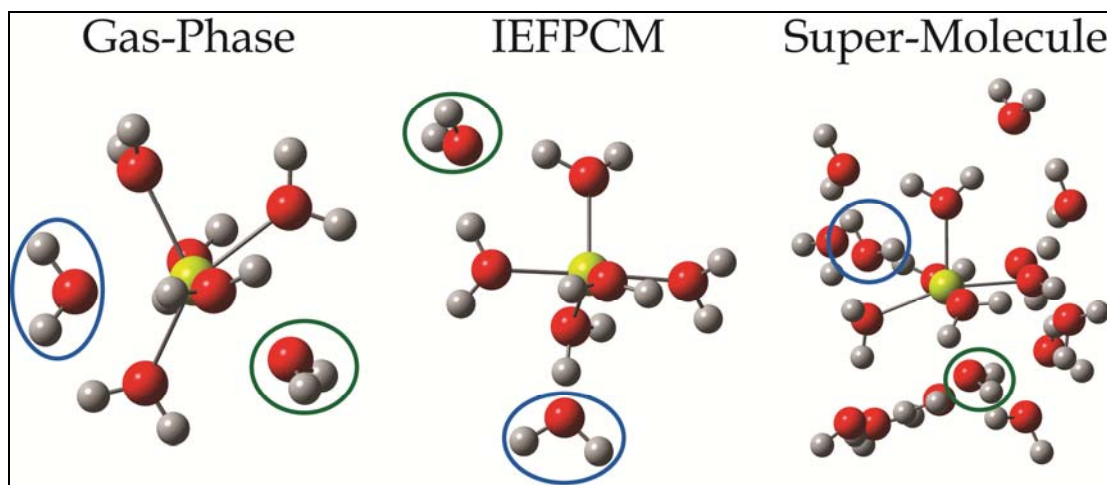


Figure 3-2: Optimized TS structures for the gas-phase, IEFPCM, and super-molecule calculations. The gas-phase TS is the same as that in **Figure 3-1** but has been rotated to show the hepta-coordinated geometry around the Mg^{2+} ion. The color scheme is the same as **Figure 3-1**.

while the H_2O molecule from the second hydration sphere approaches the Mg^{2+} along the axis opposite the apex of the pyramid. In the super-molecule calculation, the TS is also square-planar, where the incoming H_2O molecule approaches opposite the axial H_2O molecule bond to the Mg^{2+} . Due to the presence of the additional, non-reacting H_2O molecules, the first hydration sphere H_2O molecule participates in H-bonding with H_2O molecules in the second hydration sphere rather than those in the first. A square-pyramidal geometry for the TS in H_2O exchange reactions around divalent metal cations has been proposed before.^{33,43,44}

Although the molecular geometries of the TSs are different in the gas-phase and in the aqueous-phase, the H_2O exchange mechanism for $\text{Mg}(\text{H}_2\text{O})_6^{2+}$ most closely matches an associative interchange (I_a) characterization. The negative frequency in the TS corresponds to the formation of the $\text{Mg}-\text{OH}_2$ bond and is concerted throughout the H-

bonding network. In the gas-phase and super-molecule calculations, this characterization is further reinforced in that the existing Mg–OH₂ bond has not significantly lengthened, < 1.0 Å, in the TS, but this is not true in the IEFPCM calculation. The angles of the octahedron are distorted primarily in the gas-phase calculation. These findings are in contrast to previous work that suggested a seventh group could not be accommodated by Mg²⁺.^{52,53}

The PES scans and energy profiles for the Mg(H₂O)₆²⁺ exchange reaction in the three phases discussed here are shown in **Figure 3-1a**, and the barrier heights and rate constants are given in **Table 3-1**. The plot shows that the gas-phase barrier height is ~30–40 kJ/mol higher than for the IEFPCM and super-molecule calculations, respectively. The barrier heights are 71, 43, and 33 kJ/mol for the gas-phase, IEFPCM, and super-molecule calculations, respectively. The rate constants are calculated according to **Equation 3-10** and are 1.1 x 10¹, 1.6 x 10⁵, and 1.7 x 10⁶ s⁻¹, respectively.

The large difference in the gas-phase and aqueous-phase barrier heights likely stems from the hepta-coordinated geometry of the gas-phase TS, and thus the hexa-coordinated geometry of the TSs in the IEFPCM and super-molecule geometries stabilize the reaction. The geometry in the IEFPCM and super-molecule approximation likely results from steric constraints that result from the reaction cavity in the IEFPCM and the additional non-reacting H₂O molecules in the super-molecule approach; both of which lower the barrier height. The barrier height of this reaction from the IEFPCM calculation is closest to the experimental values given in **Table 3-2**, but the super-molecule value is comparable within computational uncertainty. This shows that a molecular cluster

Table 3-2: Reaction enthalpies (ΔH_x^\ddagger , in kJ/mol) and barrier heights (ΔE_x^\ddagger , in kJ/mol) for H₂O exchange around Ni(H₂O)₆²⁺, Mg(H₂O)₆²⁺, and Ca(H₂O)₆²⁺ in the gas-phase from previous studies^{42,43,45,54-56} and from this work for Mg(H₂O)₆²⁺ in the gas-phase and aqueous-phase.

Experimental (ΔH_x^\ddagger , kJ/mol)	Calculated (ΔE_x^\ddagger , kJ/mol)	Reference
Ni ²⁺		
56.9		Bechtold, <i>et al.</i> , 1978
	42.9	Rotzinger, 1996
	46.9	Rotzinger, 1996
	87.4–154.0	Kang, <i>et al.</i> , 1991
Mg ²⁺		
43		Neely and Connick, 1970
49.1±0.7		Bleuzen, <i>et al.</i> , 1997
	71	This work, gas-phase
	43	This work, IEFPCM
	33	This work, super-molecule
Ca ²⁺		
	28.0, 30.5, 31.4	Tsutsui, <i>et al.</i> , 1997

approach to modeling reactions around hydrated metal ions is appropriate for these systems.

The barrier heights for the exchange of H₂O molecules around Mg(H₂O)₆²⁺ calculated in this work can be compared to the previous experimental and theoretical values given in **Table 3-2**.^{42,43,45,54-56} The rates of H₂O exchange around Ni(H₂O)₆²⁺, Mg(H₂O)₆²⁺, and Ca(H₂O)₆²⁺ are known to follow the series Ni(H₂O)₆²⁺ < Mg(H₂O)₆²⁺ < Ca(H₂O)₆²⁺,⁵⁷ and therefore, one would expect the barrier heights to follow the same trend. Using this logic and the barrier heights in **Table 3-2**, the barrier heights for H₂O exchange around Mg(H₂O)₆²⁺ follow the expected trend within computational uncertainty. In addition, the experimentally measured rate constant for this reaction is 6.7 x 10⁵ s⁻¹,⁵⁷ and the aqueous-phase rate constants calculated in this work and given in **Table 3-1** are within an order of magnitude of this value.

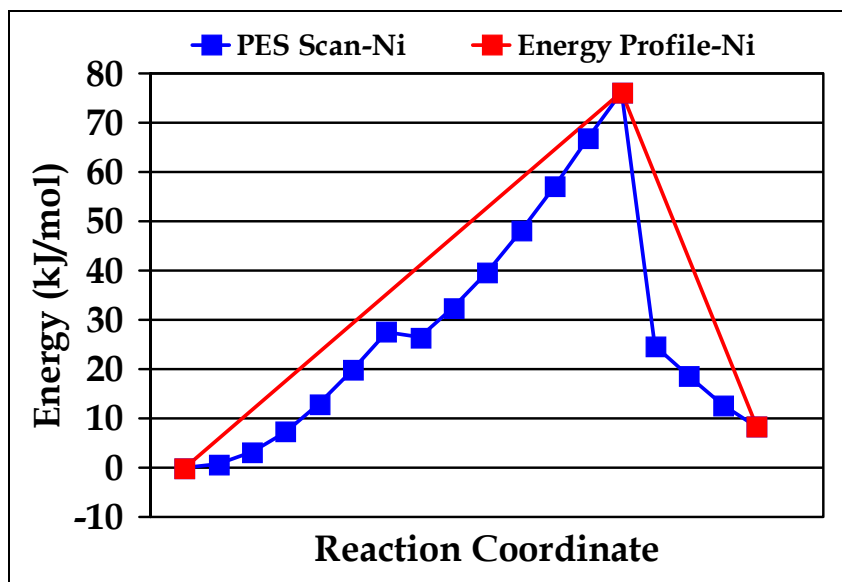
3.3.2 Reaction Mechanisms and Energy Profiles for H₂O Exchange and Hydrolysis

The PES scans present the energy that each point along the scan has as compared to the energy of the RC, which is set as zero, and the energy profiles represent the energy of the optimized TS and PC species relative to the RC. The scans are presented in **Figures 3-3a–7a** along with the energy profiles of the optimized RC, TS, and PC, whose structures appear in **Figures 3-3b–7b** and depict the reaction mechanisms of the five reactions studied. The relevant bond lengths of the optimized RC, TS, and PC as well as the bond angles of the TS for each reaction are given in **Table 3-3**, and the barrier heights of all the reactions appear in **Table 3-4**.

3.3.2.1 Protonated Ni–O–Si Sites

The PES scan where the distance between the Ni²⁺ and the H₂O molecule from the second hydration sphere was constrained and served as the reaction coordinate as well as the energy profile appear in **Figure 3-3a**. The reaction mechanism comprised of the optimized RC, TS, and PC structures is depicted in **Figure 3-3b** and shows the concerted H₂O exchange and Ni–O bond break. In the RC, the second hydration sphere H₂O molecule is H-bonded to the H⁺ on O as well as to an equatorial H₂O molecule. As this second hydration sphere H₂O molecule approaches Ni²⁺, the equatorial H₂O molecules begin to rearrange to accommodate the second hydration sphere H₂O molecule, as shown in the TS. The negative frequency corresponds to the formation of the Ni–OH₂ bond. As a result, the approach of the H₂O leads to the breaking of the Ni–O bond, and this is

(a)



(b)

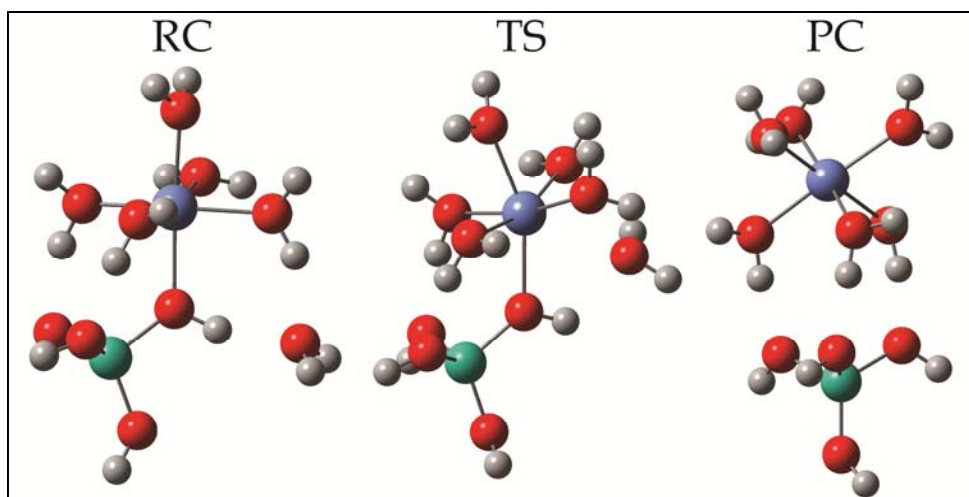


Figure 3-3: (a) The potential energy surface (PES) scan (blue line with blue squares) and optimized energy profile (red line with red squares) for hydrolysis of a protonated Ni–O–Si site where energy (kJ/mol) is plotted versus reaction coordinate. (b) The reaction mechanism for this reaction where the reactant complex (RC), transition state (TS), and product complex (PC) are presented. The nickel ion is blue, the silicon atom is turquoise, the oxygen atoms are red, and the hydrogen atoms are white. *The PES scan, geometry optimizations, and frequency calculations were performed by Dr. Amanda A. Olsen during her post-doctoral work at Penn State.*

Table 3-3: Relevant distances (Å) and bond angles (°) in the reactions for protonated Ni–O–Si, Mg–O–Si, and Ca–O–Si sites.

Reaction Type	Optimized Structure	Forming Bond (Å)	Breaking Bond (Å)
Ni–O–Si			
H ₂ O Exchange/ Hydrolysis		Ni–H ₂ O	Ni–O
	RC	3.81	2.10
	TS	2.51	2.14
	PC	2.11	4.02
		Bond Angles (deg)	
	TS	O–Ni–H ₂ O _{eq}	109, 109, 83, 83
	TS	H ₂ O _{ax} –Ni–H ₂ O _{eq}	82, 87, 86, 78
Mg–O–Si			
H ₂ O Exchange		Mg–H ₂ O _{2nd}	Mg–H ₂ O _{1st}
	RC	3.85	2.10
	TS	2.20	2.26
	PC	2.10	3.84
		Bond Angles (deg)	
	TS	O–Mg–H ₂ O _{eq}	106, 107, 82, 80
	TS	H ₂ O _{ax} –Mg–H ₂ O _{eq}	77, 83, 89, 85
Hydrolysis		Mg–H ₂ O	Mg–O
	RC	3.85	2.14
	TS	4.28	3.74
	PC	2.09	4.11
		Bond Angles (deg)	
	TS	O–Mg–H ₂ O _{eq}	70, 105, 72, 70
	TS	H ₂ O _{ax} –Mg–H ₂ O _{eq}	112, 91, 109, 93
Ca–O–Si			
Hepta-coordinated Ca ²⁺		Ca–H ₂ O	Ca–O
	RC	4.09	2.46
	TS	2.99	2.45
	PC	2.51	2.52
		Bond Angles (deg)	
	TS	O–Ca–H ₂ O _{eq}	122, 100, 75, 77
	TS	H ₂ O _{ax} –Ca–H ₂ O _{eq}	84, 93, 84, 77
Hydrolysis		Ca–H ₂ O	Ca–O
	RC	4.09	2.46
	TS	2.44	3.04
	PC	2.39	4.34
		Bond Angles (deg)	
	TS	O–Ca–H ₂ O _{eq}	83, 92, 79, 87
	TS	H ₂ O _{ax} –Ca–H ₂ O _{eq}	124, 93, 75, 92

Table 3-4: Barrier heights (kJ/mol) for H₂O exchange and hydrolysis of protonated Ni–O–Si, Mg–O–Si, and Ca–O–Si sites.

Reaction Type	Barrier Height (kJ/mol)
Ni–O–Si	
H ₂ O Exchange/Hydrolysis	76
Mg–O–Si	
H ₂ O Exchange	69
Hydrolysis	54
Ca–O–Si	
Hepta-Coordinated Ca ²⁺	24
Hydrolysis	27

evident in the PC by the hexaaqua Ni²⁺ ion and the absence of the Ni–O bond, leaving silicic acid as the second product. The barrier height for this reaction is 76 kJ/mol.

The distances between the Ni²⁺ and the approaching second hydration sphere H₂O molecule and the Ni²⁺ and O are listed in **Table 3-3** for the optimized RC, TS, and PC. In the RC, the Ni–H₂O distance is 3.81 Å, and the Ni–O distance is 2.10 Å. For the TS, the Ni–H₂O distance has decreased to 2.51 Å, while the Ni–O distance has increased to 2.14 Å. The final Ni–H₂O and Ni–O distances in the PC are 2.11 Å and 4.02 Å, respectively.

The bond angles surrounding Ni²⁺ in the TS are also included in **Table 3-3**. The bond angles surrounding the Ni²⁺ in the TS are listed starting from the equatorial H₂O molecule in the right foreground of **Figure 3-3b** and continue counter-clockwise. The O–Ni–H₂O_{eq} angles are 109°, 109°, 83°, and 83°, while the H₂O_{ax}–Ni–H₂O_{eq} bond angles are 82°, 87°, 86°, and 78°. The O–Ni–H₂O_{eq} angles closest to the approaching second hydration sphere H₂O molecule are increased from the expected 90° for an octahedral

complex, and this demonstrates that these groups are indeed rearranging as a result of the additional H₂O molecule.

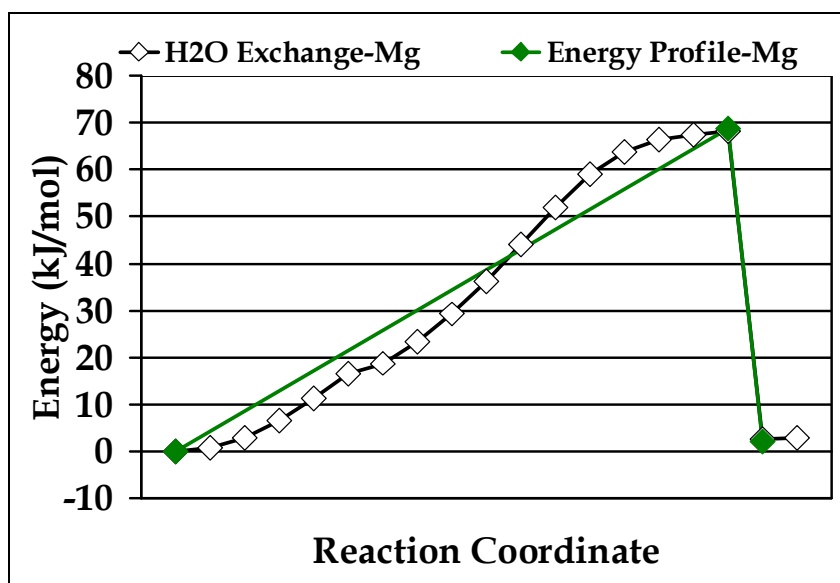
The approach of a second hydration sphere H₂O molecule toward a protonated Ni–O–Si site leads to release of Ni²⁺, in the form of Ni(H₂O)₆²⁺, to solution. The PES scan and mechanism for this reaction indicate that H₂O exchange leads to Ni–O bond break. Thus for protonated Ni–O–Si sites, the H₂O exchange and hydrolysis reactions are one and the same.

3.3.2.2 Protonated Mg–O–Si Sites

3.3.2.2.1 H₂O Exchange

The H₂O exchange reaction for a protonated Mg–O–Si site is shown in **Figure 3-4**. A PES scan of the constrained distance between the Mg²⁺ and the H₂O molecule from the second hydration sphere as the reaction coordinate and the energy profile of the optimized RC, TS, and PC appear in **Figure 3-4a**. The structures of the optimized RC, TS, and PC are shown in **Figure 3-4b**. As the incoming H₂O approaches the Mg²⁺, the equatorial H₂O molecules begin to rearrange to enable the exchange. The TS is characterized by elongated bonds to the first hydration shell H₂O molecules and to O. Also in the TS, the H₂O_{1st} (green circle) begins to leave the first hydration shell, whereas the H₂O_{2nd} (blue circle) enters the first hydration shell. For this reaction, the negative frequency corresponds to a concerted interaction of the approaching H₂O molecule with the H-bonding network of the equatorial H₂O molecules. In the PC, the Mg–O bond is

(a)



(b)

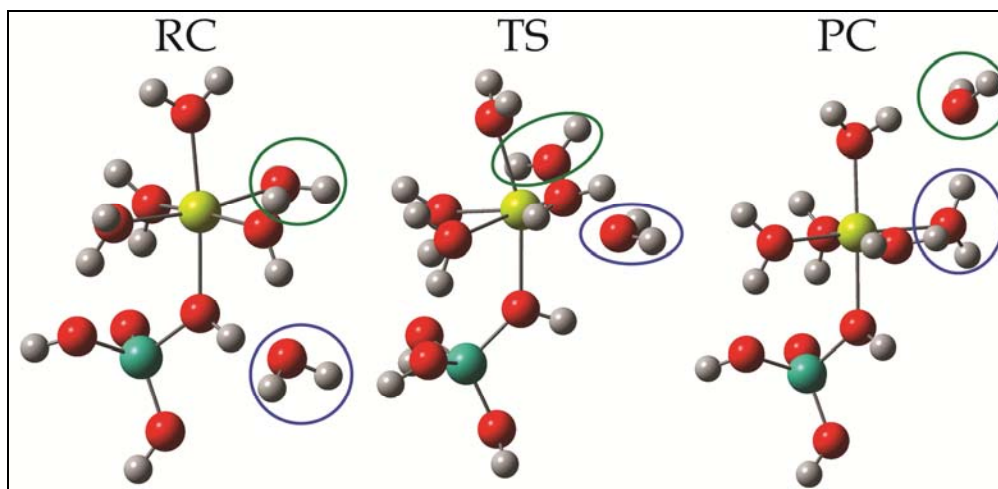


Figure 3-4: (a) The PES scan (black line with open diamonds) and optimized energy profile (green line with closed diamonds) for H₂O exchange around Mg in a protonated Mg–O–Si site where energy (kJ/mol) is plotted versus reaction coordinate. (b) The reaction mechanism for this reaction where the RC, TS, and PC are presented. The magnesium ion is yellow, the silicon atom is turquoise, the oxygen atoms are red, and the hydrogen atoms are white.

intact, and the H₂O_{1st} has been replaced by the H₂O_{2nd} as shown in **Figure 3-4b**. The barrier height for this reaction is 69 kJ/mol.

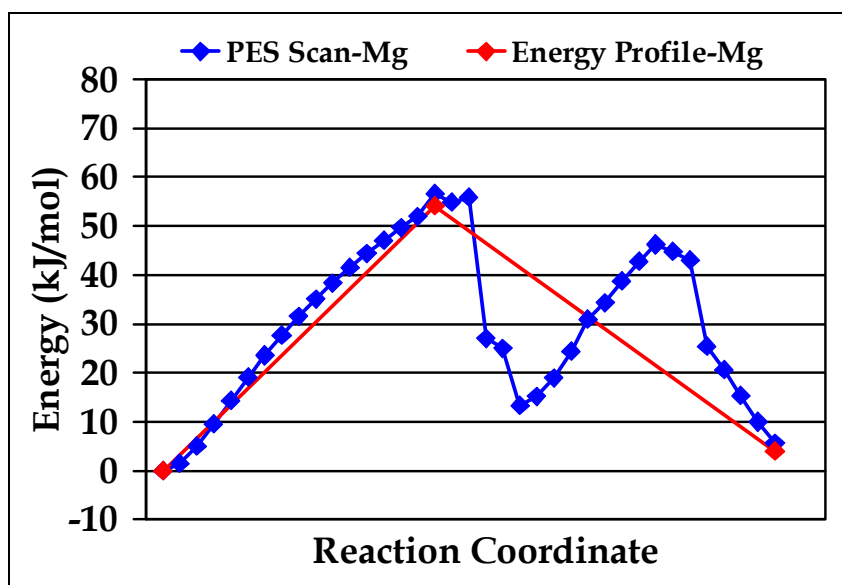
The distances between the Mg²⁺ and the H₂O_{2nd} as well as the Mg²⁺ and H₂O_{1st} are listed in **Table 3-3** for the optimized RC, TS, and PC in the H₂O exchange reaction for the protonated Mg–O–Si site. In the RC, the Mg–H₂O_{2nd} distance is 3.85 Å, and the Mg–H₂O_{1st} distance is 2.10 Å. In the TS, the Mg–H₂O_{2nd} distance is 2.20 Å, shorter than the Mg–H₂O_{1st} distance of 2.26 Å. The final Mg–H₂O_{2nd} distance is 2.10 Å, and the final Mg–H₂O_{1st} distance is 3.84 Å.

The bond angles around Mg²⁺ in the TS are also included in **Table 3-3**. The bond angles surrounding the Mg²⁺ in the TS are listed using either O or the axial H₂O as anchors and starting from the equatorial H₂O molecule in the right foreground of **Figure 3-4b** and continue counter-clockwise. The O–Mg–H₂O_{eq} bond angles are 106°, 107°, 82°, and 80°, while the H₂O_{ax}–Mg–H₂O_{eq} angles are 77°, 83°, 89°, and 85°. The O–Mg–H₂O_{eq} bond angles show that the equatorial H₂O molecules are opening up to accommodate the incoming H₂O molecule, and the H₂O_{ax}–Mg–H₂O_{eq} angles show that the equatorial H₂O molecules nearest to the approaching H₂O molecule are bending toward O also in an effort to accommodate this incoming group.

3.3.2.2.2 Hydrolysis of a Protonated Mg–O–Si Site

Because the stepwise approach of H₂O did not lead to the breaking of the Mg–O bond, the possibility of Mg–O bond lengthening as the cause of bond break was examined. The hydrolysis of a protonated Mg–O–Si site appears in **Figure 3-5**. The

(a)



(b)

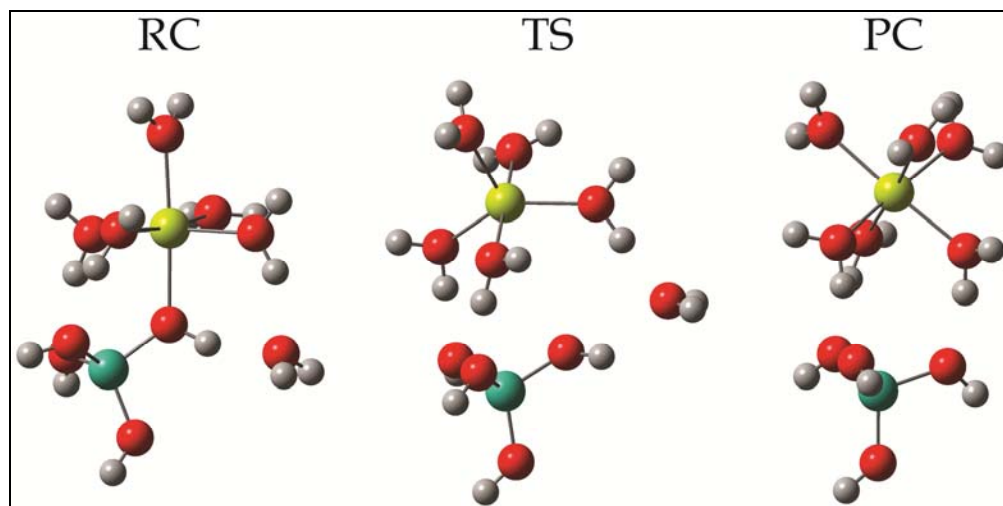


Figure 3-5: (a) The PES scan (blue line with blue diamonds) and optimized energy profile (red line with red diamonds) for hydrolysis of a protonated Mg–O–Si site where energy (kJ/mol) is plotted versus reaction coordinate. (b) The reaction mechanism for this reaction where the RC, TS, and PC are presented. The color scheme is the same as for **Figure 3-4**.

PES scan is comprised of two steps: the breaking of the Mg–O bond and the absorption of the incoming H₂O molecule by Mg²⁺. The reaction coordinate for the first step is the lengthening of the Mg–O bond, and in the second step, it is the decreasing of Mg–H₂O distance for the second hydration sphere H₂O molecule. The optimized RC, TS, and PC structures comprise the energy profile in **Figure 3-5a** and are shown as the reaction mechanism in **Figure 3-5b**. The RC in **Figure 3-5b** shows the second hydration sphere H₂O molecule H-bonded to the H⁺ on O and an equatorial H₂O molecule, in much the same manner as for the Ni–O–Si site. The Mg–O bond is lengthened until it breaks in the TS, where the negative frequency here corresponds to the breaking of the Mg–O bond, but the second hydration sphere H₂O molecule is not yet absorbed by the Mg²⁺ in the TS. The second hydration sphere H₂O molecule approaches the penta-coordinated Mg²⁺ between the TS and PC and is absorbed in the PC, and thus the PC is comprised of hexaaqua Mg²⁺ ion and silicic acid. The barrier height for this reaction is 54 kJ/mol.

The distances between the Mg²⁺ and the H₂O molecule from the second hydration sphere as well as between the Mg²⁺ and O are listed in **Table 3-3**. In the RC, the H₂O molecule from the second hydration sphere is 3.85 Å from the Mg²⁺, whereas the Mg–O distance is 2.14 Å. In the TS, the Mg–H₂O distance has increased to 4.28 Å, and the Mg–O distance has increased to 3.74 Å. The increase in the Mg–H₂O distance for the second hydration sphere H₂O molecule increases in the TS in order to allow for the rearrangement of the equatorial H₂O molecules around the Mg²⁺. The final distances for Mg–H₂O and Mg–O are 2.09 Å and 4.11 Å, respectively.

The bond angles around the Mg²⁺ in the TS are also included in **Table 3-3**. The bond angles surrounding the Mg²⁺ in the TS are listed using either O or the axial H₂O as

anchors and starting from the equatorial H₂O molecule in the right foreground of **Figure 3-5b** and continue counter-clockwise. The O–Mg–H₂O_{eq} are 70°, 105°, 72°, and 70°, whereas the H₂O_{ax}–Mg–H₂O_{eq} bond angles are 112°, 91°, 109°, and 93°. These show that the geometry around Mg²⁺ is approaching octahedral, which facilitates the absorption of the H₂O molecule from the second hydration sphere.

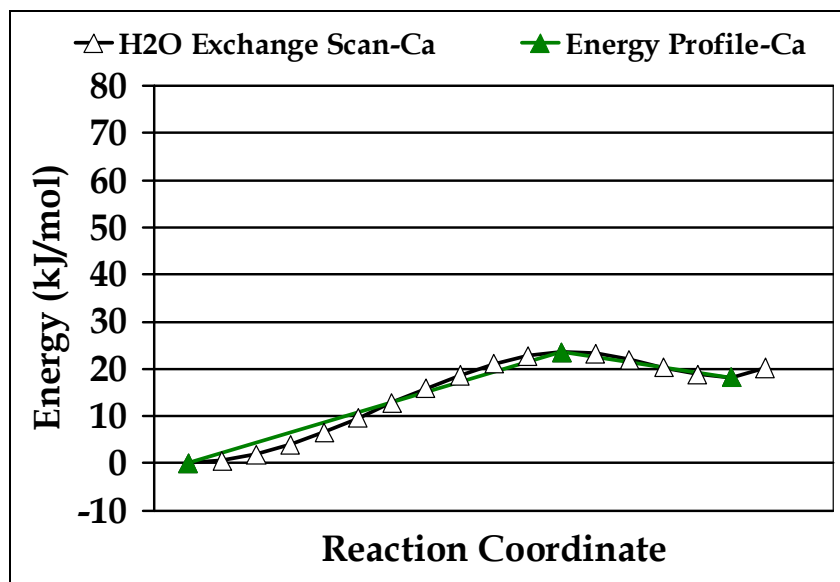
For protonated Mg–O–Si sites, the H₂O exchange and hydrolysis reactions are decoupled. The approach of a H₂O molecule causes a H₂O from the first hydration sphere to be replaced by one from the second, such that the Mg–O bond break is not a result of the approach of the H₂O molecule. Instead, the breaking of the Mg–O bond occurs as a result of the lengthening of the Mg–O bond.

3.3.2.3 Protonated Ca–O–Si Sites

3.3.2.3.1 Formation of Hepta-Coordinated Ca²⁺

An examination of H₂O exchange for Ca–O–Si sites was performed as well. In this reaction, the second hydration sphere H₂O molecule is absorbed by the Ca²⁺ and leads to the formation of a hepta-coordinated Ca²⁺. Thus a true H₂O exchange reaction does not occur for this site in these calculations; instead an H₂O addition occurs. The PES scan is performed where the incoming H₂O molecule approaches the Ca²⁺ (**Figure 3-6a**). The energies of the optimized RC, TS, and PC are shown in **Figure 3-6a** and the structures in **Figure 3-6b**. In the RC, the second hydration sphere H₂O molecule is H-bonded to the H⁺ on O and an equatorial H₂O molecule. As the second hydration sphere

(a)



(b)

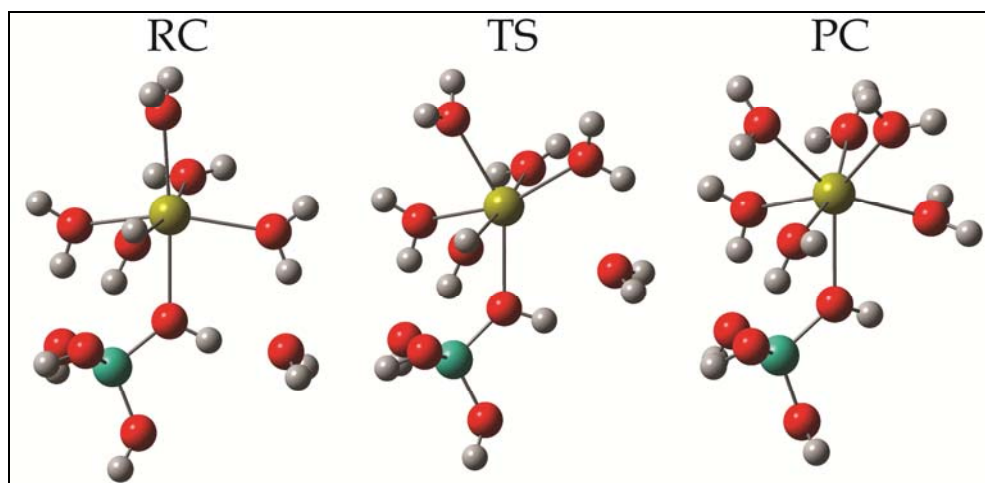


Figure 3-6: The (a) PES scan (black line with open triangles) and optimized energy profile (green line with closed triangles) for H₂O exchange around Ca²⁺ in a protonated Ca–O–Si site where energy (kJ/mol) is plotted versus reaction coordinate. (b) The reaction mechanism for this reaction where the RC, TS, and PC are presented. The calcium ion is gold, the silicon atom is turquoise, the oxygen atoms are red, and the hydrogen atoms are white. *The PES scan, geometry optimizations, and frequency calculations were performed by Dr. Amanda A. Olsen during her post-doctoral work at Penn State.*

H₂O molecule approaches the Ca²⁺, the equatorial H₂O molecules begin to rearrange to accommodate the incoming H₂O molecule as shown in the TS, and the negative frequency corresponds to the formation of this Ca–OH₂ bond. However, unlike both the protonated Ni–O–Si and Mg–O–Si sites, the H₂O molecule is absorbed to form a hepta-coordinated Ca²⁺, and thus the sole product is this newly-formed calcium silicate cluster. The barrier height for this reaction is 24 kJ/mol.

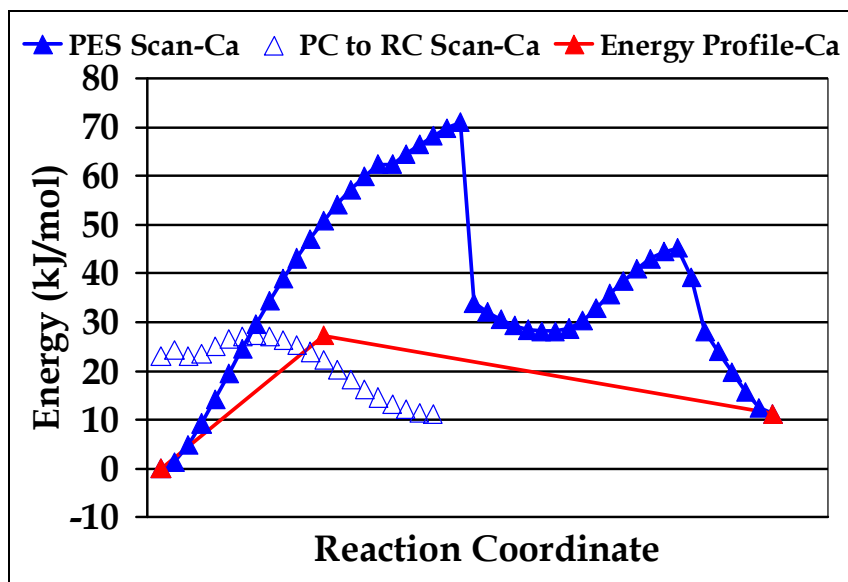
The Ca–H₂O distance for the H₂O molecule in the second hydration sphere and the Ca–O distance appear in **Table 3-3**. In the RC, the Ca–H₂O distance is 4.09 Å, and the Ca–O distance is 2.46 Å. The Ca–H₂O distance had decreased to 2.99 Å in the TS, while the Ca–O distance has remained nearly constant and is 2.45 Å. In the PC, the Ca–H₂O and Ca–O distances are nearly equal at 2.51 Å and 2.52 Å, respectively.

The bond angles surrounding Ca²⁺ in the TS are also included in **Table 3-3**. The bond angles surrounding the Ca²⁺ in the TS are listed using either the protonated O or the axial H₂O as anchors and starting from the equatorial H₂O molecule in the right foreground of **Figure 3-6b** and continue counter-clockwise. The O–Ca–H₂O_{eq} bond angles are 122°, 100°, 75°, and 77°, whereas the H₂O_{ax}–Ca–H₂O_{eq} bond angles are 84°, 93°, 84°, and 77°. These angles show that the octahedral geometry around Ca²⁺ is distorting, enabling accommodation of the seventh bonded group.

3.3.2.3.2 Hydrolysis of a Protonated Ca–O–Si Site

Because stepwise approach of H₂O did not lead to the breaking of the Ca–O bond, the Ca–O bond was lengthened as a possible cause for bond break. The hydrolysis of a

(a)



(b)

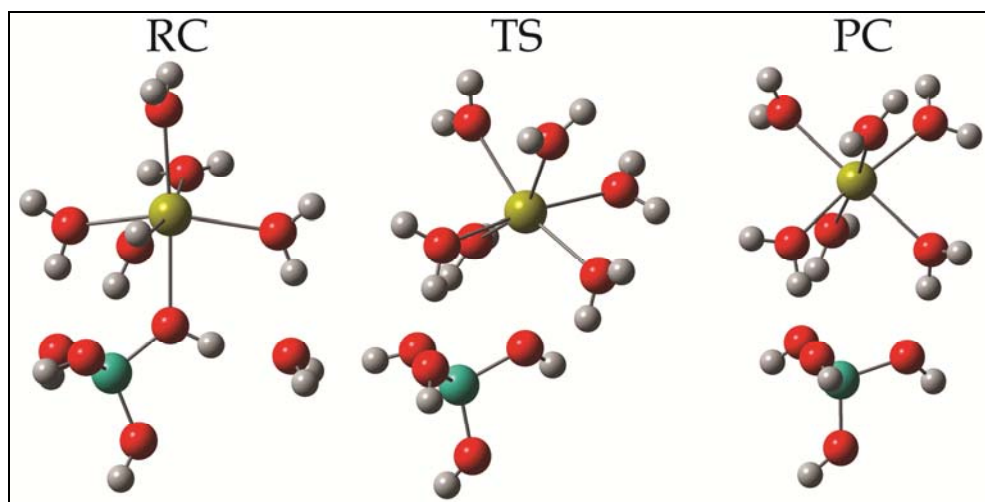


Figure 3-7: (a) The PES scan for the forward direction (blue line with closed triangles), the PES scan for the reverse direction (open blue triangles), and optimized energy profile (red line with closed triangles) for hydrolysis of a protonated Ca-O-Si site where energy (kJ/mol) is plotted versus reaction coordinate. (b) The reaction mechanism for this reaction where the RC, TS, and PC are presented. The color scheme is the same as for **Figure 3-6**.

protonated Ca–O–Si site appears in **Figure 3-7**. The initial PES scan appears in **Figure 3-7a** and is indicated by closed blue triangles and a blue line. The first step in this scan consists of the lengthening and subsequent breaking of the Ca–O bond, whereas the second step is the addition of the H₂O molecule to the first hydration sphere. This first attempt to determine the barrier height for the hydrolysis of a protonated Ca–O–Si site led to a barrier height of ~70 kJ/mol, which is higher than the expected value of 25–30 kJ/mol.⁴⁵

Therefore, the products from this scan were optimized and used to perform a scan of this reaction in the reverse direction, and the reverse direction scan appears as open blue triangles in **Figure 3-7a**. The TS from this scan was 27 kJ/mol higher in energy than the hexa-coordinated RC from the first scan, making it a representative structure of the overall mechanism. However, the scan in the reverse direction led to the hepta-coordinated Ca-silicate cluster shown in **Figure 3-6b**. Thus, the energy profile in **Figure 3-7a** and the reaction mechanism in **Figure 3-7b** consist of the hexa-coordinated RC, the TS from the reverse scan, and the hexa-coordinated PC.

In the reaction mechanism in **Figure 3-7b**, the H₂O molecule from the second hydration sphere is H-bonded to the H⁺ on the O and an equatorial H₂O molecule. The Ca–O bond is lengthened and eventually breaks in the TS, and the H₂O molecule from the second hydration sphere has already been absorbed. The negative frequency in the TS for this reaction corresponds to the breaking of the Ca–O bond. The PC is characterized by an increase in the Ca–O distance, given below, and a fully formed octahedral geometry around Ca²⁺.

The distances between the Ca^{2+} and the second hydration sphere H_2O molecule as well as between the Ca^{2+} and the O appear in **Table 3-3**. In the RC, the Ca– H_2O distance is 4.09 Å, and the Ca–O distance is 2.46 Å. The Ca– H_2O distance decreases to 2.44 Å in the TS, and the Ca–O distance increases to 3.04 Å. The final Ca– H_2O and Ca–O distances are 2.39 Å and 4.34 Å, respectively, in the PC.

The bond angles around Ca^{2+} in the TS are also included in **Table 3-3**. The bond angles surrounding the Ca^{2+} in the TS are listed using either the H_2O in the foreground or the H_2O in the background of **Figure 3-7b** as anchors and starting from the equatorial H_2O molecule in the right foreground of **Figure 3-7b** and continuing counter-clockwise. This method of analysis is used as opposed to the remaining bond angles given in **Table 3-3** because here the incoming H_2O molecule has already been absorbed in the TS. The $\text{H}_2\text{O}_{\text{fore}}\text{--Ca--H}_2\text{O}_{\text{eq}}$ bond angles are 83°, 92°, 79°, and 87°, whereas the $\text{H}_2\text{O}_{\text{back}}\text{--Ca--H}_2\text{O}_{\text{eq}}$ bond angles are 124°, 93°, 75°, and 92°. These angles show that the octahedral geometry around Ca^{2+} is nearly complete in the TS.

The formation of a hepta-coordinated Ca^{2+} in the H_2O exchange reaction for a protonated Ca–O–Si site warrants additional comment. The first hydration shell of Ca^{2+} has been shown to vary from six to eight.⁵⁸⁻⁶⁰ However, these simulations⁵⁸⁻⁶⁰ and experiments⁵⁹ were performed for the solution phase and not for the solid state. The molecular clusters used in this work are intended to represent individual sites on a mineral surface, which would be surrounded by many other surface sites. Therefore, the formation of a hepta-coordinated Ca^{2+} would be unlikely because of steric crowding.

The comparison of H_2O exchange and hydrolysis for protonated Ca–O–Si sites leads to a third reaction scheme where these two reactions are coupled. The formation of

a hepta-coordinated Ca^{2+} indicates that the breaking of the Ca–O bond is not affected by the approach of a H_2O molecule from the second hydration sphere. This fact is further reinforced by the elusiveness of the PES scan for the hydrolysis reaction for a protonated Ca–O–Si site and is manifested by the similarity of the barrier heights and rate constants, given in Section 3.3.4, for these reactions. The ability of Ca^{2+} to accommodate a large number of groups^{58,59} is what contributes to this complication. However, this elusiveness likely shows that a specific degree of freedom affects which path is chosen over the other.

3.3.3 Molecular Orbital (MO) and Natural Bond Order (NBO) Analysis of H_2O Exchange and Hydrolysis Reactions

The molecular orbitals (MOs) for the hydrolysis reactions are pictured in **Figure 3-8**, and the RCs and TSs for the reactions at protonated Ni–O–Si, Mg–O–Si, and Ca–O–Si sites are given. The orbitals surrounding Ni^{2+} during hydrolysis are comprised of three bonding orbitals and six anti-bonding orbitals, and the MO pictured in the top row of **Figure 3-8** for Ni–O–Si shows the bonding orbital for the Ni–O bond that will break in the TS. For protonated Mg–O–Si sites, the MOs surrounding Mg^{2+} are comprised of one bonding, one anti-bonding, and three anti-bonding lone pair orbitals. The bonding orbital pictured in the middle row of **Figure 3-8** represents the breaking of the Mg–O bond. For Ca–O–Si, all of the MOs surrounding Ca^{2+} in this reaction are anti-bonding. The MO representing the breaking of the Ca–O bond for the hydrolysis of protonated Ca–O–Si sites is shown in the bottom row of **Figure 3-8**, and the MO for Ca–O–Si has extended electron density on O, the H_2O in the second hydration sphere, an equatorial H_2O , and an axial H_2O group. For both Ni–O–Si and Mg–O–Si, the breaking of the M–O bond leaves

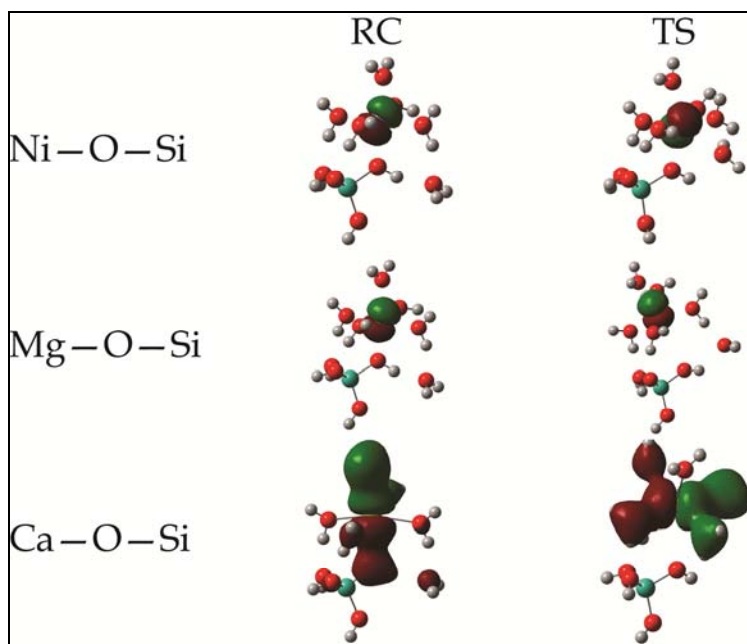


Figure 3-8: The molecular orbitals (MOs) for the hydrolysis of protonated Ni–O–Si, Mg–O–Si, and Ca–O–Si sites. The columns correspond to RCs or TSs, and the rows correspond to each silicate site.

an empty space where the second hydration sphere H_2O molecule can bond, and this is evident from the MOs in the TSs for these reactions. For Ca–O–Si, however, the second hydration sphere H_2O molecule has already been absorbed by Ca^{2+} , and the electron density in the MO has already rearranged to accommodate the new group. The energies of these orbitals are given in **Table 3-5**, and they increase in the order $\text{Ca}^{2+} < \text{Mg}^{2+} < \text{Ni}^{2+}$.

The MOs for the H_2O exchange reaction for protonated Mg–O–Si sites and the formation of the hepta-coordinated Ca^{2+} are shown in **Figure 3-9**. The MOs for the H_2O exchange reaction at a protonated Mg–O–Si site consist of one bonding, one anti-

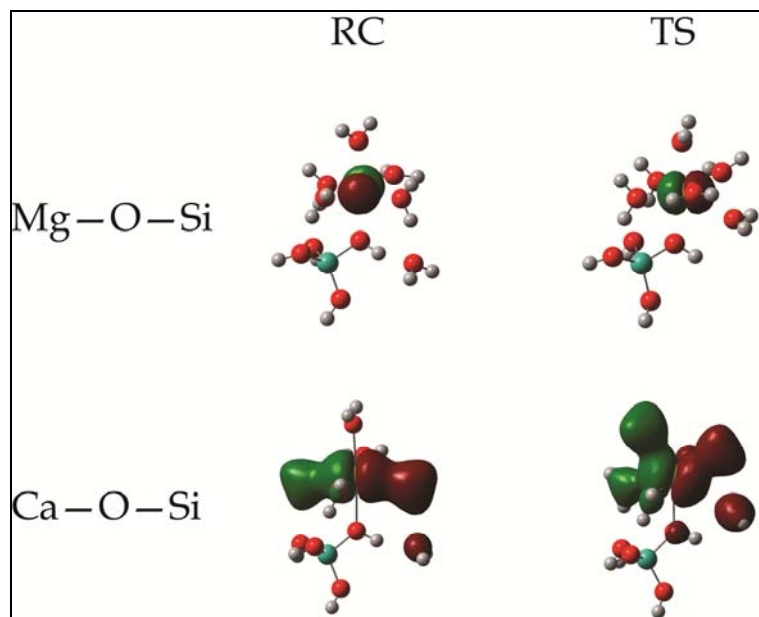


Figure 3-9: The molecular orbitals (MOs) for the H_2O exchange reaction for protonated Mg-O-Si sites as well as for the formation of the hepta-coordinated Ca-O-Si complex. The columns correspond to RCs or TSs, and the rows correspond to each silicate site.

bonding, and three anti-bonding lone pair orbitals. The MO pictured for this reaction in the top row of **Figure 3-9** corresponds to the breaking of the bond between Mg^{2+} and the first hydration sphere H_2O molecule. The MOs for the formation of the hepta-coordinated Ca^{2+} are also pictured in **Figure 3-9**. For this reaction, the MOs on Ca^{2+} consist of nine anti-bonding orbitals. The MO corresponding to the absorption of H_2O is unlike those in the TSs of the other reactions pictured in **Figures 3-8** and **3-9** in that electron density exists on the H_2O molecule from the second hydration sphere and on O. The similar phase on both the Ca^{2+} and the H_2O explains why the H_2O bonds so easily to Ca^{2+} , and the breaking of the $\text{Mg-H}_2\text{O}_{1\text{st}}$ bond in the TS enables the $\text{H}_2\text{O}_{2\text{nd}}$ to bond with

Table 3-5: Energies (kJ/mol) and change in energy (ΔE , kJ/mol) for relevant molecular orbitals (MOs) in the hydrolysis reactions of protonated Ni–O–Si, Mg–O–Si, and Ca–O–Si sites, the H₂O exchange reaction at the protonated Mg–O–Si site, and the formation of the hepta-coordinated Ca–O–Si site.

Protonated Site	RC (kJ/mol)	TS (kJ/mol)	ΔE (kJ/mol)
Hydrolysis			
Ni–O–Si	–286	–288	–2
Mg–O–Si	–201	–204	–3
Ca–O–Si	–126	–126	0
Mg ²⁺ H ₂ O Exchange and Hepta-Coordinated Ca ²⁺			
Mg–O–Si	–201	–203	–2
Ca–O–Si	–126	–126	0

Mg²⁺. The energies of these orbitals are presented in **Table 3-6**, and they show that the energies of the orbitals for Mg²⁺ are higher than those for Ca²⁺.

3.3.4 Rate Constants

The pre-exponential factors and rate constants for the reactions in **Reactions 3-4–9** are given in **Table 3-6**, and the rate constants were calculated using **Equation 3-10**. The rate constants follow the same trend as the barrier heights outlined above. There are two rate constants for the protonated Mg–O–Si site corresponding to the H₂O exchange and hydrolysis reactions, and these rate constants indicate that the hydrolysis reaction would proceed more rapidly than the H₂O exchange. Similarly for protonated Ca–O–Si sites, the two rate constants are for the formation of the hepta-coordinated complex and the hydrolysis of this site, where the rate constant of the former is higher than that of the latter. The log of these rate constants are plotted against the log of rate constants for H₂O

Table 3-6: The pre-exponential factors A (s^{-1}) and rate constants k (s^{-1}) for H_2O exchange and hydrolysis of protonated Ni–O–Si, Mg–O–Si, and Ca–O–Si sites.

Reaction Type	A (s^{-1})	k (s^{-1})
Ni–O–Si		
H_2O Exchange/Hydrolysis	1.7×10^{13}	7.2×10^{-1}
Mg–O–Si		
H_2O Exchange	3.1×10^{13}	2.6×10^1
Hydrolysis	1.4×10^{14}	4.7×10^4
Ca–O–Si		
Hepta-Coordinated Ca^{2+}	4.9×10^{13}	3.7×10^9
Hydrolysis	9.3×10^{13}	1.5×10^9

exchange around each corresponding metal ion^{17,57} in **Figure 3-10**, in a similar fashion to the analysis of Casey and Westrich.¹⁷ The trend is such that the rate constant for the reactions of each metal increases with the rate constant for H_2O exchange around the corresponding metal ion.

3.3.5 Overall Trends and Comparison to Experiment

The data in **Figure 3-10** replicate the trend observed by Casey and Westrich in experimental data,¹⁷ where the rates for end-member orthosilicate dissolution increase in the order $\text{Ni}^{2+} < \text{Mg}^{2+} < \text{Ca}^{2+}$. The reaction mechanisms described in this work provide additional insight into the relation of M–O bond energies, H_2O exchange rates, and mineral dissolution. The rate constant for the hydrolysis of a protonated surface site increases as the amount of energy required to break the M–O bond decreases, as has been discussed.^{11,15,16} However, what is most intriguing from these calculations is that H_2O exchange and hydrolysis reactions are not always intimately related at sites within the clusters, and for some minerals, these phenomena are exclusive for the Mg–O–Si and

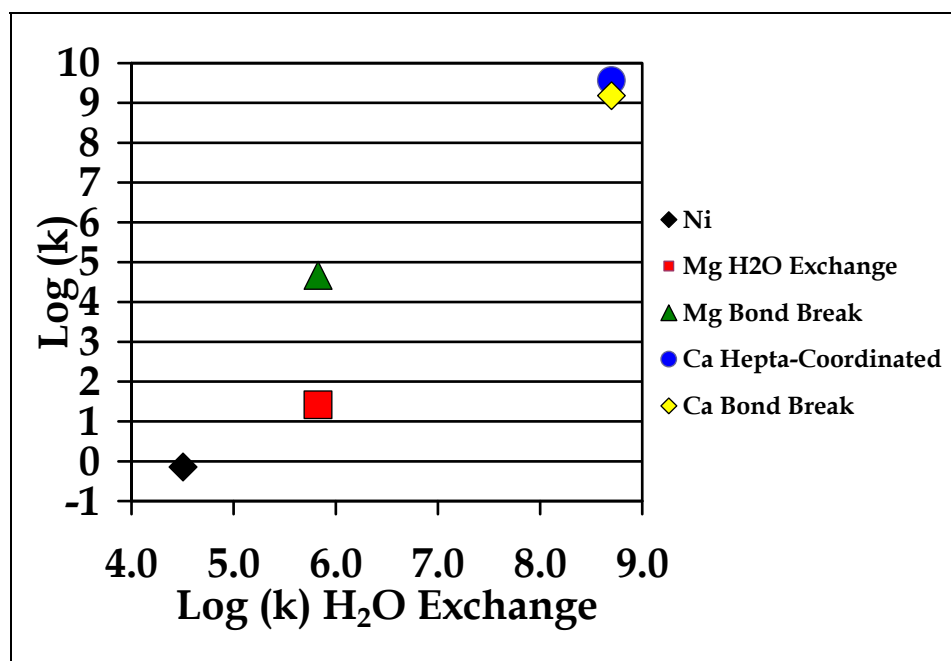


Figure 3-10: The log of the rate constant k (s^{-1}) for hydrolysis and H₂O exchange at protonated Ni-O-Si, Mg-O-Si, and Ca-O-Si sites (from this work) versus the log of the rate constant k (s^{-1}) of H₂O exchange for each of the corresponding metal ions.^{17,57}

Ca-O-Si linkages. The data in **Figure 3-10** also show that the H₂O exchange and hydrolysis rate constants are not equal and are likely two reactions occurring within the overall dissolution process.

Although the data in **Figure 3-10** replicate the trend of Casey and Westrich,¹⁷ the values are different. The dissolution rates of Casey and Westrich extend across ~5 orders of magnitude, whereas those in **Figure 3-10** differ by ~9 orders of magnitude. There are two likely explanations for this. The higher rate constants calculated here indicate that experimental phenomena contribute to the rate and somehow affect metal release from the surface. Secondly, the experiments of Casey and Westrich are at pH = 2, and although the clusters shown here represent protonated sites on the surface, the

phenomena are different because mineral surfaces contain a distribution of sites in protonated, neutral, and deprotonated states.

The results presented offer a molecular-scale insight into the link between H₂O exchange and the release of metal ions to solution during mineral dissolution. Comparison of the experimental and calculated energies in **Table 3-2** for H₂O exchange around Ni(H₂O)₆²⁺, Mg(H₂O)₆²⁺, and Ca(H₂O)₆²⁺ as well as the experimental rate constants given on the x-axis of **Figure 3-10** shows that there are differences between the H₂O exchange reactions for these ions and for the reactions described in this work. The presence of a silicic acid group instead of a sixth H₂O molecule around the metal ion is likely responsible for the difference in the H₂O exchange rate constants and the rate constants measured here.^{51,52}

There are two types of reactions in this regard. The first is where the silicic acid does not participate in the reaction; that is, the M–O bond remains intact. For both the H₂O exchange reaction at the protonated Mg–O–Si site and the formation of the hepta-coordinated Ca²⁺, this silicic acid group affects the rate constant. The H₂O exchange rate constant for Mg(H₂O)₆²⁺ is higher than the rate constant for the reaction in **Reaction 3-6**, and this shows that the silicic acid kinetically limits the H₂O exchange reaction at a protonated Mg–O–Si site. For the protonated Ca–O–Si site, on the other hand, the rate constant for the formation of the hepta-coordinated Ca²⁺ in the silicate molecular cluster is an order of magnitude larger than that for H₂O exchange on Ca(H₂O)₆²⁺. In this case, the silicic acid group is kinetically enhancing the H₂O exchange.

For the hydrolysis reaction of protonated Ni–O–Si, Mg–O–Si, and Ca–O–Si sites, the silicic acid group now participates in the reaction; that is, the breaking of the M–O

bond occurs. In these three reactions, the effect of the silicic acid group can also be examined. During hydrolysis, the H₂O from the second hydration sphere replaces the silicic acid group, and as a result, the rate constants for these reactions are different than those for H₂O exchange reactions for Ni(H₂O)₆²⁺, Mg(H₂O)₆²⁺, and Ca(H₂O)₆²⁺. For both the protonated Ni–O–Si and Mg–O–Si sites, the hydrolysis reactions have smaller rate constants than those for the H₂O exchange reactions, whereas for the protonated Ca–O–Si sites, the rate constants for the hydrolysis reaction is larger than that for H₂O exchange around Ca(H₂O)₆²⁺. These results suggest that the correlation of dissolution for end-member orthosilicate minerals with rate constants of H₂O exchange¹⁷ is coincidental and not an indication that H₂O exchange is the mechanism of dissolution.

However, both mineral dissolution and H₂O exchange rely on the breaking of M–O bonds and the formation of M–OH₂ bonds, and thus the link between M–O bond energy and mineral dissolution rates¹⁶ is also not surprising.¹¹ Furthermore, this connection may show that the bonding environment around the metal ion is similar in the mineral as in the M(H₂O)₆²⁺ ion, particularly for transition metals.⁵⁰ Moreover, the occupancy of the *d* orbitals on Ni²⁺ is the same for both the complexes shown and Ni(H₂O)₆²⁺, and the rates of H₂O exchange reactions are known to scale with *d* orbital occupancy for transition metals.^{50,52,53,61} The rate constants calculated also increase with the ionic size of the metal ion, as has been observed in other studies.^{15,17,50-52}

The hydrolysis of protonated Mg–O–Si sites proceeds through a dissociative (*D*) mechanism. This reaction can be characterized as such because of the decrease in coordination arising from the breaking of the Mg–O bond¹⁴ and because the Mg–O distance in the TS is > 1.0 Å longer than it was in the RC.⁴⁴ This dissociative type

mechanism is expected for the protonated Mg–O–Si sites based on known mechanisms for H₂O exchange around this ion,⁵⁰⁻⁵² and the primary reason for this expectation is the size of Mg²⁺.^{52,53}

On the other hand, the hydrolysis of protonated Ni–O–Si sites and the H₂O exchange reaction at protonated Mg–O–Si sites are in contrast to expectations.^{43,44,50-53} These two reactions appear to proceed through an associative interchange (*I_a*) mechanism for three reasons. First, the negative frequencies correspond to M–H₂O bond formation or concerted motion within the H-bonding network. Second, the Ni–O and Mg–H₂O_{1st} bonds have not lengthened significantly, < 1.0 Å, in the TS, and third, the bond angles of the octahedron are distorted in the TS. The Ni–O–Si sites are expected to react via dissociative mechanisms because of the population of the *d* orbitals^{50,52,53,61} and because the approach of the seventh molecule toward the face of the octahedron is electrostatically unfavorable.^{52,53} Also, the small size of the Mg²⁺ ion prevents the incorporation of a seventh group.^{52,53}

However, a recent review of ligand exchange mechanisms showed that Ni²⁺ can react via *D* or associative (*A*) mechanisms, depending upon the ligands present.⁵¹ In addition, two previous studies^{43,44} investigated H₂O exchange mechanisms around Ni(H₂O)₆²⁺ via ab initio calculations. A Hartree-Fock (HF) computational approach was employed because a DFT approach was not possible for transition metals at that time.⁴³ A TS for the associative, *A* or *I_a*, mechanisms,⁴³ was not isolated. The TSs presented were square pyramidal in geometry,^{43,44} and the hepta-coordinated TS and intermediate had two negative frequencies.⁴³ The author posed the possibility that these results arose as a

results of the method used.⁴³ These discrepancies in the literature demonstrate that additional investigations are needed.

The mechanism for the formation of the hepta-coordinated Ca^{2+} can be classified as associative (*A*) because the absorption of the incoming H_2O molecule forms a hepta-coordinated complex without negative frequencies. This is not surprising as an associative mechanism is expected for Ca^{2+} because of its ionic size.⁵² One could suggest that perhaps the development of a hepta-coordinated Ca^{2+} arises because of the employment of a computational approach via molecular clusters. In fact, DFT methods have been shown to prefer decreased coordination numbers for metal ions and thus dissociative mechanisms over associative ones.⁶¹ Therefore, the presence of a hepta-coordinated Ca^{2+} ion in this work is consistent with previous results⁵⁸⁻⁶⁰ and demonstrates this result is not an artifact of gas-phase clusters analyzed by DFT methods.

The hydrolysis of Ca-O-Si sites is difficult to classify. On one hand, the TS is characterized by the breaking of the Ca-O bond, which is indicative of a dissociative interchange (*I_d*) mechanism.^{51,52,61} However, the coordination number of Ca^{2+} has not decreased. On the other hand, the Ca-OH_2 bond is nearly fully-formed in the TS, and thus an *A* mechanism would seem to be an appropriate classification. In this case, the TS would be marked by a negative frequency corresponding to the formation of the Ca-OH_2 bond, which it is not. Thus, the hydrolysis reaction Ca-O-Si sites does not seem to fit into any of the classifications of Langford and Gray,¹⁴ and also this reinforces the observation that Ca^{2+} can react via *A* or *D* mechanisms.⁶² Additional analyses are necessary to further elucidate a straightforward description of the PES for the hydrolysis reaction at protonated Ca-O-Si surface sites.

3.4 Conclusions

The H₂O exchange reaction around the hexaaqua Mg²⁺ ion is described using gas-phase, IEFPCM, and super-molecule approximations. The barrier height from the IEFPCM calculation matched experimental values most closely, but the value from the super-molecule calculation was comparable within computational uncertainty. The reaction mechanisms are such that the gas-phase TS is characterized by a distorted pentagonal bipyramidal geometry, whereas both the IEFPCM and super-molecule approximations yield square-pyramidal geometries. These differences are manifested in the barrier heights of this reaction, which is ~30–40 kJ/mol higher for the gas-phase. These calculations show that DFT calculations can be used to approximate reactions in aqueous media.

The correlation between H₂O exchange reaction rates and the dissolution of end-member silicate minerals has been investigated via DFT methods. Three independent types of reaction mechanisms were determined for protonated Ni–O–Si, Mg–O–Si, and Ca–O–Si sites. The approach of the H₂O molecule from the second hydration sphere leads to the breaking of the Ni–O bond for protonated Ni–O–Si sites, whereas the H₂O exchange and hydrolysis reactions are independent for protonated Mg–O–Si sites. For protonated Ca–O–Si sites, however, a third situation develops where the approach of the second hydration sphere H₂O molecule is absorbed by the Ca²⁺, forming a hepta-coordinated species. The hydrolysis of protonated Ca–O–Si sites occurs via the lengthening of the Ca–O bond, but PES scans of this reaction were elusive.

The barrier heights from these reactions were used to calculate the rate constants according to the classical TST approximation. The calculated rate constants increase according to $\text{Ni}^{2+} < \text{Mg}^{2+} < \text{Ca}^{2+}$, which mimics experimental trends.^{15,17} In addition, the rate constants for the five silicate cluster reactions studied in this work are different than those for H_2O exchange around these ions in solution, and this demonstrates that the presence of a $\text{Si}(\text{OH})_4$ group as the sixth ligand instead of a H_2O molecule kinetically affects reactions around these metal ions.^{51,52} For both protonated Ni-O-Si and Mg-O-Si sites, the rate constants for H_2O exchange around $\text{Ni}(\text{H}_2\text{O})_6^{2+}$ and $\text{Mg}(\text{H}_2\text{O})_6^{2+}$ are higher than the rate constants for H_2O exchange and hydrolysis. However, for protonated Ca-O-Si sites, the rate constants for the formation of the hepta-coordinated complex as well as for the hydrolysis reaction are higher than those for H_2O exchange around $\text{Ca}(\text{H}_2\text{O})_6^{2+}$ in solution.

The reaction coordinates for these reactions were chosen according to whether the approach of the second hydration sphere H_2O molecule led to the breaking of the M-O ($\text{M} = \text{Ni}, \text{Mg}, \text{or Ca}$) bond. If not, then the lengthening of the M-O bond was used as the reaction coordinate until it broke, and then a second PES scan was performed to investigate the approach of the second hydration sphere H_2O molecule as the reaction coordinate. Using this approach, the link between H_2O exchange and hydrolysis reactions at protonated sites on end-member silicate minerals was studied.

3.5 References

- (1) Brantley, S. L. Reaction kinetics of primary rock-forming minerals under ambient conditions: fresh water geochemistry, weathering, and soils. In *Treatise on Geochemistry*; Turekian, K. K., Holland, H. D., Eds.; Pergamon Press: Oxford, 2003; Vol. 5; pp 73.
- (2) Giammar, D. E.; Bruant, R. G.; Peters, C. A. *Chem. Geol.* **2005**, *217*, 257.
- (3) Jarvis, K.; Carpenter, R. W.; Windman, T.; Kim, Y.; Nunez, R.; Alawneh, F. *Environ. Sci. Technol.* **2009**, *43*, 6314.
- (4) Roselle, G. T.; Baumgartner, L. P. *Geochim. Cosmochim. Ac.* **1995**, *59*, 1539.
- (5) Matter, J. M.; Takahashi, T.; Goldberg, D. *Geochem. Geophys. Geosy.* **2007**, *8*, Q02001.
- (6) Hanchen, M.; Prigione, V.; Storti, G.; Seward, T. M.; Mazzotti, M. *Geochim. Cosmochim. Ac.* **2006**, *70*, 4403.
- (7) Oelkers, E. H.; Gislason, S. R.; Matter, J. *Elements* **2008**, *4*, 333.
- (8) Van Essendelft, D. T.; Schobert, H. H. *Ind. Eng. Chem. Res.* **2009**, *48*, 2556.
- (9) IPCC *Special Report on Carbon Capture and Storage*; Cambridge University Press: Cambridge, 2005.
- (10) Rosso, J. J.; Rimstidt, J. D. *Geochim. Cosmochim. Ac.* **2000**, *64*, 797.
- (11) Stumm, W.; Wollast, R. *Rev. Geophys.* **1990**, *28*, 53.
- (12) Furrer, G.; Stumm, W. *Geochim. Cosmochim. Ac.* **1986**, *50*, 1847.
- (13) Ludwig, C.; Casey, W. H.; Rock, P. A. *Nature* **1995**, *375*, 44.
- (14) Langford, C. H.; Gray, H. B. *Ligand Substitution Processes*; W. A. Benjamin, Inc.: New York, 1966.
- (15) Casey, W. H. *J. Colloid Interf. Sci.* **1991**, *146*, 586.
- (16) Casey, W. H.; Rustad, J. R. *Annu. Rev. Earth Pl. Sc.* **2007**, *35*, 21.
- (17) Casey, W. H.; Westrich, H. R. *Nature* **1992**, *355*, 157.
- (18) Casey, W. H.; Ludwig, C. *Nature* **1996**, *381*, 506.
- (19) Westrich, H. R.; Cygan, R. T.; Casey, W. H.; Zemitis, C.; Arnold, G. W. *Am. J. Sci.* **1993**, *293*, 869.
- (20) Pokrovsky, O. S.; Schott, J. *Geochim. Cosmochim. Ac.* **2000**, *64*, 3299.
- (21) Davis, M. C.; Brouwer, W. J.; Wesolowski, D. J.; Anovitz, L. M.; Lipton, A. S.; Mueller, K. T. *Phys. Chem. Chem. Phys.* **2009**, *11*, 7013.
- (22) Nangia, S.; Garrison, B. J. *J. Phys. Chem. A* **2008**, *112*, 2027.
- (23) Xiao, Y.; Lasaga, A. C. *Geochim. Cosmochim. Ac.* **1994**, *58*, 5379.
- (24) Xiao, Y.; Lasaga, A. C. *Geochim. Cosmochim. Ac.* **1996**, *60*, 2283.
- (25) Morrow, C. P.; Nangia, S.; Garrison, B. J. *J. Phys. Chem. A* **2009**, *113*, 1343.
- (26) Morrow, C. P.; Kubicki, J. D.; Mueller, K. T.; Cole, D. R. *J. Phys. Chem. C* **2009**, DOI:10.1021/jp9057719.
- (27) Vosko, S. H.; Wilk, L.; Nusair, M. *Can. J. Phys.* **1980**, *58*, 1200.
- (28) Lee, C.; Yang, W.; Parr, R. G. *Phys. Rev. B* **1988**, *37*, 785.
- (29) Becke, A. D. *J. Chem. Phys.* **1993**, *98*, 1372.
- (30) Becke, A. D. *J. Chem. Phys.* **1993**, *98*, 5648.
- (31) Sousa, S. F.; Fernandes, P. A.; Ramos, M. J. *J. Phys. Chem. A* **2007**, *111*, 10439.

- (32) Adrian-Scotto, M.; Mallet, G.; Vasilescu, D. *J. Mol. Struc-Theochem* **2005**, 728, 231.
- (33) Rotzinger, F. P. *J. Phys. Chem. B* **2005**, 109, 1510.
- (34) Wang, J. W.; Rustad, J. R.; Casey, W. H. *Inorg. Chem.* **2007**, 46, 2962.
- (35) Casey, W. H.; Rustad, J. R.; Spiccia, L. *Chem.-Eur. J.* **2009**, 15, 4496.
- (36) Frisch, M. J.; Trucks, G. W.; Schlegel, H. B.; Scuseria, G. E.; Robb, M. A.; Cheeseman, J. R.; Montgomery, J. A., Jr.; Vreven, T.; Kudin, K. N.; Burant, J. C.; Millam, J. M.; Iyengar, S. S.; Tomasi, J.; Barone, V.; Mennucci, B.; Cossi, M.; Scalmani, G.; Rega, N.; Petersson, G. A.; Nakatsuji, H.; Hada, M.; Ehara, M.; Toyota, K.; Fukuda, R.; Hasegawa, J.; Ishida, M.; Nakajima, T.; Honda, Y.; Kitao, O.; Nakai, H.; Klene, M.; Li, X.; Knox, J. E.; Hratchian, H. P.; Cross, J. B.; Bakken, V.; Adamo, C.; Jaramillo, J.; Gomperts, R.; Stratmann, R. E.; Yazyev, O.; Austin, A. J.; Cammi, R.; Pomelli, C.; Ochterski, J. W.; Ayala, P. Y.; Morokuma, K.; Voth, G. A.; Salvador, P.; Dannenberg, J. J.; Zakrzewski, V. G.; Dapprich, S.; Daniels, A. D.; Strain, M. C.; Farkas, O.; Malick, D. K.; Rabuck, A. D.; Raghavachari, K.; Foresman, J. B.; Ortiz, J. V.; Cui, Q.; Baboul, A. G.; Clifford, S.; Cioslowski, J.; Stefanov, B. B.; Liu, G.; Liashenko, A.; Piskorz, P.; Komaromi, I.; Martin, R. L.; Fox, D. J.; Keith, T.; Al-Laham, M. A.; Peng, C. Y.; Nanayakkara, A.; Challacombe, M.; Gill, P. M. W.; Johnson, B.; Chen, W.; Wong, M. W.; Gonzalez, C.; Pople, J. A. Gaussian03, Revision E.01; Gaussian, Inc.: Wallingford, CT, 2004.
- (37) Dennington, R., II; Keith, T.; Millam, J. GaussView, Version 4.1; Semichem, Inc.: Shawnee Mission, KS, 2007.
- (38) Cancès, E.; Mennucci, B.; Tomasi, J. *J. Chem. Phys.* **1997**, 107, 3032.
- (39) Keith, T. A.; Frisch, M. J. Inclusion of explicit solvent molecules in a self-consistent-reaction field model of solvation. In *ACS Symposium Series*; Smith, D. A., Ed.; American Chemical Society: Washington, D.C., 1994; Vol. 569; pp 22.
- (40) Duncan, W. T.; Bell, R. L.; Truong, T. N. *J. Comp. Chem.* **1998**, 19, 1039.
- (41) TheRate. The CSE-Online Project: University of Utah, 2006.
- (42) Kang, S. K.; Lam, B.; Albright, T. A.; O'Brien, J. F. *New J. Chem.* **1991**, 15, 757.
- (43) Rotzinger, F. P. *J. Am. Chem. Soc.* **1996**, 118, 6760.
- (44) Rotzinger, F. P. *J. Am. Chem. Soc.* **1997**, 119, 5230.
- (45) Tsutsui, Y.; Wasada, H.; Funahashi, S. *B. Chem. Soc. Jpn.* **1997**, 70, 1813.
- (46) Bock, C. W.; Kaufman, A.; Glusker, J. P. *Inorg. Chem.* **1994**, 33, 419.
- (47) Markham, G. D.; Glusker, J. P.; Bock, C. L.; Trachtman, M.; Bock, C. W. *J. Phys. Chem.* **1996**, 100, 3488.
- (48) Pavlov, M.; Siegbahn, P. E. M.; Sandstrom, M. *J. Phys. Chem. A* **1998**, 102, 219.
- (49) Dudev, T.; Lim, C. *J. Phys. Chem. A* **1999**, 103, 8093.
- (50) Helm, L.; Merbach, A. E. *J. Chem. Soc.-Dalton* **2002**, 633.
- (51) Helm, L.; Merbach, A. E. *Chem. Rev.* **2005**, 105, 1923.
- (52) Richens, D. T. *Chem. Rev.* **2005**, 105, 1961.
- (53) Ducommun, Y.; Newman, K. E.; Merbach, A. E. *Inorg. Chem.* **1980**, 19, 3696.
- (54) Neely, J.; Connick, R. *J. Am. Chem. Soc.* **1970**, 92, 3476.
- (55) Bechtold, D. B.; Liu, G.; Dodgen, H. W.; Hunt, J. P. *J. Phys. Chem.* **1978**, 82, 333.

- (56) Bleuzen, A.; Pittet, P. A.; Helm, L.; Merbach, A. E. *Magn. Reson. Chem.* **1997**, *35*, 765.
- (57) Helm, L.; Merbach, A. E. *Coord. Chem. Rev.* **1999**, *187*, 151.
- (58) Ikeda, T.; Boero, M.; Terakura, K. *J. Chem. Phys.* **2007**, *127*, 074503.
- (59) Jalilehvand, F.; Spangberg, D.; Lindqvist-Reis, P.; Hermansson, K.; Persson, I.; Sandstrom, M. *J. Am. Chem. Soc.* **2001**, *123*, 431.
- (60) Schwenk, C. F.; Loeffler, H. H.; Rode, B. M. *J. Chem. Phys.* **2001**, *115*, 10808.
- (61) Rotzinger, F. P. *Chem. Rev.* **2005**, *105*, 2003.
- (62) Akesson, R.; Pettersson, L. G. M.; Sandstrom, M.; Wahlgren, U. *J. Am. Chem. Soc.* **1994**, *116*, 8705.

Chapter 4

Density Functional Theory Modeling of Water on Forsterite (100) and (010) Surfaces

4.1 Introduction

The work builds upon the investigation of Mg^{2+} release from forsterite in Chapter 2. Density functional theory molecular dynamics (DFT-MD) simulations are employed to investigate the structures and relative stabilities of the forsterite (100) and (010) cleavage planes. Instead of studying how the Mg–O bond breaks to effect the release of Mg^{2+} ions to solution, the focus here is to determine the types of functional groups present on the forsterite surface at the aqueous-mineral interface, and surface sites exist as O^- , O_{br} , OH , and H_2O groups on both the forsterite (100) and (010) surfaces. Reactions between surface groups and between surface groups and H_2O molecules in solution are possible throughout the simulations, and the evolution of surface functional groups over 10 ps is described. Comparisons are given to previous computational and experimental observations.

Characterization of sites on the forsterite surface is necessary for accurate descriptions of dissolution, as the types of functional groups present control the dissolution rate.^{1,2} Currently, the Brunauer-Emmett-Teller (BET) surface area³ is often used to estimate the surface area of a mineral sample, where an inert gas is adsorbed to the mineral surface, and the volume that adsorbs is used to determine the surface area of the mineral. This term is then used to estimate the surface contribution to the dissolution

rate law. The overall dissolution rate does not correlate well with the BET surface area in many instances,⁴ and as a result, chemical probe molecules are being used to determine which sites are the most reactive on mineral surfaces.^{4,5} In addition, the adsorption of the inert gas during a BET surface area measurement is not sensitive to surface topographical features,⁶ and this serves as another disadvantage to the technique in that surface topography also contributes to the dissolution rate of a mineral because preferential dissolution occurs at defect sites and edge sites.^{7,8}

In addition to descriptions of which functional groups are present on the forsterite mineral surface, the relative stabilities of crystallographic planes also contribute to observed dissolution rates. The two major reasons for this are that each crystallographic plane will be present in varying concentrations^{9,10} and because each plane will be terminated with a different number of each functional group.¹¹ The relative stabilities of forsterite (100) and (010) surfaces have been investigated using atomistic simulations.^{9,12} The means by which the forsterite surface is cleaved affects which surface is determined to be more stable, as too many dangling bonds in the cleavage plane can lead to a surface that is heavily covered in defects.¹² This difference in cleavage of the surface plane may be why the (100) surface was found to be more stable in one study⁹ and less stable in another.¹² These conflicting conclusions demonstrate that additional insight is needed to isolate which of these two surfaces is more stable than the other, and such a conflict can be resolved with the use of density functional theory molecular dynamics (DFT-MD) simulations.

Adsorption of water onto the forsterite mineral surface has several overarching applications. Forsterite is one of the most common astronomical minerals,^{12,13} and

therefore, understanding the structure of monolayers of water on the forsterite mineral surface provides insight into a number of astronomical phenomena. The first is how water was delivered to Earth,^{12,14,15} as water is believed to have adsorbed onto forsterite grains during planet formation.¹⁵ In addition, the adsorption of water onto forsterite influences the current concentration of water in Earth's mantle,¹⁶⁻²⁰ and the presence of water affects seismic processes¹⁷⁻¹⁹ and the global water cycle¹⁸ throughout Earth's surface. Lastly, forsterite has been found on the surface of Mars, and thus, understanding the structure of water on the surface of this mineral enables a description of the mineralogical history of this planet.²¹⁻²³

DFT-MD simulations for the investigation of the surface structure of the forsterite (100) and (010) planes in both hydrated and aqueous environments are particularly useful because both bond-breaking and bulk scale behaviors can be studied simultaneously. DFT-MD simulations via the Vienna Ab-initio Simulation Package (VASP)²⁴⁻²⁷ have been employed to model the adsorption of H₂O molecules to mineral surfaces,²⁸ the aqueous-mineral interface,^{29,30} the adsorption of ions from solution to the mineral surface,³¹ and the vibrational spectrum of H₂O molecules adsorbed to the mineral surface.³² The advantage of using DFT-MD versus classical MD in part is that the results from the simulations are not artifacts of the potentials or fitting parameters used.²⁹ In addition, reactions between surface species and solution species can occur in DFT-MD, whereas many classical force fields rely on non-dissociable H₂O molecules. Consequently, DFT-MD allows for a more realistic description of the surface and is less subject to the initial configuration selected. This approach builds upon previous work of

using single surface sites to describe the release of Mg^{2+} from the forsterite surface² by increasing the number of surface sites and modeling cooperative H-bonding effects.

The goal of this work is to determine the structure of the forsterite (100) and (010) surfaces in both H_2O monolayer and bulk aqueous environments. The energetic stability of each will be calculated via DFT-MD simulations with the intent that these simulations will provide insight for experimental characterization and dissolution studies. Use of quantum mechanical calculations enables bond-breaking and bond-forming processes to be included in the simulations, and thus H^+ and H_2O transfers between surface groups and at the aqueous-mineral interface are possible. Each surface is investigated at a unit cell scale which permits the inclusion of several surface sites, and thus the protonation states on the surfaces in hydrated and aqueous environments will be determined. The findings of this study are then compared with previous computational and experimental results.

4.2 Computational Details

Density functional theory molecular dynamics (DFT-MD) simulations have the benefits of including the electronic structure of atoms as well as long enough timescales for the investigation of physicochemical processes. Simulations are made practical by employing pseudopotentials that separate the non-reacting core electrons from the valence electrons during the calculation of the electronic structure.³³ The Vienna Ab-initio Simulation Package (VASP)²⁴⁻²⁷ employs a plane wave approximation to the band structure via the projector augmented-wave (PAW) approach.³⁴ The advantages of the

PAW approach are the elimination of adjustments to the core electrons and the ability to achieve chemical behaviors similar to those observed in all-electron methods.³⁵ The improvements by Kresse and Joubert on Blöchl's original description are especially useful for silicate systems because the properties of a siliceous substance were tested in the training set.²⁴ The calculations described in this work were constructed with an automatic generation of k points within the Brillouin zone according to the Monkhorst-Pack approach.³⁶ The energy cutoff for the energy-minimization of samples was 500 eV, which is a reasonably accurate cut-off for these systems.³⁴

An overview of the computational scheme appears in **Figure 4-1**. The coordinates for the forsterite (100) and (010) surfaces were taken from the Cerius² mineral structures database,³⁷ and the bulk crystal was energy-minimized such that the periodic cell boundaries were permitted to change. The force and stress tensors were calculated. Simultaneously, the positions of all ions were permitted to relax.²⁵ The coordinates of the bulk model were used as the lattice parameters for further surface simulations, and the energy of this energy-minimized structure is E_{bulk} .

Surface slabs were cleaved from the forsterite mineral structure using the Surface Builder module in the Cerius² database³⁷ along the (100) and (010) cleavage planes in such a way as to minimize the number of dangling bonds. The forsterite (100) slab is $10.2430 \times 6.0030 \text{ \AA}^2$ and is 11.75 \AA thick, and this cell has eight Mg_2SiO_4 formula units. The forsterite (010) slab is $12.0060 \times 9.5380 \text{ \AA}^2$ and is 15.75 \AA thick, and this cell has 16 formula units. These slabs were also energy-minimized allowing all ions to relax but restricting the dimensions of the simulation cell. The final dimensions of the forsterite (100) cell were $19.6954 \times 10.2430 \times 6.0030 = 1211.0 \text{ \AA}^3$, and the forsterite (010) cell was

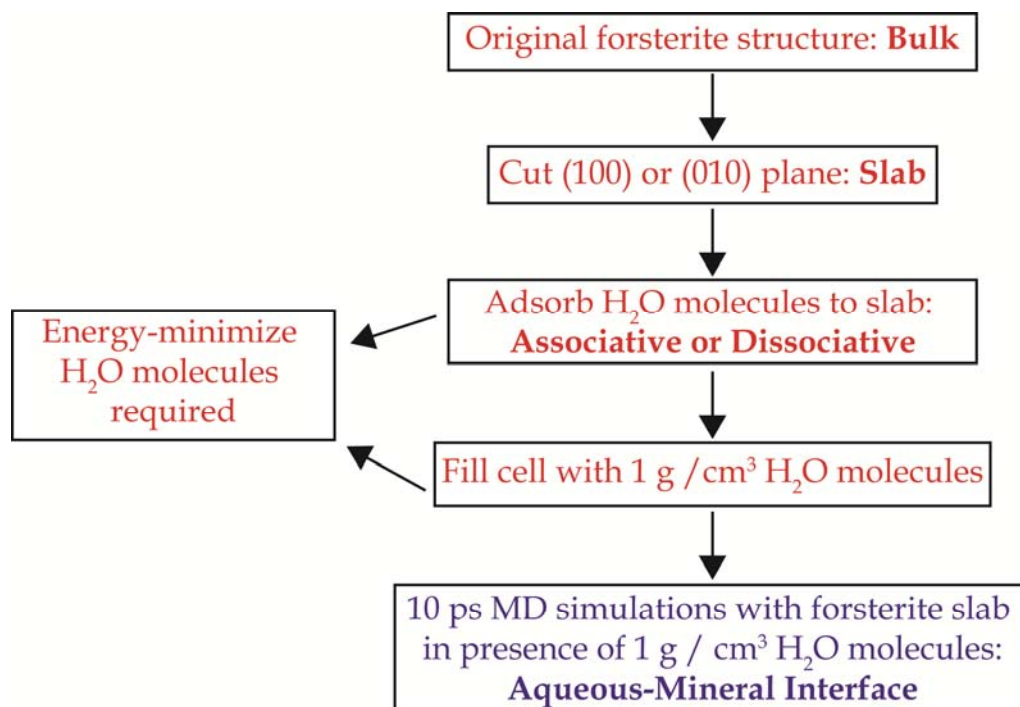


Figure 4-1: Overview of computational method for simulation aqueous-mineral interface. The steps in red are those that are energy-minimized, and that in purple is the MD simulations. Additional details about the energy contributions of each are covered in the text.

$21.3124 \times 12.0060 \times 9.5380 = 2440.6 \text{ \AA}^3$. The energy of these energy-minimized slabs are denoted E_{slab} .

Each surface was then covered with H_2O or H^+ and OH^- groups to model associative and dissociative adsorption, respectively. A neutral charge in the system was maintained by adjusting the number of H^+ and OH^- groups bonded to the surface. These model surfaces were energy-minimized, and again all ions were permitted to relax. The free energy of the energy-minimized monolayer samples is E_{ads} . The H_2O molecules adsorbed to each surface in the monolayer system were energy-minimized separately in a cell whose dimensions were the same as the vacuum portion of the forsterite (100) and

(010) simulation cells, and the free energy of this energy-minimized configuration is labeled as E_{hyd} .

The surface energy indicates the relative stability of a surface structure,³⁸ and the values calculated in this work will be used to determine whether the forsterite (100) or (010) surface is more stable for the slabs, hydrated surfaces, and at the aqueous-mineral interface. According to the description of de Leeuw *et al.*, the surface energy γ of a mineral slab is calculated according to (1):

$$\gamma = \frac{E_{slab} - E_{bulk}}{A} \quad \mathbf{1}$$

where A is the area of the surface (in units of m^2).³⁸ For all the samples in this work, A is multiplied by a factor of two to account for both sides of the slab, as both are permitted to react as a result of the periodic boundary conditions. E_{slab} and E_{bulk} are each reflective of the number of Mg_2SiO_4 formula units within the slab and bulk, respectively. The relative energy of the hydrated slabs are calculated according to (2):³⁸

$$\gamma = \frac{E_{ads} - (E_{bulk} + E_{hyd})}{A} \quad \mathbf{2}$$

An additional system was designed to model the low density of water that could exist if vapor-phase H_2O adsorbed onto the surface. In this system, the energy-minimized (100) surface covered with a distribution of functional groups, formed from six adsorbed H_2O molecules, was solvated by 12 H_2O molecules to simulate the aqueous-mineral interface. The six H_2O molecules used to hydrate the surface and the 12 H_2O molecules used to solvate the surface were separately energy-minimized in cells that were the same size as the vacuum above the (100) surface. The energies of these molecules

are as listed as E_{hyd} and E_{solv} in **Table 4-1**, respectively. DFT-MD simulations were performed with a 0.5 fs timestep for a total of 10 ps, and the final 5 ps were used for data analysis. The advantage to this model is that less H₂O molecules within the simulation cell allow for more freedom of H₂O arrangement. Following similar logic to de Leeuw *et al.*,³⁸ the relative energy of this low density system was calculated according to (3):

$$\gamma = \frac{E_{int} - (E_{bulk} + E_{hyd} + E_{ads} + E_{solv})}{A} \quad 3$$

The models studied in this work were visualized with either Cerius²³⁷ or Materials Studio.³⁹

4.3 Results and Discussion

4.3.1 Bulk Forsterite Structure

The original and energy-minimized structures for bulk forsterite are shown in **Figure 4-2** and correspond to 16 formula units. The lattice parameters of the original sample were (9.538 x 10.243 x 12.006) Å³, and those for the DFT energy-minimized structures were (9.600 x 10.321 x 12.095) Å³. The errors in calculated lattice parameters of > 1% are excellent for the DFT methodology used here.⁴⁰ The angles of the energy-minimized bulk structure are $\alpha = \beta = \gamma = 90^\circ$. The energy-minimized structure has a free energy of -4.65×10^3 kJ/mol, and this value is listed as E_{bulk} in **Table 4-1**.

Table 4-1: Energies (kJ/mol) and lattice parameters (\AA^3) for forsterite samples studied throughout this work.

Sample	Lattice Parameters	Energy
Bulk		
Input	9.538 x 10.243 x 12.006	
Output	9.600 x 10.321 x 12.095	-4.65×10^3
Hydrated Forsterite (100)		
Slab		-4.48×10^3
Associative Adsorption	8 H ₂ O molecules	-1.13×10^4
	Slab + Adsorbed H ₂ O	-4.82×10^4
Dissociative Adsorption	8 H ₂ O molecules	-1.13×10^4
	Slab + Adsorbed H ₂ O	-4.83×10^4
Low-Density Solvated Forsterite (100)		
Aqueous-Mineral Interface	6 H ₂ O molecules	-8.43×10^3
	Slab + Adsorbed H ₂ O	-4.54×10^4
	12 H ₂ O molecules	-1.70×10^4
	Hydrated slab + 12 H ₂ O molecules	-6.22×10^4
Hydrated Forsterite (010)		
Slab		-4.39×10^3
Associative Adsorption	12 H ₂ O molecules	-1.70×10^4
	Slab + Adsorbed H ₂ O	-8.81×10^4
Dissociative Adsorption	8 H ₂ O molecules	-1.13×10^4
	Slab + Adsorbed H ₂ O	-8.31×10^4

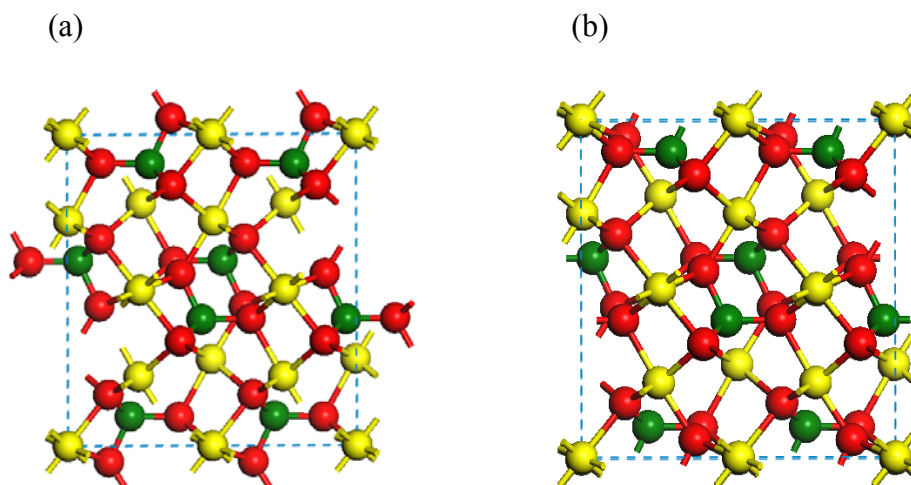
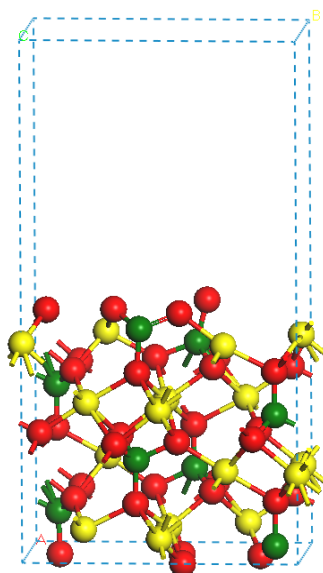


Figure 4-2: (a) Initial structure of bulk forsterite from Cerius² mineral database.^{37,39} (b) Energy-minimized bulk forsterite structure.³⁹ The Mg²⁺ ions are yellow, the Si atoms are green, and the O atoms are red.

4.3.2 Forsterite (100) and (010) Slabs

Surface structures are shown in **Figures 4-3** and **4-4** for the forsterite (100) and (010) cleavage planes, respectively. The numbers of functional groups on the forsterite (100) and (010) slabs are given in **Table 4-2**. The initial (100) cleavage plane contained five O_{br} and two O⁻ functional groups on the surface, where the total number of sites possible was 36. Upon energy-minimization, all of the O atoms on the surface became O_{br} groups. The initial (010) sample, on the other hand, had 28 O_{br} and four O⁻ out of a possible 80 sites on the surface. The energy-minimized (010) cleavage plane had 28 O_{br} and four O⁻ functional groups, which is the same as the original sample. The total possible sites refers to the number of dangling surface bonds on both Mg²⁺ ions and Si

(a)



(b)

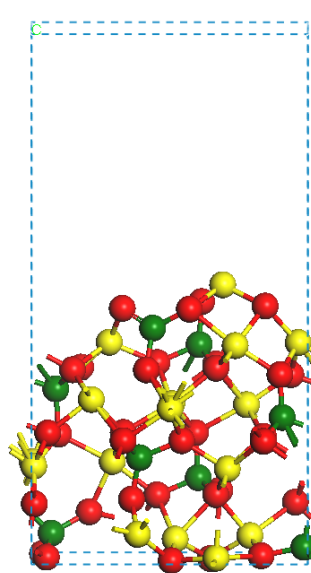
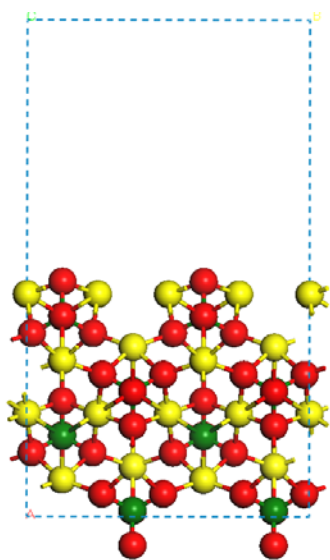


Figure 4-3: Forsterite (100) slab. (a) Initial structure.^{37,39} (b) Energy-minimized structure.³⁹ The color scheme is the same as **Figure 4-1**.

(a)



(b)

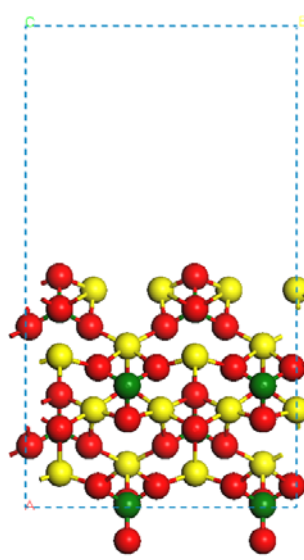


Figure 4-4: Forsterite (010) slab. (a) Initial structure.^{37,39} (b) Energy-minimized structure.³⁹ The color scheme is the same as **Figure 4-1**.

atoms on the surface of these mineral samples, and this terminology will be continued throughout this work.

The energies of the energy-minimized slabs are listed in **Table 4-1** as E_{slab} . The total energy for the forsterite (100) slab was -4.48×10^3 kJ/mol, and the total energy for the forsterite (010) slab was -4.39×10^3 kJ/mol. Each slab had 8 and 16 Mg_2SiO_4 formula units for the (100) and (010) slabs, respectively.

The initial structure of the (100) cleavage plane was such that atoms were more free to move, and thus, the surface underwent significant rearrangement during energy-minimization. This observation is in contrast to what was seen for the (010) cleavage plane, where the configuration of atoms on the surface did not enable significant rearrangement. This may in part explain why a lower energy structure was attained for the (100) cleavage plane as a result.

The relative energies γ of the (100) and (010) slabs are given in **Table 4-3**. For the (100) slab, γ is 1.81 J/m^2 , while for the (010) slab, γ is 3.07 J/m^2 . Thus, the (100) surface is predicted to be more stable than the (010) surface in vacuum because of the lower surface energy.

4.3.3 Associative and Dissociative Adsorption of H_2O to Forsterite Slabs

The adsorption of H_2O molecules to the forsterite (100) and (010) surfaces was modeled to determine whether associative or dissociative adsorption was more favorable for each plane. The energy values for these samples are given in **Table 4-1** as E_{ads} , and the number of functional groups on each respective original and energy-minimized

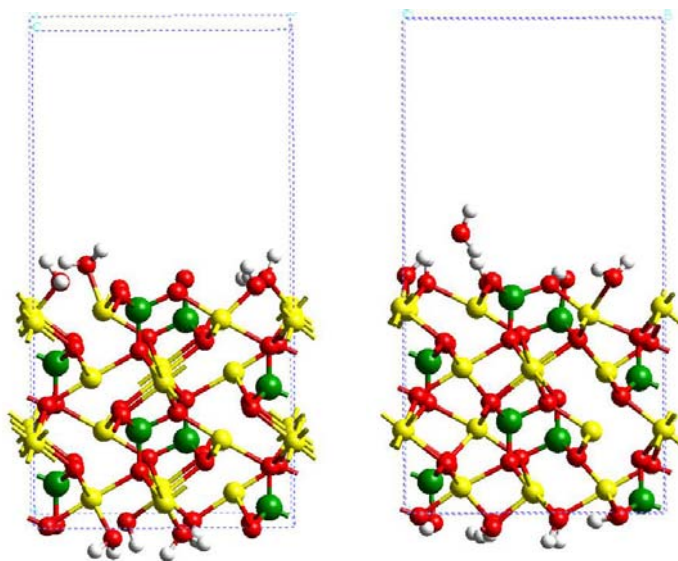
Table 4-2: Type and number of functional groups on the bulk, slab, hydrated, and aqueous-mineral interface surfaces for forsterite (100) and (010). The raw number and the fraction of total sites are given.

Adsorption	Structure	O _{br}	O ⁻	OH	H ₂ O
Hydrated Forsterite (100): 36 total possible surface sites					
Slab	Original	5 (14%)	2 (6%)	0 (0%)	0 (0%)
	Energy-minimized	7 (19%)	0 (0%)	0 (0%)	0 (0%)
Associated	Original	6 (17%)	2 (6%)	0 (0%)	8 (22%)
	Energy-minimized	3 (8%)	0 (0%)	10 (28%)	2 (6%)
Dissociated	Original	0 (0%)	0 (0%)	16 (44%)	0 (0%)
	Energy-minimized	2 (6%)	0 (0%)	12 (33%)	2 (6%)
Low-Density Solvated Forsterite (100): 36 total possible surface sites					
Aqueous Interface	t = 0 ps	2 (6%)	1 (3%)	10 (28%)	2 (6%)
	t = 10 ps	2 (6%)	2 (6%)	9 (25%)	3 (8%)
Hydrated Forsterite (010): 80 total possible surface sites					
Slab	Original	28 (35%)	4 (5%)	0 (0%)	0 (0%)
	Energy-minimized	28 (35%)	4 (5%)	0 (0%)	0 (0%)
Associated	Original	28 (35%)	4 (5%)	0 (0%)	12 (15%)
	Energy-minimized	26 (33%)	4 (5%)	4 (5%)	8 (10%)
Dissociated	Original	24 (30%)	0 (0%)	16 (20%)	0 (0%)
	Energy-minimized	25 (31%)	0 (0%)	14 (18%)	1 (1%)

Table 4-3: Relative energies (J/m²) for the forsterite (100) and (010) slabs, hydrated surfaces, and aqueous-mineral interfaces.

Surface Plane		Slab	Hydrated Surface		Aqueous-Mineral Interface
			Associative	Dissociative	
(100)	Pore Water System	1.8	0.32	0.26	61.8
(010)		3.1	2.47	1.89	—

(a)



(b)

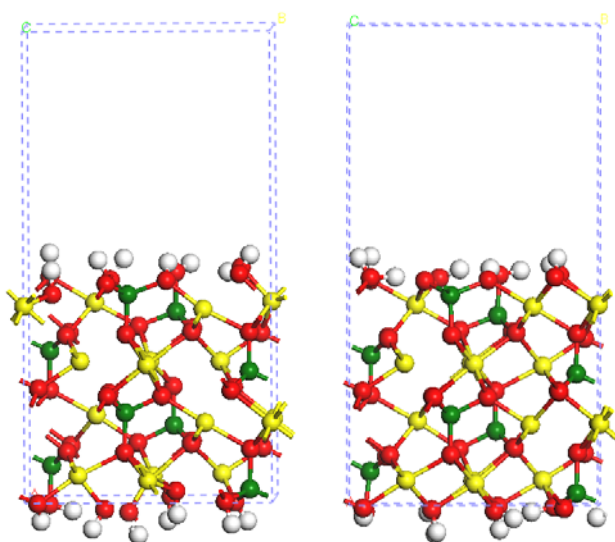
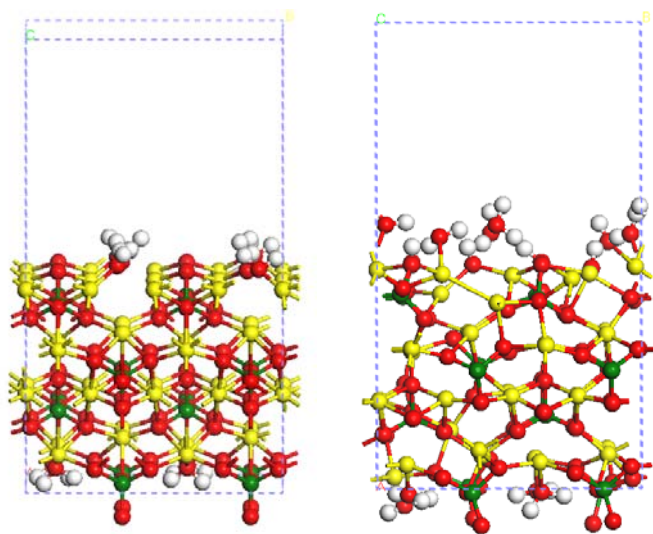


Figure 4-5: Hydrated forsterite (100) surface. a) Original (left) and energy-minimized (right) surface structures for associative adsorption of H_2O molecules. b) Original (left) and energy-minimized (right) surface structures for dissociative adsorption of H_2O molecules. The color scheme is such that Mg atoms are yellow, Si atoms are green, O atoms are red, and H atoms are white.^{37,39}

surface is listed in **Table 4-2**. For the (100) plane, associative adsorption and dissociative adsorption of H₂O molecules were modeled with eight H₂O molecules adsorbed to the slab where the total energy contribution from the H₂O molecules adsorbed (E_{hyd}) was -1.12×10^4 kJ/mol. The initial and energy-minimized surfaces are shown in **Figure 4-5**. The energy- minimization of the associative adsorption surface was -4.82×10^4 kJ/mol, and during the energy-minimization for associative adsorption, one H₂O molecule was released from the surface to the vacuum. For dissociative adsorption, on the other hand, the energy-minimization of the dissociative adsorption surface was -4.83×10^4 kJ/mol. Although these two values are nearly identical, dissociative adsorption is predicted to be a lower energy process for the forsterite (100) surface because a surface H₂O molecule was released during the energy-minimization of associative adsorption.

The associative and dissociative mechanisms of H₂O adsorption to the forsterite (010) surface were also modeled, and these surfaces are shown in **Figure 4-6**. For the (010) plane, 12 intact H₂O molecules were adsorbed to the slab, where the total energy contribution from the H₂O molecules adsorbed was -1.70×10^4 kJ/mol. The energy-minimization of the associative adsorption surface was -8.81×10^4 kJ/mol, and during this simulation, two H₂O molecules were released from the surface to the vacuum. For dissociative adsorption, on the other hand, eight H₂O molecules were adsorbed to the forsterite (010) slab, and the energy contribution of these molecules was -1.13×10^4 kJ/mol. Similar to the associative adsorption for this cleavage plane, one H₂O molecule was released from the surface to the vacuum. Two different numbers of H₂O molecules were adsorbed for the (010) cleavage plane to maintain charge neutrality in the system,

(a)



(b)

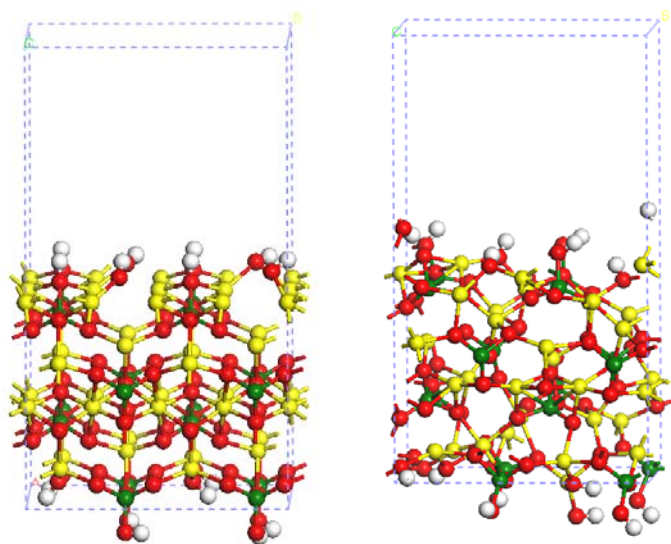


Figure 4-6: Hydrated forsterite (010) surface. a) Original (left) and energy-minimized (right) surface structures for associative adsorption of H_2O molecules. b) Original (left) and energy-minimized (right) surface structures for dissociative adsorption of H_2O molecules. The color scheme is the same as **Figure 4-5**.^{37,39}

which was a challenge due to the structure of the plane, particularly in the dissociative adsorption case. The energy-minimization of the dissociative adsorption surface was -8.31×10^4 kJ/mol. Because the cells used to simulate dissociative and associative adsorption have different numbers of atoms, comparisons regarding the energy of these processes will be limited to the relative energies, discussed below.

The relative energies for the associative and dissociative adsorption of H₂O molecules on the (100) and (010) cleavage planes are given in **Table 4-3**. For the (100) cleavage plane, γ_{diss} is 0.26 J/m², and γ_{assoc} is 0.32 J/m². As before, the similarity of these two values is a result of the nearly identical energy values for the hydrated surfaces. For the (010) cleavage plane, γ_{diss} is 1.89 J/m², and γ_{assoc} is 2.47 J/m². This confirms the expectation that dissociative adsorption would be a lower energy process for this cleavage plane.

4.3.4 Density Functional Theory Molecular Dynamics (DFT-MD) Simulations

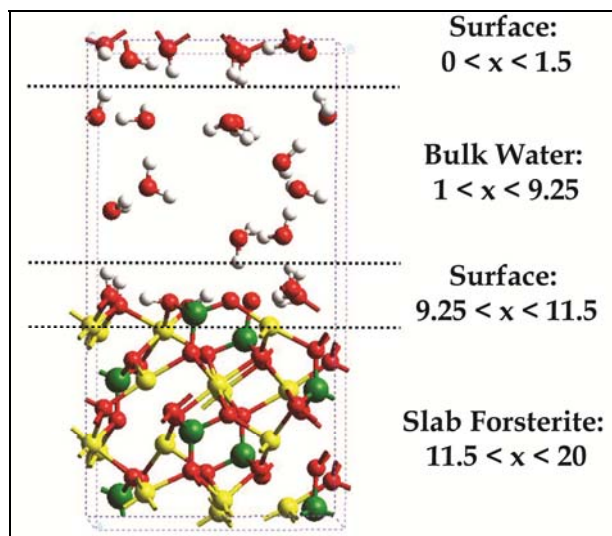
The results outlined in Sections 4.3.1–4.3.3 serve as the foundation for the simulations described in the current section. In the above analysis, the goals were to determine whether the (100) cleavage plane was more stable than the (010) cleavage plane and to investigate the surface structure of these planes when a monolayer of H₂O molecules is adsorbed to them. These systems were used to make samples that represented the aqueous-mineral interface for the forsterite (100) and (010) surfaces, where MD simulations were performed to investigate how the distribution of functional

groups on the surface changes with time and how the H-bonding network at the aqueous-mineral interface affects the surface structure.

The hydrated forsterite (100) surface that is solvated by 12 H₂O molecules is characterized by one O⁻, two H₂O, ten OH, and two O_{br} groups as listed in **Table 4-2**, and the initial starting configuration for the aqueous-mineral interface of this plane is shown in **Figure 4-7a**. There are 110 atoms in the simulation cell. The x-coordinates correspond to the vertical direction of **Figure 4-7a**, and the assignments of regions as surface, bulk water, and slab for forsterite are also shown. The average positions of O and H atoms in the forsterite (100) simulation cell for the low-density water system are shown in **Figures 4-7b** and **4-7c**, respectively. As with the fully-solvated forsterite (100) system, the locations of the O atoms remain roughly constant, with the exception of the O atoms in H₂O molecules in solution. For the H atom histogram shown in **Figure 4-7c**, the wide peaks from $0.00 \text{ \AA} \leq x \leq 10.25 \text{ \AA}$ show that the H atoms contained within this part of the system move quite a bit during the last 5 ps of the simulation.

The data described above for the forsterite (100) solvated by 12 H₂O molecules average the positions of O and H atoms over time. Throughout the simulation, the O⁻ group on the surface remained deprotonated except for a H⁺ transfer from a neighboring H₂O on the surface, but this H⁺ is transferred back within 0.5 ps. In addition, a H⁺ from an OH group on the surface is transferred to another, leaving O⁻ and H₂O groups on the surface at the end of the simulation. The O_{br} remains deprotonated throughout the entirety of the simulation, however. After 10 ps, there are three H₂O molecules adsorbed to the forsterite (100) surface for the low-density water system, and this corresponds to a

(a)



(b)

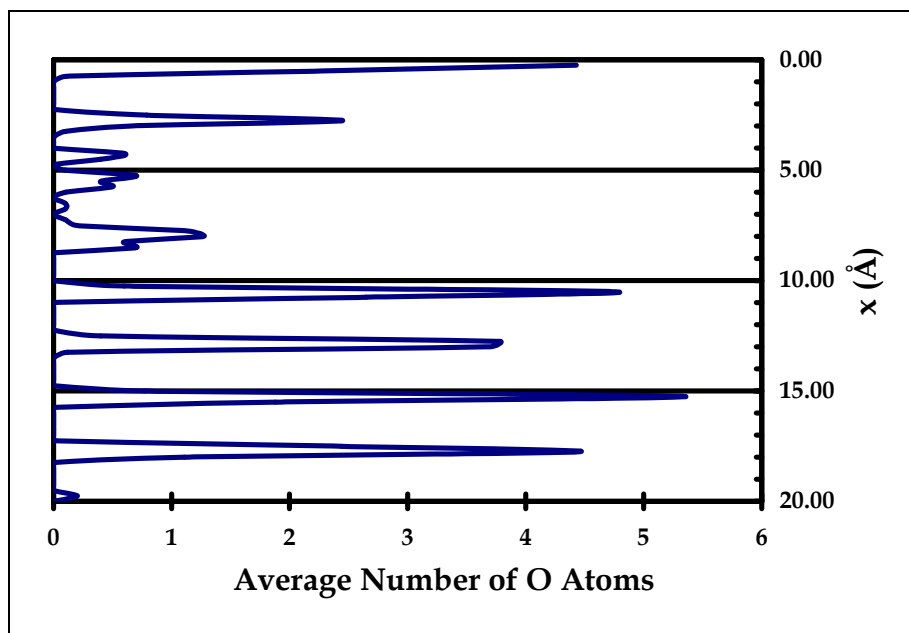
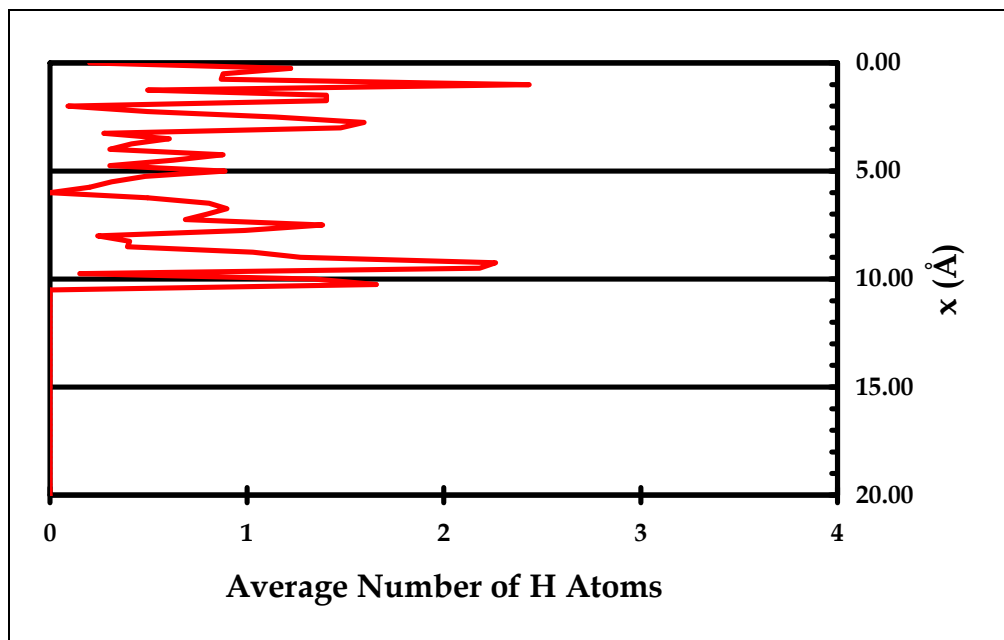


Figure 4-7: (a) Forsterite (100) surface solvated with low-density water. Atoms are characterized according to their x-coordinates (b) O atom histogram and (c) H atom histogram, where the absence of H atoms from $11 \leq x \leq 20$ corresponds to the forsterite slab. Each histogram is averaged over the last 5 ps of simulation. The color scheme is the same as **Figure 4-5**.

(c)



coverage of ~ 2 H₂O/nm². The relative stability of the forsterite (100) aqueous-mineral interface with 12 H₂O molecules studied here is 61.8 J/m² (**Table 4-3**).

4.3.5 Comparison to Computational Results and Experimental Data

The bulk crystal lattice dimensions calculated in this work are within 1% of the experimentally measured lattice parameters of $a = 4.756$ Å, $b = 10.207$ Å, $c = 5.980$ Å.⁴¹ In addition, the forsterite unit cell angles were determined to be $\alpha = \beta = \gamma = 90^\circ$ for a forsterite sample used in recent experiments,⁴² and the angles for the energy-minimized bulk sample from this work were the same as the experimental sample. The comparison of lattice parameters shows that the VASP calculations described in this work model the

electronic structure of this system well. Therefore, our computational methodology is an appropriate method to study forsterite surfaces.

The relative stabilities of the forsterite (100) and (010) surfaces were also calculated and are included in **Table 4-3**. The forsterite (100) surface was found to be more stable than the (010) surface, and this agrees with earlier findings.⁹ In addition, the dissociative adsorption surfaces were slightly more stable than the corresponding associative adsorption surfaces for the same cleavage plane. This is likely because less energy was required to stabilize the surfaces that already had H₂O molecules in a dissociated state. Furthermore, both the associative and dissociative adsorption samples minimize to surfaces with a similar distribution of functional groups on the surface.

These findings contrast earlier investigations employing force field calculations³⁸ and DFT calculations⁴³ where the authors concluded that associative and dissociative adsorption happen exclusively. Further, associative adsorption was considered more favorable because the process was calculated to be more exothermic.³⁸ However, this was a result of the fact that the H₂O molecules on the forsterite surface were not able to dissociate or recombine in those calculations because a non-reactive force field was used. At the same time, the H₂O molecules were found to prefer Mg²⁺ sites in the samples simulated here, which served to complete the coordination sphere on the forsterite surface, and similar results were found in a previous study.³⁸ More recently, density functional theory (DFT) calculations showed that dissociated H₂O molecules recombine,⁴³ which is also in accord with our current findings.

For both the forsterite (100) and (010) cleavage planes, the energy-minimized forms of the surfaces initially covered with either intact or dissociated H₂O molecules are

similar. A distribution of O^- , O_{br} , OH , and H_2O groups exists on each. These observations show that the protonation state of sites is an important contribution for the forsterite mineral structure. In addition, not all sites on the forsterite surface are covered with OH groups, which provides information regarding where dissolution reactions occur on the surface of this mineral.^{2,44} The results described show that different types of sites exist on the forsterite mineral surface, which corroborates the idea of identifying reactive sites on a mineral surface versus the total number of sites and total surface area.^{4,45}

A recent description of Mg^{2+} release from the forsterite mineral surface used the total number of OH groups possible on the (100) plane as possible reactive sites.² The rate of Mg^{2+} release calculated was $\sim 10^6$ – 10^9 times faster than experimentally measured rates, and the authors attributed this discrepancy to the possibility that they were not modeling the rate-limiting step.² However, another possibility is that the total number of OH groups does not equal the number of sites where a dissolution reaction will occur. As seen in this surface characterization study, not every functional group on the forsterite (100) and (010) surfaces is an OH group. What is more, OH sites are known to be preferential dissolution sites.⁴⁶

If one combines the results of this work with those of Morrow *et al.*,² then a new dissolution rate can be calculated. Using either the actual number of OH groups on the hydrated forsterite (100) or (010) surfaces or the number of H_2O and O^- groups, the Mg^{2+} release rate decreases by less than an order of magnitude (data not shown). This suggests that the rate of Mg^{2+} release is not only controlled by the types of groups on the surface but more importantly by the reactions that ultimately lead to surface functionality, such as degradation of the mineral structure as a result of adsorption of groups to the surface.⁴⁷

In addition, the formation of a silica rich layer on the surface of forsterite during dissolution^{42,48} also contributes to the overall rate for Mg^{2+} release.²

4.4 Conclusions and Future Directions

4.4.1 Conclusions

The Vienna Ab-initio Simulation Package (VASP) was used to model the adsorption of H_2O molecules onto the forsterite (100) and (010) cleavage planes. For both dissociative and associative adsorption, a distribution of sites that includes O^- , O_{br} , OH, and H_2O groups results for the energy-minimized surfaces. However, dissociative adsorption is predicted to be a lower energy process because the resulting surface was lower in energy than that for the associative surface for both the forsterite (100) and (010) cleavage planes. These results provide insight into reactive surface sites for this mineral in that not all of the sites on the surface are OH groups, as was previously modeled.²

The forsterite (100) and (010) cleavage planes were compared to identify which was more stable, and forsterite (100) was determined to be the more stable plane. This is in accord with previous force field calculations⁹ but in contrast to another.³⁸ In the present work, particular attention was given to cutting the slabs so that the number of dangling bonds was minimized, which can lead to the development of surface defects.³⁸ Knowledge of which plane is more stable is important for determining the concentration of each plane in a mineral sample, as the more stable planes are present in higher concentration.

The interaction of water with the forsterite surface as a monolayer phase has implications for the incorporation of water into the Earth during its accretionary phase. Currently, the means by which water arrived on Earth is not understood.^{12,14,15} Several theories include delivery by comets or asteroids, the reaction of hydrogen from nebular gas with iron oxides in the Earth's mantle, and the adsorption of gaseous water onto the accretion disk.^{12,14,15} An accretion disk describes a collection of interstellar grains that aggregate during planet formation,^{12,15,49} and at present, this theory seems the most plausible.¹⁵ If water adsorbed to these grains, then water could have been delivered to form Earth's oceans during this process.^{12,15} Moreover, olivine minerals,¹⁵ such as forsterite,^{12,13} are the most common astronomical minerals, and thus, adsorption of water to forsterite surfaces, such as the (100) and (010) cleavage planes modeled here, has astrobiological implications.

Regardless of which theory for the delivery of water to Earth is true, the adsorption of water onto olivine phases continues to be important throughout Earth's history. Earth is believed to have formed from water-containing materials,¹⁶ but debates exist regarding how much water was contained in the mantle throughout history^{18,20} and at present.¹⁶⁻²⁰ The amount of water present in the mantle contributes to the existence of plate tectonics on Earth¹⁷⁻¹⁹ and to the global water cycle,¹⁸ such as the volumes of Earth's oceans.⁵⁰ The mineralogic profile of Earth's mantle is dominated by olivine-rich minerals,^{17,50} and forsterite is the Mg-rich end-member of the olivine series. Therefore, the adsorption of water to forsterite surfaces as well as the functional groups present at the aqueous-mineral interface are important processes to model for understanding the contribution of water to olivine minerals in Earth's mantle.

In addition to the presence of forsterite in accretion disks and in Earth's mantle, this mineral has also been found on the surface of Mars. The perpetuation of this mineral phase throughout the planet's surface shows that water has not been present for billions of years or that a limited amount once existed because its dissolution rate is relatively rapid with respect to more silica-rich phases.²¹⁻²³ However, there is evidence for water on Mars in the forms of morphological alteration to minerals²³ and secondary mineral phases that likely resulted from acidic weathering of forsterite on Mars.^{21,23} These investigations into forsterite weathering provide insight into the aqueous alteration history^{22,23} as well as the impact it has on the chemistry of Martian soils.²¹ Forsterite dissolution on Mars is thought have to occurred under a low water/rock ratio,²¹ and in this work, the investigation of the aqueous-water interface for the forsterite (100) surface solvated by 12 H₂O molecules models such a system.

4.4.2 Future Directions

The main focus of the future directions of this work is to simulate the aqueous-mineral interface for the forsterite (100) and (010) cleavage planes. The energy-minimized structure that resulted from the dissociative adsorption of H₂O molecules onto the forsterite (100) and (010) surfaces will be used as the starting surface. Bulk water will be modeled by adding 1 g/cm³ H₂O molecules to the periodic cell, and the number of H₂O molecules needed will be determined via the following equations (4 and 5):

$$\frac{molecules}{A^3} = \frac{1g}{cm^3} * \frac{1cm^3}{(10^8 A)^3} * \frac{1mol}{18.02g} * \frac{6.02 * 10^{23} molecules}{1mol} \quad 4$$

$$molecules_in_cell = \frac{molecules}{A^3} * (cell_x * cell_y * cell_z) A^3 \quad 5$$

where *cell_x*, *cell_y*, and *cell_z* correspond to the parameters of the vacuum space over the forsterite (100) and (010) slabs. Sixteen H₂O molecules are needed for the forsterite (100) cell and 21 H₂O molecules for the (010) cell. Inclusion of H₂O molecules in the simulation cell according to **Equations 4-4-5** models solvation of the surface at the aqueous-mineral interface. The H₂O molecules will be energy-minimized separately in a cell whose dimensions were the same as the vacuum portion of the forsterite (100) and (010) simulation cells. DFT-MD simulations using these energy-minimized structures will be run for a 5 ps equilibration period with a timestep of 0.5 fs. Results for structural energy and dynamical analysis will then be collected over an additional 5 ps with a 0.5 fs timestep.

After 10 ps of simulation, the samples will be characterized according to how many of each functional are present on the surface. In addition, the average positions of O and H atoms in the simulation cells for the last 5 ps will be analyzed to determine how these atoms are moving during the timescale simulated. The goal of this analysis will be to understand where these atoms are located to provide insight into spectroscopic analysis used to characterize these systems.⁵¹

Some initial simulations have been performed for the forsterite (100) and (010) surfaces at the aqueous-mineral interface. Twenty-one H₂O molecules were used to solvate the forsterite (100) surface while 34 H₂O molecules were used to solvate the forsterite (010) surface. As with the monolayer surfaces, a distribution of functional

groups is present on the forsterite (100) and (010) surfaces at the aqueous-mineral interface. In addition, H^+ transfers occur between surface groups and between surface groups and solution, such that the distribution of functional groups present on the surface evolves with time. When H^+ ions adsorb to the surface, the primary sites are $Si-O^-$, $Mg-O_{br}$, or $Mg-OH$, and in the case of $Mg-O_{br}$ adsorption, this then results in a new reaction site on the surface. H_2O transfers from solution to surface sites also occur, and these are located at Mg sites on the surface, which has been observed in previous calculations.³⁸

On the surface of each of these samples at the aqueous-mineral interface, at least one O^- group is present. One would anticipate that this excess of electron density would be unstable on the surface and readily become protonated. Although H^+ ions are transferred to such sites throughout the simulations, O^- groups remain. This observation is in accord with previous DFT calculations where a $Si-O^-$ group was stabilized by solvation by three H_2O molecules,⁵² and therefore, such a site can be expected to perpetuate at the aqueous-mineral interface for forsterite.

For these two samples as well as those modeling 1 g/cm^3 , an analysis scheme will be designed to capture the events within the simulations that best capture the essential science of the aqueous-mineral interface for forsterite (100) and (010) surfaces. The number of H^+ and H_2O transfers can be calculated for each solvated forsterite (100) surface and the solvated forsterite (010) surface. The goal is to identify at which functional groups H^+ transfers occur and thus to show which are the more reactive sites on each surface. In addition, H^+ and H_2O transfers between surface groups and solution also occurred, and these transfers will be quantified and tracked with time. Further, such analysis will provide insight into whether the forsterite (100) or the (010) cleavage plane

is more reactive at the aqueous-mineral interface, particularly since the coverage of these surfaces by H₂O molecules is very similar among the systems studied.

In addition to quantification of H⁺ and H₂O transfers, the H-bond lengths can be calculated according to the analysis scheme of Kumar, *et al.*³² The H-bond interactions were shown to be the strongest between Ti–OH sites and H₂O molecules in a monolayer on the rutile surface, whereas Ti₂O sites interacted the weakest with H₂O molecules adsorbed to the rutile surface. Further, the bond lengths on the surface of goethite have been shown to lengthen as additional H₂O molecules solvate the surface.³³ A similar approach will be applied here to calculate the bond distances for sites on the forsterite (100) and (010) surfaces.

4.5 References

- (1) Nangia, S.; Garrison, B. J. *J. Phys. Chem. A* **2008**, *112*, 2027.
- (2) Morrow, C. P.; Kubicki, J. D.; Mueller, K. T.; Cole, D. R. *J. Phys. Chem. C* **2010**, *114*, 5417.
- (3) Brunauer, S.; Emmett, P. H.; Teller, E. *J. Am. Chem. Soc.* **1938**, *60*, 309.
- (4) Washton, N. M.; Brantley, S. L.; Mueller, K. T. *Geochim. Cosmochim. Ac.* **2008**, *72*, 5949.
- (5) Sanders, R. L.; Washton, N. M.; Mueller, K. T. *J. Phys. Chem. C* **2010**, 5491.
- (6) Brantley, S. L.; Mellott, N. P. *Am. Mineral.* **2000**, *85*, 1767.
- (7) Dove, P. M.; Han, N.; De Yoreo, J. J. *P. Natl. Acad. Sci. USA* **2005**, *102*, 15357.
- (8) Bandstra, J. Z.; Brantley, S. L. *Geochim. Cosmochim. Ac.* **2008**, *72*, 2587.
- (9) Watson, G. W.; Oliver, P. M.; Parker, S. C. *Phys. Chem. Miner.* **1997**, *25*, 70.
- (10) Toulhoat, H.; Digne, M.; Arrouvel, C.; Raybaud, P. *Oil Gas Sci. Technol.* **2005**, *60*, 417.
- (11) Awad, A.; van Groos, A. F. K.; Guggenheim, S. *Geochim. Cosmochim. Ac.* **2000**, *64*, 1765.
- (12) Stimpfl, M.; Walker, A. M.; Drake, M. J.; de Leeuw, N. H.; Deymier, P. *J. Cryst. Growth* **2006**, *294*, 83.
- (13) van Boekel, R.; Min, M.; Leinert, C.; Waters, L. B. F. M.; Richichi, A.; Chesneau, O.; Dominik, C.; Jaffe, W.; Dutrey, A.; Graser, U.; Henning, T.; de Jong, J.; Kohler, R.; de Koter, A.; Lopez, B.; Malbet, F.; Morel, S.; Paresce, F.; Perrin, G.; Preibisch, T.; Przygodda, F.; Scholler, M.; Wittkowski, M. *Nature* **2004**, *432*, 479.
- (14) Drake, M. J. *Meteorit. Planet. Sci.* **2005**, *40*, 519.
- (15) Muralidharan, K.; Deymier, P.; Stimpfl, M.; de Leeuw, N. H.; Drake, M. J. *Icarus* **2008**, *198*, 400.
- (16) Drake, M. J.; Richter, K. *Nature* **2002**, *416*, 39.
- (17) Regenauer-Lieb, K.; Kohl, T. *Mineral. Mag.* **2003**, *67*, 697.
- (18) Korenaga, J. *Terra Nova* **2008**, *20*, 419.
- (19) Albareda, F. *Nature* **2009**, *461*, 1227.
- (20) Schonbachler, M.; Carlson, R. W.; Horan, M. F.; Mock, T. D.; Hauri, E. H. *Science* **2010**, *328*, 884.
- (21) Hurowitz, J. A.; McLennan, S. M. *Earth Planet. Sc. Lett.* **2007**, *260*, 432.
- (22) Olsen, A. A.; Rimstidt, J. D. *Am. Mineral.* **2007**, *92*, 598.
- (23) Hausrath, E. M.; Treiman, A. H.; Vicenzi, E.; Bish, D. L.; Blake, D.; Sarrazin, P.; Hoehler, T.; Midtkandal, I.; Steele, A.; Brantley, S. L. *Astrobiology* **2008**, *8*, 1079.
- (24) Kresse, G.; Joubert, D. *Phys. Rev. B* **1999**, *59*, 1758.
- (25) Vienna Ab-initio Simulation Package (VASP) Group Page, <http://cms.mpi.univie.ac.at/vasp/>.
- (26) Kresse, G.; Furthmuller, J. *Comp. Mater. Sci.* **1996**, *6*, 15.
- (27) Kresse, G.; Furthmuller, J. *Phys. Rev. B* **1996**, *54*, 11169.
- (28) Bandura, A. V.; Sykes, D. G.; Shapovalov, V.; Troung, T. N.; Kubicki, J. D.; Evarestov, R. A. *J. Phys. Chem. B* **2004**, *108*, 7844.
- (29) Tunega, D.; Gerzabek, M. H.; Lischka, H. *J. Phys. Chem. B* **2004**, *108*, 5930.

- (30) Kubicki, J. D.; Paul, K. W.; Sparks, D. L. *Geochem. T.* **2008**, *9*, 4.
- (31) Zhang, Z.; Fenter, P.; Cheng, L.; Sturchio, N. C.; Bedzyk, M. J.; Predota, M.; Bandura, A.; Kubicki, J. D.; Lvov, S. N.; Cummings, P. T.; Chialvo, A. A.; Ridley, M. K.; Benezeth, P.; Anovitz, L.; Palmer, D. A.; Machesky, M. L.; Wesolowski, D. J. *Langmuir* **2004**, *20*, 4954.
- (32) Kumar, N.; Neogi, S.; Kent, P. R. C.; Bandura, A. V.; Kubicki, J. D.; Wesolowski, D. J.; Cole, D. R.; Sofo, J. O. *J. Phys. Chem. C* **2009**, *113*, 13732.
- (33) Hafner, J. *Comput. Phys. Commun.* **2007**, *177*, 6.
- (34) Blochl, P. E. *Phys. Rev. B* **1994**, *50*, 17953.
- (35) Hafner, J.; Wolverton, C.; Ceder, G. *MRS Bull.* **2006**, *31*, 659.
- (36) Monkhorst, H. J.; Pack, J. D. *Phys. Rev. B* **1976**, *13*, 5188.
- (37) Cerius²; Accelrys: San Diego, CA.
- (38) de Leeuw, N. H.; Parker, S. C.; Catlow, C. R. A.; Price, G. D. *Phys. Chem. Miner.* **2000**, *27*, 332.
- (39) Materials Studio; Accelrys: San Diego, CA.
- (40) Demichelis, R.; Civalleri, B.; Ferrabone, M.; Dovesi, R. *I. J. Quantum Chem.* **2010**, *110*, 406.
- (41) Smyth, J. R.; Hazen, R. M. *Am. Mineral.* **1973**, *58*, 588.
- (42) Davis, M. C.; Brouwer, W. J.; Wesolowski, D. J.; Anovitz, L. M.; Lipton, A. S.; Mueller, K. T. *Phys. Chem. Chem. Phys.* **2009**, *11*, 7013.
- (43) de Leeuw, N. H. *J. Phys. Chem. B* **2001**, *105*, 9747.
- (44) Pokrovsky, O. S.; Schott, J. *Geochim. Cosmochim. Ac.* **2000**, *64*, 3313.
- (45) Sanders, R. L.; Washton, N. M.; Mueller, K. T. *J. Phys. Chem. C* **2010**, *114*, 5491.
- (46) Stumm, W.; Wollast, R. *Rev. Geophys.* **1990**, *28*, 53.
- (47) Rosso, J. J.; Rimstidt, J. D. *Geochim. Cosmochim. Ac.* **2000**, *64*, 797.
- (48) Pokrovsky, O. S.; Schott, J. *Geochim. Cosmochim. Ac.* **2000**, *64*, 3299.
- (49) Lewis, J. S. *Physics and Chemistry of the Solar System*; Academic Press: New York, 1997.
- (50) Smyth, J. R.; Frost, D. J.; Nestola, F.; Holl, C. M.; Bromiley, G. *Geophys. Res. Lett.* **2006**, *33*, 5.
- (51) Chen, S. S.; Navrotsky, A. *Am. Mineral.* **2010**, *95*, 112.
- (52) Kubicki, J. D. *J. Phys. Chem. A* **2001**, *105*, 8756.

Chapter 5

Conclusions and Future Directions

5.1 Summary of Research

The overarching goal of the work presented in this dissertation was to use existing computational tools to model geochemical systems across spatial and temporal scales. Density functional theory (DFT) calculations were employed to model the release of divalent metal ions from individual surface sites on ortho- and framework-silicate mineral surfaces. DFT molecular dynamics (DFT-MD) simulations were used to model the forsterite mineral surface along two different cleavage planes, and these simulations allowed for the description of multiple surface sites simultaneously. Hence, the use of DFT-MD simulations enabled investigation of a larger system size as well as a longer timescale, as bulk physicochemical processes were modeled.

In Chapter 2, Mg^{2+} release from the forsterite mineral surface from sites of various protonation states was modeled. A reaction mechanism was described for hydrolysis of each type of site, and the barrier heights were also calculated. Ab-initio results were coupled with experimental data, which incorporated the concentration of sites in each protonation state. The mechanisms showed that hydrolysis occurs through two steps, namely the breaking of the Mg–O bond and the incorporation of a H_2O molecule from the second hydration sphere into the first hydration sphere. In both the gas-phase and aqueous-phase, the protonated sites have the lowest barrier height,

followed by the deprotonated and neutral sites, respectively. In addition, calculations employing aqueous-phase models must be optimized because single-point aqueous-phase calculations yielded unreliable results, and this is particularly important when modeling geochemical processes that occur in aqueous media.

The rate constants for the release of Mg^{2+} from Mg–O–Si sites were calculated using the barrier heights from the DFT calculations. The rate constants and thus Mg^{2+} release rates were higher than those measured experimentally,¹⁻⁷ which was, in part, a result of higher E_{app} values measured experimentally for the dissolution of forsterite.^{8,9} This shows that the rate-limiting step is not the release of Mg^{2+} as a result of breaking the last Mg–O bond to the forsterite surface. At the same time, the DFT results corroborate previous experimental and DFT findings. ^1H - ^{29}Si cross-polarization magic angle spinning (CPMAS) NMR experiments showed that a Mg-depleted, Si-rich layer develops on the forsterite surface during dissolution in acidic conditions.¹⁰ When the DFT results from this work are compared with barrier heights for the hydrolysis of Si–O–Si sites on quartz,¹¹⁻¹⁴ Mg^{2+} ions would be expected to leach first from forsterite during dissolution.

The reaction coordinates were chosen from two possibilities. Initially, the Mg–OH₂ distance seemed reasonable, but decreasing the distance between the H₂O molecule in the second hydration sphere and the Mg^{2+} ion did not lead to the breaking of the Mg–O bond connecting the ion with the surface. Instead, such a reaction coordinate led to the exchange of H₂O molecules around the Mg^{2+} ion, while the Mg–O bond remained unbroken. Thus, Mg–O bonds on the forsterite surface break as a result of the lengthening of this bond and not from H₂O exchange around the Mg^{2+} ion.

In Chapter 3, the link between H₂O exchange reactions and M–O bond break was investigated to determine which of these processes led to release of metal ions to solution. The H₂O exchange reaction around the hexaaqua Mg²⁺ ion was modeled in the gas-phase and aqueous-phase, using both the IEFPCM and super-molecule approximations. The barrier heights using the IEFPCM and super-molecule approaches were comparable to experimental values within computational uncertainty. The high barrier height for this reaction in the gas-phase is likely a result of a high energy TS characterized by distorted pentagonal bipyramidal geometry. In the IEFPCM and super-molecule calculations, however, the TSs had square-pyramidal geometry, indicative of six electron pairs around the Mg²⁺ ion. The different TS geometries for these two phases result in a barrier height for the gas-phase that was ~30–40 kJ/mol higher than the aqueous-phase models. The aqueous-phase model calculations show that this approach is appropriate for these systems.

DFT calculations were used to probe the link between H₂O exchange reactions for hydrated metal ions and dissolution of end-member silicate minerals containing those ions. Protonated Ni–O–Si, Mg–O–Si, and Ca–O–Si sites were found to react via three separate mechanisms. The breaking of the Ni–O bond occurs as a result of approach of a H₂O molecule from the second hydration sphere. For protonated Mg–O–Si sites, approach of a H₂O molecule instead leads to H₂O exchange around the Mg²⁺ ion. Breaking the Mg–O bond is accomplished by lengthening of the bond, in contrast to protonated Ni–O–Si sites. Ca–O–Si sites react via closely coupled reactions for H₂O exchange and hydrolysis. Instead of a traditional H₂O exchange reaction, the second hydration sphere H₂O molecule was absorbed by the Ca²⁺ ion to form a hepta-

coordinated Ca-silicate cluster. Similar to protonated Mg–O–Si sites, the breaking of the Ca–O bond occurred via lengthening this bond, but the precise reaction mechanism was difficult to elucidate.

The barrier heights of these reactions were used to calculate the rate constants for these reactions via the classical TST approximation, and in accord with experimental trends,^{15,16} the rate constants increase in the order $\text{Ni}^{2+} < \text{Mg}^{2+} < \text{Ca}^{2+}$. What is more, rate constants for hydrolysis and H_2O exchange of these M–O–Si clusters differ from rate constants for H_2O exchange around these ions in solution, and therefore, the Si-containing group as opposed to a sixth H_2O molecule contributes to the kinetics of these metal ions.^{17,18} The rate constants for H_2O exchange and hydrolysis around protonated Ni–O–Si and Mg–O–Si sites are lower than those for $\text{Ni}(\text{H}_2\text{O})_6^{2+}$ and $\text{Mg}(\text{H}_2\text{O})_6^{2+}$. For protonated Ca–O–Si sites, however, the rate constant for $\text{Ca}(\text{H}_2\text{O})_6^{2+}$ is lower than those for the formation of the hepta-coordinated complex and hydrolysis.

As with the calculations in Chapter 2, there were two possibilities for the reaction coordinate. Initially, the distance between the metal ion and the H_2O molecule in the second hydration sphere was used. If a H_2O exchange reaction occurred and not hydrolysis, then the M–O bond was lengthened until it broke. A second PES scan was performed to model the absorption of the second hydration sphere H_2O molecule into the first. In this way, the correlation between H_2O exchange reaction rates and hydrolysis rates for protonated sites on end-member silicates was modeled.

In Chapter 4, DFT-MD calculations via the VASP were used to simulate the adsorption of a monolayer of H_2O molecules to the forsterite (100) and (010) cleavage planes. Both the associative and dissociative adsorption processes were modeled for each

cleavage plane, and the energy-minimized surfaces were characterized by a distribution of functional groups that included O_{br} , O^- , OH, and H_2O sites regardless of whether the starting surface was covered with dissociated or intact H_2O molecules. For both the (100) and (010) surfaces, dissociative adsorption is predicted to be a lower-energy process.

In addition to investigating the surface structure for the adsorption of H_2O molecules, a comparison was made regarding the stability of the (100) and (010) cleavage planes for forsterite, and the (100) plane was determined to be lower in energy. This is in accord with a previous study¹⁹ but in contrast to another.²⁰ However, care was taken here to cut the slabs such that dangling bonds were minimized, and thus the formation of defects on the surface was avoided. The presence of both dangling bonds and surface defects contributed to the instability of forsterite (100) in a previous study, which is likely why it was found to be higher in energy than the (010) cleavage plane.²⁰

5.2 Expected Implications

There were several goals to the work described in this dissertation. The first was to use existing computational tools to model geochemical systems across spatial and temporal scales. The second was to provide molecular scale insight into experimental observations. The third goal of this work was to combine experimental data with calculated results. The fourth goal was to initiate a study of the forsterite surface at the aqueous-mineral interface so that larger-scale investigations of the forsterite surface at

various stages during dissolution could be modeled, and these future calculations are described in **Section 5.3**.

These goals were each successfully attained. Two different timescales and spatial scales were modeled through metal release from single surface sites on silicate surfaces as well as by simulating the aqueous-mineral interface on a unit cell sized scale for forsterite. Molecular scale insight was provided by determining how the final M–O bond connecting the metal surface breaks as a result of H₂O approach for protonated Ni–O–Si sites and as a result of M–O bond lengthening for protonated Ca–O–Si sites and for Mg–O–Si sites in various protonation states. In addition, differences in calculated Mg²⁺ release rates from forsterite as well as surface characterization studies for unit cell sized forsterite systems show that rate-controlling dissolution reactions likely occur at specific reactive sites on the surface versus all sites present. Experimental data were combined with calculated results in Chapter 2, where the coverage of the forsterite surface by H⁺ or OH[−] ions measured experimentally versus pH was combined with ab-initio results to calculate a rate for Mg²⁺ release. Also in Chapter 3, the rate constants calculated for H₂O exchange and hydrolysis for protonated M–O–Si (M = Ni²⁺, Mg²⁺, and Ca²⁺) clusters are compared with those measure for H₂O exchange reactions around these ions in solution. The initial work for simulating the aqueous-mineral interface for two forsterite cleavage planes was begun. Initial findings showed that the (100) cleavage plane is lower in energy than the (010) plane and that dissociative adsorption of H₂O molecules is likely the lower energy process. However, for both associative and dissociative adsorption, the energy-minimized surfaces are characterized by sites with a distribution of functional groups.

The implications of this work pertain to integrating computational tools into geochemical kinetics investigations. Existing computational technology allows for detailed descriptions of the mechanisms throughout which geochemical species react. Further, the employment of multi-scale tools allows for insight into which processes are rate-controlling and if any act concertedly. Examples include the coupled H₂O exchange and hydrolysis reaction for protonated Ca–O–Si and the presence of a distribution of functional groups on the forsterite surface. Lastly, such a multi-faceted approach begs to question whether these approaches can be similarly adapted for other minerals. In fact, studies for quartz,^{11-14,21-24} aluminosilicates,^{25,26} and rutile²⁷⁻²⁹ have already been performed, and possibilities for future study include mixed-cation silicate minerals.³⁰

In addition, the description of molecular scale models provides insight into experimental observations of geochemical systems on much larger temporal and spatial scales. For example, current experimental studies use laboratory-scale models to replicate field conditions and isolate which are the controlling factors to dissolution rates measured in the field, and reasons for discrepancies between the dissolution rates for minerals at the different time and spatial scales are suggested.^{31,32} White and Brantley showed that the surface roughness in part contributed to differences between lab and field dissolution rates,³¹ while Navarre-Sitchler and Brantley showed that a number of contributing factors including reaction mechanism account for the discrepancies in dissolution rates between scales.³² In this way, molecular scale understanding of their geochemical systems would further contribute to their conclusions. For example, molecular scale models enable the amount of energy to be calculated for simplified systems where the most fundamental phenomena can be simulated. Therefore, the

aspects of the system which are the energetically controlling the observed process can be identified, and in these experimental examples,^{31,32} such molecular scale insight would explain why two different minerals within the same sample weather at different rates.

5.3 Future Directions

Studies of the aqueous-mineral interfaces for the forsterite (100) and (010) surfaces are currently in progress. The number of H₂O molecules required to simulate the presence of bulk water over the forsterite (100) and (010) slabs is being energy-minimized in the vacuum space above the slab, and once finished, these molecules will be added to the simulation cell. DFT-MD simulations will be performed for 10 ps, where a 5 ps equilibrium period will be followed by 5 ps of analysis time. The location of O and H atoms within the simulation cell will be analyzed with time, and the number of H⁺ and H₂O transfers over time will be calculated. Both H⁺ and H₂O transfers are anticipated to occur between groups on the surface and between surface groups and species in solution. This would lead to a change in the number of functional groups on the surface throughout the surface, but a distribution of functional groups is expected to remain throughout these simulations. In addition, the O–H bond lengths and H-bond interaction distances will be calculated so that these quantities can be compared to experimental measurements. These distances were found to change from equilibrium at the aqueous-mineral interface for rutile,²⁹ and thus a similar analysis will be conducted here.

Moreover, the studies described in Chapters 2–4 focused on pristine mineral surfaces. During dissolution, however, the mineral surface is physically^{3,33-35} as well as chemically altered, and for forsterite, a Mg-depleted layer develops.^{10,36} At this point, no molecular scale description of such a layer has been delineated, but this layer is known to consist of Si atoms with three Si–O–Si bonds.¹⁰ Thus one possible future direction of this work is to employ DFT-MD simulations in order to investigate the stability of a forsterite surface where Mg²⁺ ions have been removed and isolated SiO₄⁴⁻ tetrahedra remain.

Similarly, the presence of re-polymerized SiO₄⁴⁻ tetrahedra has been characterized via ¹H-²⁹Si cross-polarization magic angle spinning (CPMAS) NMR,¹⁰ but the mechanism through which the surface reconnects these isolated tetrahedra is not yet known. This re-polymerization of silica species on the forsterite surface could be investigated with a multi-scale approach similar to the one adopted in this dissertation. For example, molecular clusters comprised of several Mg–O–Si linkages could be designed and then Mg²⁺ ions removed, leaving behind SiO₄⁴⁻ tetrahedra. The energy for this process could be calculated. The ensuing Mg-depleted clusters could be reacted with H₂O molecules to show how these tetrahedra connect to form the silica-rich layer observed experimentally.^{10,36} In addition, a forsterite sample comprised of several unit cells could be modeled, and again Mg²⁺ ions removed. Here, DFT-MD simulations modeling this Mg-depleted forsterite surface at the aqueous-interface could be performed such that H⁺ and H₂O from solution, for example, would be available to react with the surface, and surface reconstruction to yield a silica-rich layer could be modeled over time.

Once these Mg-depleted and re-polymerized samples have been sufficiently energy-minimized, they would be used to calculate NMR chemical shifts. Davis *et al.*¹⁰ observed chemical shifts at –62 ppm for the pristine forsterite surface, corresponding to Q^0 Si atoms – that is, those Si atoms without any Si–O–Si bonds. At 190 h of dissolution in acidic media, a peak at –93 ppm, corresponding to Q^3 Si atoms – those Si atoms with three Si–O–Si bonds – began to develop. The molecular clusters representing intact forsterite and Mg-depleted forsterite surfaces could be used in an attempt to replicate the experiments of Davis *et al.*

The expected implications of these future directions are to continue to develop a molecular scale picture of forsterite dissolution and to discern an appropriate method for calculating NMR shifts of minerals. The mechanisms for Mg^{2+} release from sites of various protonation states and for H_2O exchange and hydrolysis of protonated M–O–Si (M = Ni^{2+} , Mg^{2+} , and Ca^{2+}) sites were described in Chapters 2 and 3, respectively. However, questions remain as to the stability of the surface after Mg^{2+} release and the process through which SiO_4^{4-} tetrahedra re-polymerize. Previous work where NMR chemical shifts were calculated showed that these results are heavily dependent upon which functional and basis set were chosen.³⁷⁻³⁹ Therefore, determining the NMR chemical shifts for these geochemical systems will also allow for a more systematic approach of calculating NMR chemical shifts with ab-initio methods.

5.4 References

- (1) Grandstaff, D. E. The dissolution rate of forsteritic olivine from Hawaiian beach sand. In *Rates of Chemical Weathering of Rocks and Minerals*; Colman, S. M., Dethier, D. P., Eds.; Academic Press, Inc.: New York, 1986; pp 49.
- (2) Wogelius, R. A.; Walther, J. V. *Chem. Geol.* **1992**, 97, 101.
- (3) Pokrovsky, O. S.; Schott, J. *Geochim. Cosmochim. Ac.* **2000**, 64, 3313.
- (4) Rosso, J. J.; Rimstidt, J. D. *Geochim. Cosmochim. Ac.* **2000**, 64, 797.
- (5) Oelkers, E. H. *Chem. Geol.* **2001**, 175, 485.
- (6) Olsen, A. A.; Rimstidt, J. D. *Geochim. Cosmochim. Ac.* **2008**, 72, 1758.
- (7) Wogelius, R. A.; Walther, J. V. *Geochim. Cosmochim. Ac.* **1991**, 55, 943.
- (8) Awad, A.; van Groos, A. F. K.; Guggenheim, S. *Geochim. Cosmochim. Ac.* **2000**, 64, 1765.
- (9) Van Herk, J.; Pietersen, H. S.; Schuiling, R. D. *Chem. Geol.* **1989**, 76, 341.
- (10) Davis, M. C.; Brouwer, W. J.; Wesolowski, D. J.; Anovitz, L. M.; Lipton, A. S.; Mueller, K. T. *Phys. Chem. Chem. Phys.* **2009**, 11, 7013.
- (11) Nangia, S.; Garrison, B. J. *J. Phys. Chem. A* **2008**, 112, 2027.
- (12) Xiao, Y.; Lasaga, A. C. *Geochim. Cosmochim. Ac.* **1994**, 58, 5379.
- (13) Xiao, Y.; Lasaga, A. C. *Geochim. Cosmochim. Ac.* **1996**, 60, 2283.
- (14) Pel'menschikov, A.; Leszczynski, J.; Pettersson, L. G. M. *J. Phys. Chem.* **2001**, 105, 9528.
- (15) Casey, W. H. *J. Coll. Interf. Sci.* **1991**, 146, 586.
- (16) Casey, W. H.; Westrich, H. R. *Nature* **1992**, 355, 157.
- (17) Helm, L.; Merbach, A. E. *Chem. Rev.* **2005**, 105, 1923.
- (18) Richens, D. T. *Chem. Rev.* **2005**, 105, 1961.
- (19) Watson, G. W.; Oliver, P. M.; Parker, S. C. *Phys. Chem. Miner.* **1997**, 25, 70.
- (20) de Leeuw, N. H.; Parker, S. C.; Catlow, C. R. A.; Price, G. D. *Phys. Chem. Miner.* **2000**, 27, 332.
- (21) Criscenti, L. J.; Kubicki, J. D.; Brantley, S. L. *J. Phys. Chem. A* **2006**, 110, 198.
- (22) Nangia, S.; Garrison, B. J. *Mol. Phys.* **2009**, 107, 831.
- (23) Nangia, S.; Garrison, B. J. *J. Am. Chem. Soc.* **2009**, 131, 9538.
- (24) Nangia, S.; Garrison, B. J. *J. Phys. Chem. C* **2010**, 114, 2267.
- (25) Criscenti, L. J.; Brantley, S. L.; Mueller, K. T.; Tsomaia, N.; Kubicki, J. D. *Geochim. Cosmochim. Ac.* **2005**, 69, 2205.
- (26) Morrow, C. P.; Nangia, S.; Garrison, B. J. *J. Phys. Chem.* **2009**, 113, 1343.
- (27) Bandura, A. V.; Sykes, D. G.; Shapovalov, V.; Troung, T. N.; Kubicki, J. D.; Evarestov, R. A. *J. Phys. Chem. B* **2004**, 108, 7844.
- (28) Zhang, Z.; Fenter, P.; Cheng, L.; Sturchio, N. C.; Bedzyk, M. J.; Predota, M.; Bandura, A.; Kubicki, J. D.; Lvov, S. N.; Cummings, P. T.; Chialvo, A. A.; Ridley, M. K.; Benezeth, P.; Anovitz, L.; Palmer, D. A.; Machesky, M. L.; Wesolowski, D. J. *Langmuir* **2004**, 20, 4954.
- (29) Kumar, N.; Neogi, S.; Kent, P. R. C.; Bandura, A. V.; Kubicki, J. D.; Wesolowski, D. J.; Cole, D. R.; Sofo, J. O. *J. Phys. Chem. C* **2009**, 113, 13732.

- (30) Westrich, H. R.; Cygan, R. T.; Casey, W. H.; Zemitis, C.; Arnold, G. W. *Am. J. Sci.* **1993**, 293, 869.
- (31) White, A. F.; Brantley, S. L. *Chem. Geol.* **2003**, 202, 479.
- (32) Navarre-Sitchler, A.; Brantley, S. *Earth Planet. Sc. Lett.* **2007**, 261, 321.
- (33) MacInnis, I. N.; Brantley, S. L. *Geochim. Cosmochim. Ac.* **1992**, 56, 1113.
- (34) Macinnis, I. N.; Brantley, S. L. *Chem. Geol.* **1993**, 105, 31.
- (35) Luttge, A. *Am. Mineral.* **2005**, 90, 1776.
- (36) Pokrovsky, O. S.; Schott, J. *Geochim. Cosmochim. Ac.* **2000**, 64, 3299.
- (37) Gao, Q.; Yokojima, S.; Fedorov, D. G.; Kitaura, K.; Sakurai, M.; Nakamura, S. *J. Chem. Theory Comput.* **2010**, 6, 1428.
- (38) Casabianca, L. B.; De Dios, A. C. *J. Chem. Phys.* **2008**, 128, 10.
- (39) Tossell, J. A. Calculating the NMR properties of minerals, glasses, and aqueous species. In *Molecular Modeling Theory: Applications in the Geosciences*; Mineralogical Soc. America: Washington, 2001; Vol. 42; pp 437.

VITA

Christin Palombo Morrow

104 Chemistry Building, Box 202
University Park, PA 16802
cup126@psu.edu (814) 863-3584

EDUCATION

Doctor of Philosophy Candidate, Chemistry, September 2008 – August 2010, Anticipated
The Pennsylvania State University, University Park, PA 16802
Advisors: Drs. Karl Mueller and James Kubicki

Master of Science, Chemistry, December 2008
The Pennsylvania State University, University Park, PA 16802
Advisor: Dr. Barbara Garrison

Bachelor of Science, Chemistry, May 2004
Marist College, Poughkeepsie, NY 12601
Mathematics, Minor
Honors: Cum Laude
Study Abroad: La Scuola de Lorenzo de' Medici, Florence, Italy

PUBLICATIONS

Morrow, C. P.; Kubicki, J. D. Density Functional Theory Modeling of Water on Forsterite (100) and (010) Surfaces, *J. Phys. Chem. C*, in preparation.

Morrow, C. P.; Olsen, A. A.; Kubicki, J. D. Quantum Mechanical Modeling of Hydrolysis and H₂O-Exchange in Mg-, Ca- and Ni-Silicate Clusters: Implications for Dissolution Mechanisms of Olivine Minerals, *J. Phys. Chem. C*, **2010**, submitted.

Morrow, C. P.; Kubicki, J. D.; Mueller, K. T.; Cole, D. R. A Description of Forsterite Dissolution using Ab-Initio Methods. *J. Phys. Chem. C* **2009**, *114*, 5417.

Morrow, C. P.; Nangia, S.; Garrison, B. J. Ab-Initio Investigation of Dissolution Mechanisms in Aluminosilicate Minerals. *J. Phys. Chem. A* **2009**, *113*, 1343.

SIGNIFICANT PROFESSIONAL ACCOMPLISHMENTS

Second Place Winner, Penn State University, University Park, PA
Environmental Chemistry Student Symposium (ECSS), 2010, 2009 (Oral); 2008 (Poster)

American Chemical Society (ACS), Fall 2009 National Meeting, Washington, DC
Co-Organizer and On-Site Coordinator, Café Chemistry, August 16 – 19, 2009

Graduate Student Winner, Penn State University, University Park, PA
Achieving Women Award, Commission for Women (CFW), 2009

Graduate Women in Science (GWIS), Nu Chapter, Penn State University, University Park, PA
Chair, Voices Conference Planning Committee, November 2008 – March 2009
Treasurer, January 2008 – May 2009

American Chemical Society (ACS), Central Pennsylvania Section, State College, PA
Chair, Government Action Committee (GAC), January 2006 – Present
